Accurate atom counting for entanglement-enhanced atom interferometry

Von der QUEST-Leibniz-Forschungsschule der
Gottfried Wilhelm Leibniz Universität Hannover

zur Erlangung des Grades

Doktor der Naturwissenschaften
- Dr. rer. nat. -

genehmigte Dissertation von

M. Sc. Andreas Christian Hüper,

2020

Referent:	apl. Prof. Dr. Carsten Klempt, Institut für Quantenoptik, Leibniz Universität Hannover
Korreferent:	Prof. Dr. Silke Ospelkaus, Institut für Quantenoptik, Leibniz Universität Hannover
Korreferent:	Prof. Dr. Jan Arlt, Department of Physics and Astronomy, Aarhus University
Tag der Promotion:	17.06.2019

Abstract

Atom interferometers belong among today's most precise sensors and offer a broad range of possible metrological applications. Given their ability to measure accelerations and rotations precisely, they are suitable for inertial sensing, navigation and geodesy. Beyond this, they proved indispensible for time-keeping as well as fundamental research. This explains why the improvement of achievable sensitivities of atom interferometers is of particular interest.
However the sensitivity of atom interferometers is fundamentally restricted by the standard quantum limit. The standard quantum limit can only be surpassed by employing entangled many-partice states. Entangled states, such as the twin-Fock state, allow atom interferometers to improve the phase sensitivity beyond the standard quantum limit, but they are reliant on an accurate detection of the interferometric out come. In this work, an experimental apparatus is designed and set up that will allow for routine generation of highly entangled twin-Fock states in a ^{87}Rb spinor Bose-Einstein condensate. As the main feature of this apparatus, an accurate atom counting fluorescence detection has been implemented. This detection achieves single-particle resolving fluorescence measurements for 1 up to 30 atoms. According to the noise analysis the single-atom resolution extends to a limiting atom number of 390(20) atoms. The implemented quadrupole coils with their strong gradient of up to 300 G/cm offer a tight confinement that in combination with the 55 W optical dipole trap laser will enable a fast repetition rate of the creation of highly entangled quantum states.

Key words: accurate atom counting, entanglement-enhanced atom interferometry, single-atom resolution

Contents

Chapter 1

Introduction

The story of entanglement begins with one of physics' most famous paradoxes and a hand full physicists that later will be known as pioneers in the, at the time, young field of quantum mechanics. Einstein, Podolsky and Rosen came up with a thought experiment of two perfectly correlated particles that violated EPRs notions of realism and/or locality, when described by quantum mechanics [1]. The ensuing discussion about this so-called EPR paradoxon with their peers Schrödinger, Born and Dirac manifested the concept of entangled particles [2–4]. Even today the correlations exhibited by entangled particles are equally as intriguing as they were 85 years ago. They only seem to be observable in the microscopic quantum world but are absent in our everyday experience of the macroscopic world. This divide between the physical laws governing the microscopic and the macroscopic realms begs the question for the transition between the two [5–7] and what types of entanglement can be created in different systems and sizes. In smaller, well-controlled systems, entanglement for up to 10 photons [8] and 20 ions has been created [9]. More entangled particles but less control about the individual constituents is offered by up to 910 entangled atoms in a Bose-Einstein condensate [10]. Beyond being a mere subject in the fundamental question for the classical-to-quantum transition, entanglement has become a resource for many new fields of research. Divers applications of the the fields of quantum simulation [11], quantum cryptography [12], quantum information processing [13], quantum computation and quantum communication [14] rely on entangled states of particles. Entanglement plays a pivotal role for the field of quantum metrology, in particular for atom interferometers. These measurement devices rely on interference effects between massive particles to measure time [15, 16], acceleration [17–19], earth's rotation [20–24], magnetic [25] fields, microwave fields [26] and are even employed for tests of general relativity [27]. A fundamental limit in the context of atom interferometry is the standard

quantum limit. It is a direct consequence of counting uncorrelated particles and limits the achievable sensitivity to $1/\sqrt{N}$, where N is the number of employed particles. While using more particles does increase the sensitivity, it also comes with the drawbacks of technical problems like increased collision rates and density-dependent losses. A paradigm shift comes about with the use of entangled many-particle states as they allow to overcome the standard quantum limit and enhance the measurement precision [28]. These entanglement-enhanced atom interferometers are fundamentally limited only by the Heisenberg limit, according to which the achievable sensitivity for N particles scales as $1/N$. Ions have excelled at reaching this limit due to their well-controlled interactions and efficient detection schemes [29]. Experiments with spin-squeezed Bose-Einstein condensates [30, 31] have demonstrated a sensitivity gain beyond the standard quantum limit [32, 33]. Spin-changing collisions are an established technique to create highly entangled many particle states of neutral atoms in Bose-Einstein condensates [34, 35] and were employed in the demonstration of a an atomic twin-Fock interferometer [36]. In this case, the performance was mainly limited by the detection noise of the applied absorption detection. To gain full access to the sensitivity enhancement that mesoscopic entangled states could deliver, they need to be paired with a detection that can distinguish single atoms at mesoscopic sample sizes. In order to count the atoms within an ultracold cloud, detection techniques like absorption imaging and fluorescence imaging are most commonly employed. Absorption imaging works by illuminating the atomic cloud with a resonant laser beam and detecting the shadow that is cast by the cloud. With this technique detection uncertainties of about 4 atoms are possible [37]. Fluorescence imaging is based on exciting the atoms internal energy state by (near-) resonant laser light and detecting the emitted fluorescence photons. This technique is especially applicable to detect atoms in a magneto-optical trap, as the emission of fluorescence photons occurring naturally. While fluorescence detection can be applied to atoms in other trapping scenarios, the fact that atoms in a magneto-optical trap are not only trapped but also actively cooled by the excitation light allows for prolonged interrogation times. Longer detection times scale the signal-to-noise ratio caused by photon shot noise favorably. Detecting the fluorescence photons emitted by atoms held in a magneto-optical traps, the detection of single and few atoms simultaneously has already been realized [38–42]. Yet only recently, this detection limit of a few atoms was pushed towards the mesoscopic regime [43] in a dedicated setup and combined with a state selective detection technique in a double-well potential [44]. Specifically the ability to accurately count atoms within an ensemble of mesoscopic size of highly entangled atoms will enable to approach Heisenberg scaling of the phase sensitivity for mesoscopic atom numbers in atom interferometers [45, 46]. The idea of combining these two experimental techniques in on apparatus is stands at the center of this work. Within the scope of this thesis, an apparatus that com-

bines an accurate atom counting detection and efficient entanglement creation has been designed and partially constructed. The presented thesis is structured as follows. The second chapter of this thesis gives introductions to three fields of research on ultracold atoms, where an accurate atom counting detection enables: Atom interferometry at the Heisenberg limit, the creation and characterization of few-particle Fock states and Bell tests. Chapter 3 reviews currently available detection techniques with respect to their ability to count single-atoms accurately. As a main result, the apparatus designed and build within the work of this thesis is presented in Chapter 4. The aspired experimental sequence is outlined and the implemented subsystems of the apparatus are characterized. In Chapter 5, as a second main result, the performance of the implemented accurate atom counting detection is tested. The stable and reproducible fluorescence time traces show single-particle resolution for atom numbers from 1 up to 30. Further, the noise analysis puts the limit of atoms detectable with single-atom counting to 390(20) atoms. Finally, Chapter 6 sums up the presented work and gives an outlook on the next steps in the construction of the experimental apparatus aiming towards becoming an entanglement-enhanced atom interferometer.

Chapter 2

Why to be an atom nit-picker

This first chapter outlines the motivation behind taking on the challenge of designing and building an experimental apparatus aims at combining all the tools and techniques needed to efficiently create large highly entangled quantum states with a single-atom detection. The first section describes the current limitations of atom interferometry and is a paramount example of the prospects that the combination of the aforementioned techniques offers. In fact, the outlined experiment is the reason for naming the apparatus the quantum-enhanced atom interferometer (QAI). The following two sections highlight uses of an accurate atom detection beyond atom interferometry. Detection and creation of atomic few particle Fock states will be enabled by the analogon to the single-photon detector. Further, tests of Bells inequality with spatially separated Bose-Einstein condensates can be accomplished with the aid of a single-atom detection.

2.1 The twin-Fock interferometer

Within this section, the basic physics of quantum interferometry are outlined using the example of a two-level quantum system pictured on the Bloch sphere. The naturally occurring boundaries, given by the *standard quantum limit* for coherent states and the *Heisenberg limit* for entangled states, are discussed. Overcoming the standard quantum limit in interferometric cold atom and ion experiments is a highly investigated task, with the goal of reaching the ultimate phase estimation precision at the Heisenberg limit for larger and larger particle numbers. Using the example of the entangled twin-Fock state, this section shows that in order to fully exploit the benefits of entangled states towards Heisenberg scaling, an accurate atom counting detection is needed. The combination of twin-Fock states created in a spinor Bose-Einstein condensate in conjunction

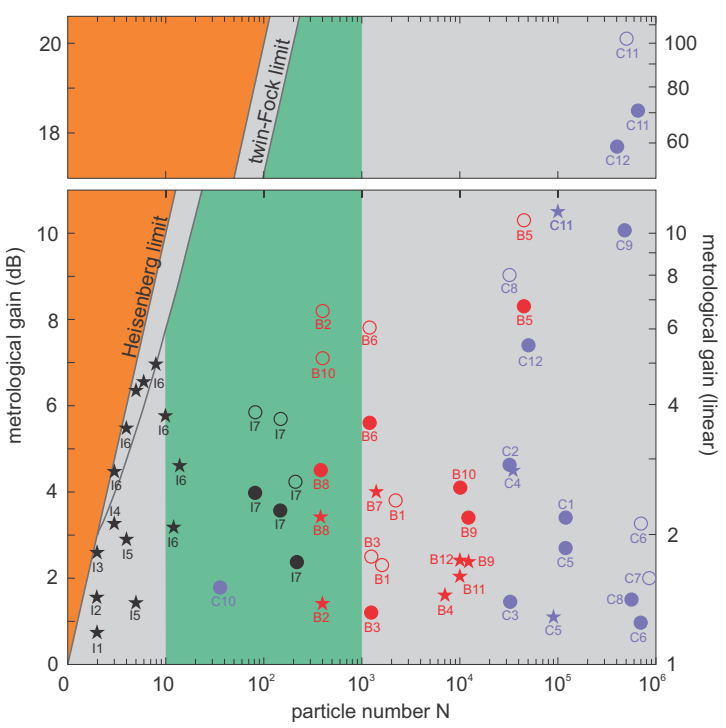

Trapped ions
I1 [47]Sackett et al., 2000
I2 [48]Meyer et al., 2001
I3 [49]Leibfried et al., 2003
I4 [50]Leibfried et al., 2004
I5 [51]Leibfried et al., 2005
I6 [52]Monz et al., 2011
I7 [29]Bohnet et al., 2016

Bose-Einstein condensates
B1 [30]Estève et al., 2008
B2 [32]Gross et al., 2010
B3 [33]Riedel et al., 2010
B4 [36]Lücke et al., 2011
B5 [53]Hamley et al., 2012
B6 [54]Berrada et al., 2013
B7 [55]Ockeloen et al., 2013
B8 [56]Muessel et al., 2014
B9 [57]Strobel et al., 2014
B10 [58]Muessel et al., 2015
B11 [59]Kruse et al., 2016
B12 [60]Zou et al., 2018

Cold thermal atoms
C1 [31]Appel et al., 2009
C2 [61]Leroux et al., 2010
C3 [62]Leroux et al., 2010
C4 [63]Louchet-Chauvet et al., 2010
C5 [64]Schleier-Smith et al., 2010
C6 [65]Chen et al., 2011
C7 [66]Sewell et al., 2012
C8 [67]Bohnet et al., 2014
C9 [68]Sewell et al., 2014
C10 [69]Barontini et al., 2015
C11 [70]Cox et al., 2016
C12 [16]Hosten et al., 2016

Figure 2.1 & Table 2.1: Overview of experimentally demonstrated interferometric sensitivity gain. Logarithmic (left vertical axis scaling as $10\log_{10}((\Delta\theta_{\mathrm{SQL}})^2/(\Delta\theta)^2)$ in dB) and linear (right vertical axis scaling as $(\Delta\theta_{\mathrm{SQL}})^2/(\Delta\theta)^2$) map of experimental demonstrations obtaining a phase sensitivity gain with respect to the standard quantum limit using trapped ions (black), Bose-Einstein condensates (red) and cold thermal atomic ensembles (violet). Stars reference full phase estimation experiments, filled cirlces an obtained gain by characterization of the underlying quantum state and open circles an inferred gain after substraction of technical and/or imaging noise. Corresponding publications are referenced in the accompanying table on the right. The Heisenberg limit is represented by the solid line bordering the physically unaccesible region in orange. While trapped ions follow the Heisenberg limit closely for particles numbers $N < 10$, beyond this experiments have not been able to achieve Heisenberg scaling. The experimental apparatus build within this work will incorperate the experimental techniques neccessary to access the area highlighted in green and allow for Heisenberg scaling with particle numbers beyond $N = 10$ based on the twin-Fock interferometer scheme presented in Ref. [36]. The lower gray line indicates the theoretical limit of the twin-Fock interferometer. Adapted from Ref. [28] and extended.

with such a detection can potentially outperform currently employed experimental schemes for particle numbers from 10 to 1000 (Fig. 2.1).

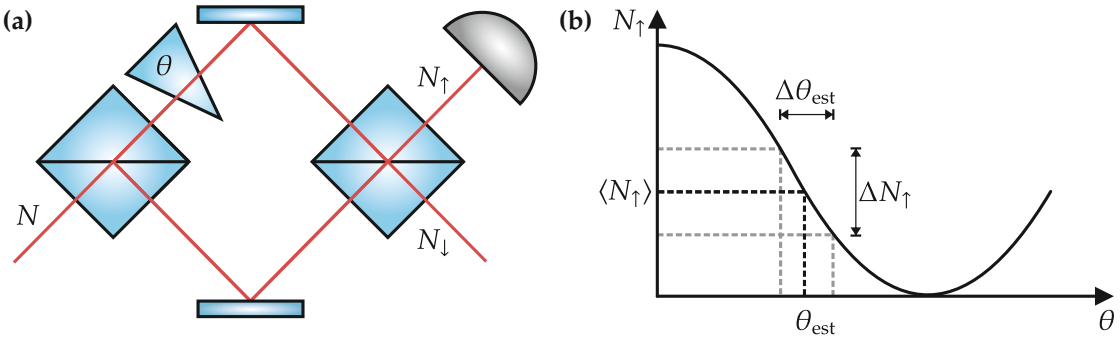

Figure 2.2: Classical interferometric experiment. **a** N independent particles enter the apparatus through one port of a balanced beam splitter, while the other port is left open. The beam splitter puts each particle in a superposition of following the upper path (state one $|\uparrow\rangle$) and the lower path (state two $|\downarrow\rangle$). A phase shift θ in the upper path only affects state one $|\uparrow\rangle$. A second beam splitter combines the two paths again, where the value of the phase shift will alter the number of particles $N_\uparrow$ ($N_\downarrow$) leaving the interferometer at the upper (lower) output port. **b** The relation between the atom number $N_\uparrow$ at the upper output port and the phase shift θ allows to estimate the experienced phase shift θ_{est} from the mean number $\langle N_\uparrow \rangle$ of atoms detected at the upper output port. The uncertainty $\Delta N_\uparrow$ of the atom number directly translates into a corresponding uncertainty $\Delta\theta_{\text{est}}$ of the estimated phase.

2.1.1 Interferometry and its limits

An interferometer is an experimental apparatus that transforms a probe state $\hat{\rho}_0$ based on the unknown value of a phase shift θ. The resulting output state $\hat{\rho}_\theta$ is detected and used to infer the value of the phase shift. While the phase shift itself is not measured directly, the choice of the measurement observable in combination with the input state is crucial as it will determine the sensitivity with which the phase shift can be estimated. Depending on the exact apparatus, the phase shift θ can be coupled to a multitude of physical quantities. This directly links improvements in phase estimation to improved sensor performance for a wide variety of applications in magnetometry [56, 66, 71], microwave characterization [55], gravimetry [72] and time-keeping [16].

The standard quantum limit

Consider an input state of N uncorrelated particles entering a Mach-Zehnder interferometer setup (Fig. 2.2 a) [73, 74]. A balanced beam splitter puts each particle into a superposition state of appearing on both output ports of the beam

splitter. The two spatially distinct paths can be considered as two spatially separated states or modes, labeled $|\uparrow\rangle$ and $|\downarrow\rangle$. One of them will experience an additional phase shift θ. Finally, the two states are being combined again by another balanced beam splitter. The outcome is measured in terms of the mean particle numbers $\langle N_\downarrow \rangle$ and $\langle N_\uparrow \rangle$ on the corresponding output ports of the second beam splitter. For the output port $|\uparrow\rangle$, both possible paths leading to it are perfectly symmetric with respect to the experienced reflections. Thus for a vanishing phase shift constructive interference causes each particle to appear on this output port. The full dependence of the appearance probability on the phase shift is given by $p_\uparrow = \cos^2(\theta/2)$ (Fig. 2.2 b). An estimation of this probability can be obtained by $p_{\uparrow,\mathrm{est}} = \langle N_\uparrow \rangle / N$, allowing to estimate the phase in the interferometer by using $\theta_{\mathrm{est}} = 2 \arccos\left(\sqrt{p_{\uparrow,\mathrm{est}}}\right)$. The error of this estimation can be calculated from the standard deviation $\Delta N_\uparrow = \sqrt{N p_\uparrow (1 - p_\uparrow)}$ of the binomially distributed particle number $N_\uparrow$ and reads [75]

$$\Delta\theta_{\mathrm{est}} = \frac{\Delta N_\uparrow}{\partial_\theta \langle N_\uparrow \rangle} = \frac{1}{\sqrt{N}}. \tag{2.1}$$

This equation describes a fundamental relation in quantum metrology and is known as the shot noise limit (SNL) or standard quantum limit (SQL). For repeated measurements, the estimation improves by a factor of $1/\sqrt{m}$, yielding

$$\Delta\theta_{\mathrm{est}}^{(\mathrm{SQL})} = \frac{1}{\sqrt{mN}}, \tag{2.2}$$

where m is the number of repetitions [76, 77]. This can be understood recalling the independence of the particles. In this idealized view, it does not matter if all the particles are employed in the interferometer within the same realization or sequentially. Repeating the measurement with single particles and averaging or running multiple particles in the same instance will yield the same precision. This insight about independent particles immediately bares a conceptual advance in interferometric sensitivity: the use of correlated or entangled particles.

The Heisenberg limit

While the previous assumption of uncorrelated particles invariably led to a binomial distribution of the measured atom number $N_\uparrow$, this changes drastically for correlated particles. Entangled quantum states can lead to more complex distributions with narrower features (Fig. 2.7), ultimately improving the phase estimation error. By applying the Heisenberg uncertainty between phase difference and particle number difference [78],

$$\Delta\theta \Delta (N_\uparrow - N_\downarrow) \geq 1, \tag{2.3}$$

a more fundamental precision limit can be derived under the assumption, that the maximum fluctuation in the particle number difference is given by $\Delta\left(N_{\uparrow} - N_{\downarrow}\right) = N$ [76, 77]:

$$\Delta\theta \geq \frac{1}{N}. \tag{2.4}$$

This relation is also known as the *Heisenberg limit* (HL), where the same scaling for m repeated measurements holds as for the SQL:

$$\Delta\theta^{(\mathrm{HL})} \geq \frac{1}{\sqrt{m}N}. \tag{2.5}$$

A simplified understanding of the origin of this limit can be gained by making the semiclassical argument, that the smallest change in the outcome of the experiment is given by the quantization of the probe, i.e. the particles. Therefore the limit set to the sensitivity of a phase measurement can at best scale inversely with the number N of employed particles.

A more rigorous approach to estimation limitations like the SQL and HL makes use of the more general concepts of the *Fisher information* (FI) [79, 80] and the *Cramér-Rao* bound (CR) [81, 82]. In the context of quantum measurements the *quantum Cramér-Rao* bound has been introduced [83]

$$\Delta\theta_{\mathrm{est}}^{(\mathrm{QCR})} \geq \frac{1}{\sqrt{mF_Q\left[\rho_0, \hat{\boldsymbol{J}}_{\vec{n}}\right]}}, \tag{2.6}$$

where m is again the number of independent measurements and F_Q is the *quantum Fisher information* (QFI). The quantum Fisher information depends on the input state ρ_0 of the interferometric evolution described by $\hat{\boldsymbol{J}}_{\vec{n}}$, as well as the optimal choice of the measurement observable. It serves as an upper limit to the Fisher information and reflects the best possible phase sensitivity for the given state. A potential improvement in phase sensitivity compared to the standard quantum limit can be written in the form

$$\Delta\theta_{\mathrm{est}} \geq \frac{\chi}{\sqrt{N}} \tag{2.7}$$

where the achieved quantum-enhancement is quantified by the parameter

$$\chi^2 = \frac{N}{F_Q}. \tag{2.8}$$

The QFI uniquely links entanglement and metrological gain in the condition $\chi^2 < 1$ [84]. From a comparison of Eqn. 2.2 and Eqn. 2.6 it becomes apparent, that states with $F_Q > N$ provide entanglement that can be used to surpass the the standard quantum limit. Any state providing a QFI content that fulfills $F_Q > N$ is thus useful for metrological purposes. The QFI is bound by $F_Q < N^2$ underlining the validity of the Heisenberg limit (Eqn. 2.5).

2.1.2 The Bloch sphere

The theory of two-level quantum systems or qubits is one of the most fundamental constituents of quantum mechanical physics. Despite its seemingly theoretical simplicity it allows for a feature rich representation of quantum phenomena and experimental techniques, including two-mode interferometers. A very intuitive geometrical depiction of these kinds of systems is the *Bloch sphere* (Fig. 2.3).

The single-particle Bloch sphere

In analogy to a spin-1/2 particle the orthonormal state basis of a single particle in a two-level system is often depicted as $|\uparrow\rangle$ for one level and $|\downarrow\rangle$ for the other. The direction of the associated spin orientation is commonly chosen to be the z direction. The basis states $|\uparrow\rangle$ and $|\downarrow\rangle$ thus must be the eigenstates to the corresponding spin measurement operator. A spin measurement in this picture is defined by the (pseudo) spin operators $\hat{s}_x$, $\hat{s}_y$ and $\hat{s}_z$ [78], measuring along the orthonormal directions x, y and z, respectively. They can be defined using the Pauli matrices $\hat{\sigma}_k$ [85] and $s = 1/2$ as

$$\begin{aligned} \hat{s}_x &= \tfrac{1}{2}\left(|\downarrow\rangle\langle\uparrow| + |\uparrow\rangle\langle\downarrow|\right) &&= s\hat{\sigma}_x \\ \hat{s}_y &= \tfrac{1}{2i}\left(|\downarrow\rangle\langle\uparrow| - |\uparrow\rangle\langle\downarrow|\right) &&= s\hat{\sigma}_y \\ \hat{s}_z &= \tfrac{1}{2}\left(|\uparrow\rangle\langle\uparrow| - |\downarrow\rangle\langle\downarrow|\right) &&= s\hat{\sigma}_z \quad . \end{aligned} \tag{2.9}$$

The operators $\hat{s}_k$ thus fulfill the commutation relations

$$[\hat{s}_k, \hat{s}_l] = i\epsilon_{klm}\hat{s}_m, \tag{2.10}$$

similar to the Pauli matrices, where ϵ_{klm} is the *Levi-Civita tensor*. Using the spin-up and spin-down basis every possible normalized pure state of the system can be written as a superposition in the form

$$\left|\psi\right\rangle = \left|\varphi, \vartheta\right\rangle = e^{i\varphi/2}\cos(\vartheta)\,|\uparrow\rangle + e^{-i\varphi/2}\sin(\vartheta)\,|\downarrow\rangle\,, \tag{2.11}$$

where $0 \leq \varphi < 2\pi$ describes the relative phase and the sinusoidal prefactors with $-\frac{\pi}{2} \leq \vartheta < \frac{\pi}{2}$ quantify the relative occupation of the two basis states. The mean value of the spin operators is given in vectorial notation by

$$\langle \hat{\boldsymbol{s}} \rangle = \begin{pmatrix} \langle \hat{s}_x \rangle \\ \langle \hat{s}_y \rangle \\ \langle \hat{s}_z \rangle \end{pmatrix} = \frac{1}{2}\begin{pmatrix} \sin 2\vartheta \cos\varphi \\ \sin 2\vartheta \sin\varphi \\ \cos 2\vartheta \end{pmatrix} = \vec{s} \tag{2.12}$$

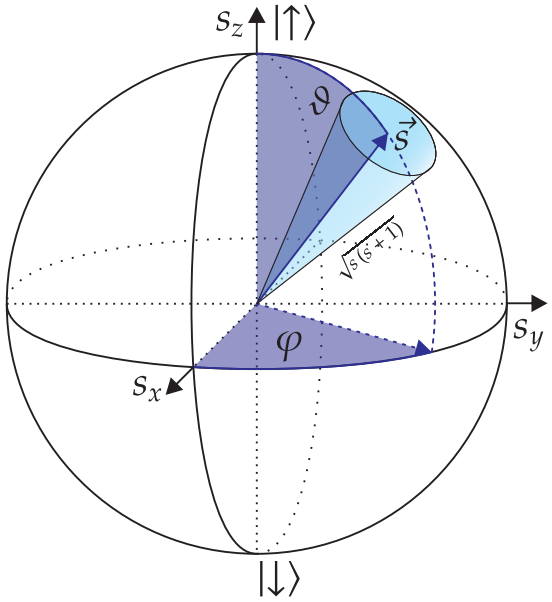

Figure 2.3: Single particle spin state Bloch sphere. Top and bottom of the sphere can be associated with the basis states $|\uparrow\rangle$ and $|\downarrow\rangle$, respectively. A single spin-1/2 state is best described by a cone, the center of which represents the spins mean orientation $\langle\hat{\boldsymbol{s}}\rangle = \vec{s}$ as a vector, oriented according to the angles ϑ and φ, on the surface of the Bloch sphere. The uncertainty of the spins orthogonal components is visualized as the opening disk spanning across the wide end of the cone (not to scale with respect to the sphere). The spin's length is given by $\sqrt{s\,(s+1)}$.

and its length is $|\vec{s}| = 1/2$. This spherical coordinate parameterization of the mean spin vector is referred to as the *Bloch vector* and lends itself directly to a sphere representation with a radius of 1/2, the *Bloch sphere* (Fig. 2.3). The poles of the Bloch sphere can be identified with the basis states $|\uparrow\rangle$ and $|\downarrow\rangle$. Every pure state's spin expectation value can now be interpreted as a point on the Bloch sphere's surface[1]. But the total quantum mechanical spin $\hat{\boldsymbol{s}}$ of length

$$|\hat{\boldsymbol{s}}| = \sqrt{\langle\hat{\boldsymbol{s}}^2\rangle} = \sqrt{s\,(s+1)} = \sqrt{3/4} \tag{2.13}$$

is best described by a cone around its mean value $\vec{s}$, such that the projection onto the cone's axis matches the expectation value of $|\langle\hat{\boldsymbol{s}}\rangle| = 1/2$. This behavior can be understood as a direct result of the non-vanishing commutator relations (Eqn. 2.10) between the different spin components, which lead to Heisenberg

[1] A mixed state $\hat{\rho} = (\mathbb{1} + r\vec{s}\cdot\hat{\boldsymbol{\sigma}})$ can be viewed as an object within the sphere, where the length of the effective state vector is given by $0 \leq r \leq 1$.

uncertainty relations of the form[2]

$$(\Delta s_y)^2(\Delta s_z)^2 \geq \frac{1}{4}\left|\langle \hat{s}_x \rangle\right|^2 . \tag{2.14}$$

This relation holds for any direction the spin could be pointing in (in this case $\hat{s}_x$) with respect to the corresponding orthogonal directions (in this case $\hat{s}_y$ and $\hat{s}_z$). Within this picture the opening disc of the cone thus represents the uncertainty of the spin components orthogonal to its mean direction. The size of the disc can be derived from an example, assuming that the spin is orientated along $\hat{s}_x$ and the fluctuations are symmetric in $\hat{s}_y$ and $\hat{s}_z$. As a direct consequence of this it follows that $\langle \hat{s}_x \rangle = 1/2$. The bestcase scenario of uncertainty relation Eq. 2.14 thus yields $\Delta s_{y/z} = 1/2$.

The multi-particle Bloch sphere

When considering not only one single spin but many spins, a very similar depiction holds true. By adding the individual spin contributions of N particles within the considered ensemble, a collective spin can be defined as

$$\hat{\boldsymbol{J}} = \sum_{m=1}^{N} \hat{\boldsymbol{s}}^{(m)} \tag{2.15}$$

where $\hat{\boldsymbol{s}}^{(m)}$ is the single particle spin vector[3] of the m-th particle. Once more the commutation relations from Eqn. 2.10 will hold for the newly defined spin operators

$$\left[\hat{J}_k, \hat{J}_l\right] = i\epsilon_{klm}\hat{J}_m, \tag{2.16}$$

immediately yielding the associated uncertainty relations

$$(\Delta J_k)^2(\Delta J_l)^2 \geq \frac{1}{4}\left|\langle \hat{J}_m \rangle\right|^2 . \tag{2.17}$$

Only considering the case of states that are symmetric with respect to particle exchange allows for writing the spin length as

$$\left|\hat{\boldsymbol{J}}\right| = \sqrt{J(J+1)} = \sqrt{\frac{N}{2}\left(\frac{N}{2}+1\right)} \overset{N\gg 1}{\approx} \frac{N}{2}, \tag{2.18}$$

[2]The uncertainty of the spin operators is defined following the textbook standard as $(\Delta s_i)^2 = \langle\psi\left|(\hat{s}_i - \langle \hat{s}_i \rangle)^2\right|\psi\rangle$

[3]The one of which the mean value has been derived in Eqn. 2.12.

where the collective spin is at its maximum $J = N/2$ and the last approximation assumes large particle numbers N. States of this kind can now be visualized by means of a generalized multi-particle Bloch sphere representing all possible collective spins $\hat{\boldsymbol{J}}$ (Fig. 2.4). A state aligned to either pole of the sphere has all spins within the ensemble pointing along $|\uparrow\rangle$ or $|\downarrow\rangle$, respectively. Thus, it is intuitive that $\hat{J}_z$ is given by the difference of the populations $\hat{N}_\uparrow$ and $\hat{N}_\downarrow$ of the respective single particle states:

$$\hat{J}_z = \frac{1}{2}\left(\hat{N}_\uparrow - \hat{N}_\downarrow\right). \tag{2.19}$$

Again the collective spin is best represented by a mean direction with a cone around it and an uncertainty disc at its end. As well as for the single spin consideration an example helps to estimate the uncertainty represented by Eq. 2.17. Assuming all N contributing spins are aligned along $\hat{s}_x^{(m)}$, such that $\langle \hat{s}_x^{(m)} \rangle = 1/2$ for all $m = 1, \ldots, N$ forms a state that is called the *coherent spin state* and posses a collective spin that also points into the x direction where

$$\langle \hat{J}_x \rangle = \sum_{m=1}^{N} \langle \hat{s}_x^{(m)} \rangle = \frac{N}{2} = J. \tag{2.20}$$

Assuming there are no correlations between the particles allows to set $\Delta J_y = \Delta J_z$. Employing Eq. 2.17 yields a minimum uncertainty of $\Delta J_{y/z} = \sqrt{N}/2$. Eq. 2.19 reveals a linear relationship between the population imbalance and $\hat{J}_z$, such that

$$\Delta\left(N_\uparrow - N_\downarrow\right) = 2\Delta J_z = \sqrt{N}. \tag{2.21}$$

This particle number uncertainty can be linked to the phase uncertainty to retrieve the fundamental scaling relations for the phase sensitivity from equation 2.1. To reveal this connection the mean collective spin can be written in vectorial form, as has been done for the single spin in Eq. 2.12, i.e.

$$\langle \hat{\boldsymbol{J}} \rangle = \begin{pmatrix} \langle \hat{J}_x \rangle \\ \langle \hat{J}_y \rangle \\ \langle \hat{J}_z \rangle \end{pmatrix} = r \begin{pmatrix} \sin 2\vartheta \cos\varphi \\ \sin 2\vartheta \sin\varphi \\ \cos 2\vartheta \end{pmatrix} = \vec{J}, \tag{2.22}$$

with the mean spin length r. Choosing $\varphi = \varphi_\uparrow - \varphi_\downarrow = 0$ without loss of generality and approximating for small phases φ this leads to the relations

$$\begin{aligned} \langle \hat{J}_x \rangle &= r \sin 2\vartheta \\ \Delta J_y &\approx r \sin 2\vartheta \Delta\varphi \end{aligned} \tag{2.23}$$

These results together with the commutation relations from Eq. 2.17 yield

$$\Delta\left(N_\uparrow - N_\downarrow\right)\Delta\varphi \geq 1 \tag{2.24}$$

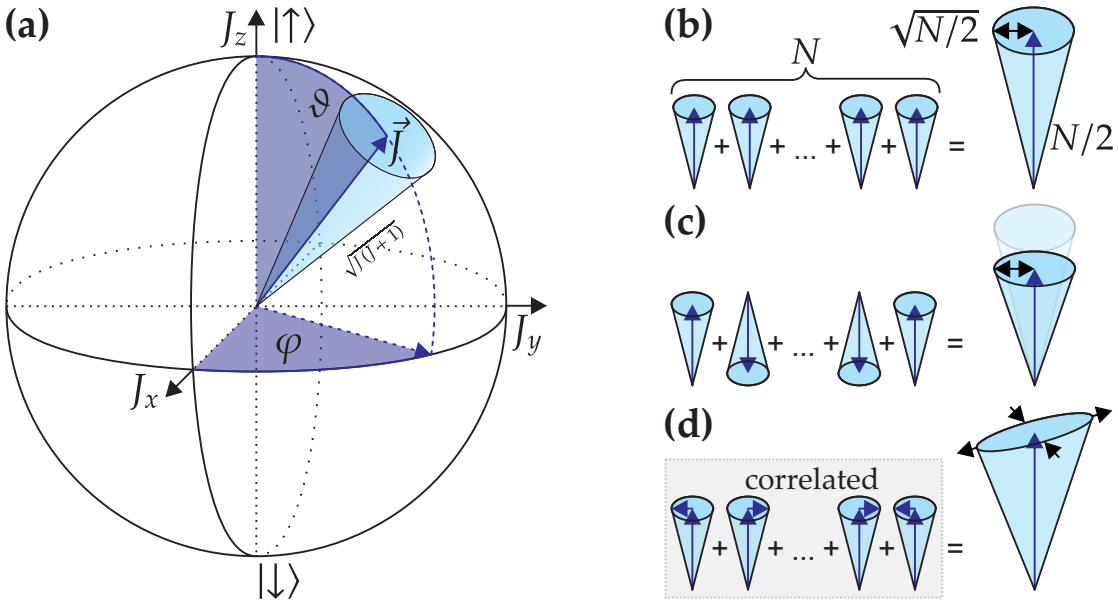

Figure 2.4: Multi particle spin state Bloch sphere and collective spin formation. **a** The collective spin state of N spin-1/2 particles is best described by a cone, the center of which represents the spins mean orientation $\langle \hat{\boldsymbol{J}} \rangle = \vec{J}$ as a vector on the surface of the Bloch sphere. The collective uncertainty of the spins' orthogonal components is visualized as the opening disk spanning across the wide end of the cone. The spins' length in the case of symmetry with respect to particle exchange is $\sqrt{J(J+1)}$. **b** A collection of (indistinguishable) spins all residing in the identical pure single spin state form a symmetric polarized or coherent spin state of maximum spin length. **c** A collection of distinguishable spins can form a non-symmetric collective spin of reduced spin length. **d** A spin-squeezed state is the result of correlations between the individual spins, featuring reduced fluctuations along one direction while the other direction suffers from increased fluctuations.

as the relation between number and phase uncertainties, showing that at the expense of either phase or number fluctuations, the respective other can be improved upon. Figure 2.4d already mentions the spin-squeezed states that exploit this behaviour to gain advantageous scaling of the phase sensitivity.

2.1.3 The interferometer on the Bloch sphere

The Bloch sphere picture does not only cover the states themselves but can be used to depict state manipulation and dynamics as well (Fig. 2.5 a-d). In

particular, the representation of an interferometric sequence for a given input state can help to gain a visual understanding of the states' distinctive features and useful metrological properties. In order to compose an interferometric sequence, at least two ingredients are needed: the beam splitters and the phase shift. Both can be derived from the single-particle representation and extended to the multi-particle representation [86].

Firstly, the resulting transformation for the beam splitter reads

$$\hat{\boldsymbol{J}} = \begin{pmatrix} \hat{J}_x \\ \hat{J}_y \\ \hat{J}_z \end{pmatrix} \rightarrow \begin{pmatrix} 1 & 0 & 0 \\ 0 & \cos\alpha & -\sin\alpha \\ 0 & \sin\alpha & \cos\alpha \end{pmatrix} \begin{pmatrix} \hat{J}_x \\ \hat{J}_y \\ \hat{J}_z \end{pmatrix}, \tag{2.25}$$

where the angle α defines the splitting ratio of the beam splitter. A balanced 50:50 beam splitter is obtained for $\alpha = \pi/2$. In the Schrödinger representation for a given input state $\left|\psi\right\rangle_{\text{in}}$ the output state of the beamsplitter action reads

$$\left|\psi\right\rangle_{\text{out}} = \exp\left(-i\alpha\hat{J}_x\right)\left|\psi\right\rangle_{\text{in}}. \tag{2.26}$$

On the Bloch sphere this results in a rotation of any given input state around the J_x axis[4] (Fig. 2.5 b).

Secondly, the transformation representing the phase shift can be written as

$$\hat{\boldsymbol{J}} = \begin{pmatrix} \hat{J}_x \\ \hat{J}_y \\ \hat{J}_z \end{pmatrix} \rightarrow \begin{pmatrix} \cos\theta & -\sin\theta & 0 \\ \sin\theta & \cos\theta & 0 \\ 0 & 0 & 1 \end{pmatrix} \begin{pmatrix} \hat{J}_x \\ \hat{J}_y \\ \hat{J}_z \end{pmatrix}, \tag{2.27}$$

where θ represents the added relative phase. The Schrödinger picture in this case is given by

$$\left|\psi\right\rangle_{\text{out}} = \exp\left(-i\theta\hat{J}_z\right)\left|\psi\right\rangle_{\text{in}}. \tag{2.28}$$

Just like the beam splitting action, this phase shift transformation can be understood in terms of state rotations on the Bloch sphere, only this time around the J_z axis.

Hence, the full interferometric action, consisting of a balanced beam splitting process, a phase shift and a recombining balanced beam splitter, on a collective spin state is given in terms of a multiplication of the corresponding matrices, yielding

$$\hat{\boldsymbol{J}} = \begin{pmatrix} \hat{J}_x \\ \hat{J}_y \\ \hat{J}_z \end{pmatrix} \rightarrow \begin{pmatrix} \cos\theta & 0 & \sin\theta \\ 0 & -1 & 0 \\ \sin\theta & 0 & -\cos\theta \end{pmatrix} \begin{pmatrix} \hat{J}_x \\ \hat{J}_y \\ \hat{J}_z \end{pmatrix}. \tag{2.29}$$

[4] A representation that results in rotation around the J_y axis can also be given and is equally valid. For simplicity, the J_x representation will be chosen within the context of this work.

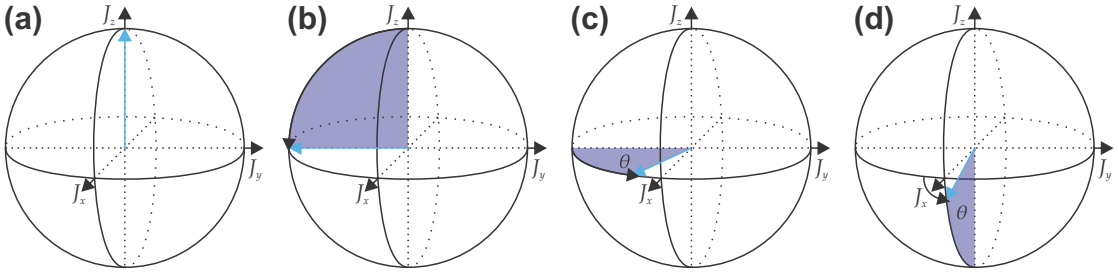

Figure 2.5: Stepwise depiction of a standard interferometric sequence on the Bloch sphere. **a** The initial input state is prepared along the J_z direction, as depicted by the blue vector. **b** A balanced beam splitter acts as a $\pi/2$ rotation around the J_x axis and aligns the state vector with the J_y axis in the equatorial plane. **c** The phase evolution θ is represented by a rotation around J_z. A full turn would correspond to a phase shift of $\theta = 2\pi$. Illustrated is a phase shift close to $\theta = \pi/2$, almost aligning the state vector with the J_x axis. **d** A final balanced beam splitting operation turns the state around the J_x axis. The resulting output state is slightly offset from the J_x axis in the J_x-J_z plane. The last operation turned the imprinted phase into a measurable population difference between the two involved single particle states $|\uparrow\rangle$ and $|\downarrow\rangle$.

This shows that the combined action of the interferometer can be understood as a collective rotation of the state around the generalized Bloch sphere's J_y axis. The Schrödinger representation allows to summarize the whole interferometric sequence into one operator $\hat{U}_{\mathrm{IS}}$ that acts on the input state $\left|\psi\right\rangle_{\mathrm{in}}$ as

$$\begin{aligned} \left|\psi\right\rangle_{\mathrm{out}} &= \hat{U}_{\mathrm{IS}} \left|\psi\right\rangle_{\mathrm{in}} \\ &= \exp\left(-i\tfrac{\pi}{2}\hat{J}_x\right)\exp\left(-i\theta\hat{J}_z\right)\exp\left(-i\tfrac{\pi}{2}\hat{J}_x\right)\left|\psi\right\rangle_{\mathrm{in}} \\ &= \begin{pmatrix} i\sin\frac{\theta}{2} & \cos\frac{\theta}{2} \\ \cos\frac{\theta}{2} & i\sin\frac{\theta}{2} \end{pmatrix}\left|\psi\right\rangle_{\mathrm{in}}. \end{aligned} \tag{2.30}$$

Coherent state interferometry

While the coherent spin state has already been introduced in the context of its representation on the generalized Bloch sphere, it is also the most common starting point for looking at the interplay of a state's phase sensitivity and the interferometric sequence described above. Its mathematical representation in terms of the single particle spin states is given by

$$\left|\vartheta, \varphi, N\right\rangle = \bigotimes_{m=1}^{N}\left[\cos\vartheta\left|\uparrow\right\rangle_m + e^{i\varphi}\sin\vartheta\left|\downarrow\right\rangle_m\right]. \tag{2.31}$$

Simply making use of the fact that the interferometric sequence acts like a rotation around the y-axis on the Bloch sphere (Fig. 2.6), shows that a change in the

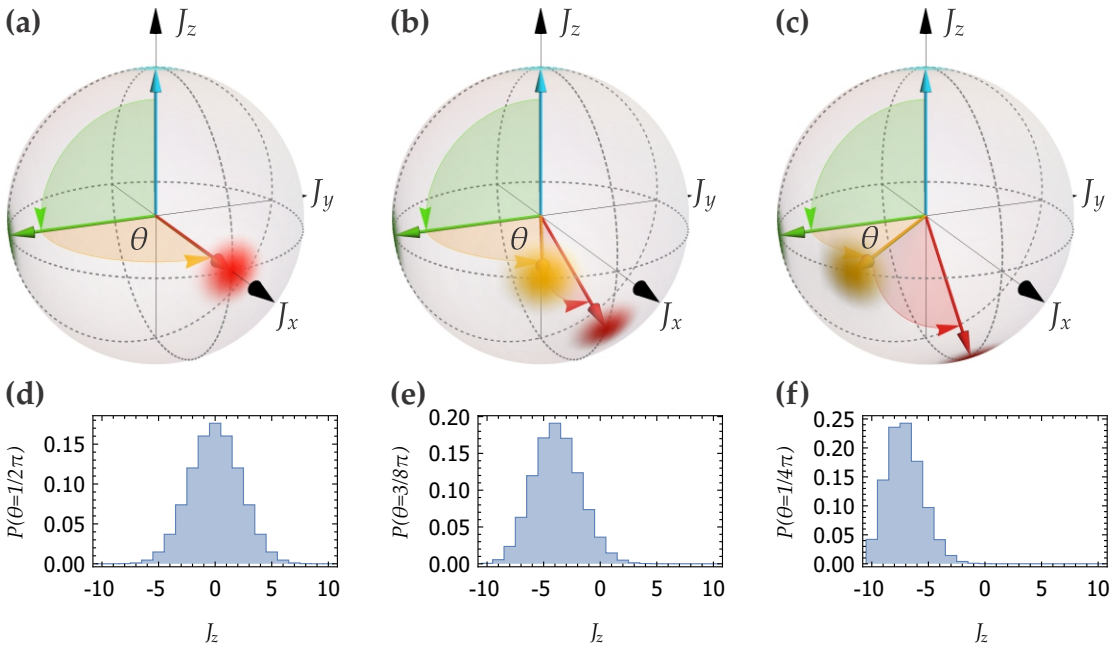

Figure 2.6: Depiction of standard interferometric sequences using a coherent spin state and the resulting distributions of detectable population imbalances J_z for different values of the experienced phase shift θ. In each case (**a** $\theta = \pi/2$, **b** $\theta = 3\pi/8$, **c** $\theta = \pi/4$) the interferometric sequences undergo the same three steps, involving four different states in the process (including the initial state), all depicted on the same Bloch sphere. The colored vectors represent the mean spin orientation of the state while the accordingly colored distributions on the spheres surfaces depict the Husimi distribution of the state. The initial state is colored in blue, always orientated along the J_z axis. The beam splitting process turns the state to the equator (green) where a phase θ is acquired (orange). The combining beam splitter operation turns the state from the equator into the J_x-J_z-plane (red). The projection of the state onto the J_z axis is the measured output of the interferometer and is accessed experimentally by the observed occupation difference of the single particle states $|\uparrow\rangle$ and $|\downarrow\rangle$. **d-f** Corresponding J_z distributions are shown below for a coherent spin state consisting of $N = 10$ particles. A change in phase θ simple shifts the distribution. Its mean can be used as an estimator for the underlying phase change.

acquired phase θ can be measured indirectly by measuring the states $\langle \hat{J}_z \rangle$, i.e. the population imbalance between $|\uparrow\rangle$ and $|\downarrow\rangle$. For both the initial and the final state this measurement is a projection of the state onto the z-axis, resulting in a Gaussian distribution. The corresponding shift of the mean value between final and initial state acts as a measure for the acquired phase. Coherent spin states possess a quantum Fisher information that is given by $F_Q = N$, making it exactly

fulfill the SQL (Eq. 2.2).

Twin-Fock state interferometry

In contrast to the coherent spin state, the twin-Fock state is a highly entangled quantum state and belongs to the family of Dicke states. While Dicke states in general feature a well defined number of atoms in the $|\uparrow\rangle$ and $|\downarrow\rangle$ state, the twin-Fock state features the exact same amount of atoms in both states:

$$|m_z\rangle_{\text{Dicke}} = |N/2 + m\rangle_\uparrow \, |N/2 - m\rangle_\downarrow = |N/2 + m, N/2 - m\rangle \tag{2.32}$$

$$|m_z\rangle_{\text{TF}} = |N/2, N/2\rangle \, . \tag{2.33}$$

In turn, the vanishing population difference $N_\uparrow - N_\downarrow = 0$ and the vanishing mean collective spin $\langle \hat{\boldsymbol{J}} \rangle = (0, 0, 0)^{\text{T}}$ cause the phase ϑ to be completely undefined as it is not possible to assign an angle between mean spin and J_x-axis. These characteristics are best described by a ring around the equator of the Bloch sphere (Fig. 2.7 a-c). The quantum Fisher information for a Dicke state reads [28]

$$F_Q \left[|m_z\rangle \, , \hat{\boldsymbol{J}}_\perp \right] = \frac{N^2}{2} - 2m^2 + N, \tag{2.34}$$

implying that in case of a twin-Fock state (i.e. $m = 0$) Heisenberg scaling $F_Q \propto N^2$ can be achieved. While the statement, that a state without a well defined phase should be useful for phase estimation appears counterintuitive at first, it becomes clear once the interferometric sequence is applied step by step (Fig. 2.7). Already the first beam splitter turns the ring from its horizontal orientation at the equator by 90 degrees into a vertical position. This immediately converts the well defined population difference into a precisely defined phase at the cost of largely increased fluctuations in the population difference. The phase accumulation now turns the ring around the J_z-axis of the Bloch sphere before the second beam splitting process turns the state around the J_x-axis again. Once the interferometric sequence is completed, the population difference can be measured, acting as a projection of the state onto J_z. As opposed to the coherent state, for the twin-Fock state the mean value $\langle \hat{J}_z \rangle$ of the resulting distribution cannot serve as a measure of the phase shift θ since it does not depend on it. Indeed this holds true for the mean values of each collective spin component $\langle \hat{J}_z \rangle = \langle \hat{J}_y \rangle = \langle \hat{J}_x \rangle = 0$ for all possible turning angles on the Bloch sphere. But the phase shift ϑ in this case has an even more dramatic influence on the distribution. It changes its overall shape rather than only shifting it. Exactly this type of influence is captured well by the Fisher information, as it quantifies the observable's probability distribution's rate of change with respect to a change in the phase. This implies the need for a more advanced phase estimation scheme

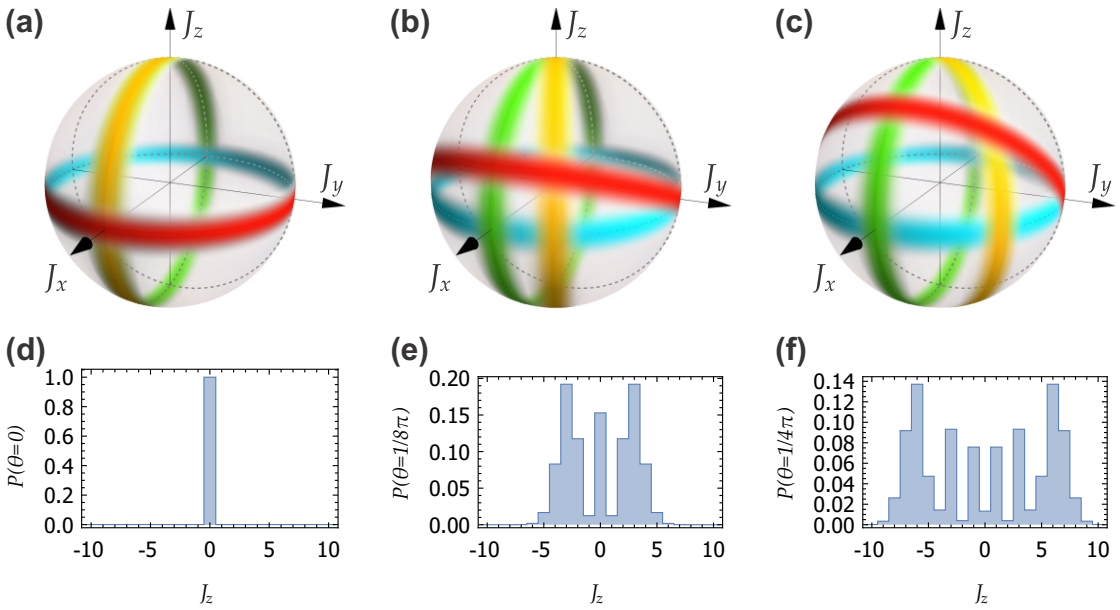

Figure 2.7: Depiction of standard interferometric sequences for a twin-Fock input state and the resulting distributions of detectable population imbalances J_z for different values of the experienced phase shift θ. In each case (**a** $\theta = 0$, **b** $\theta = \pi/8$, **c** $\theta = \pi/4$) the interferometric sequences undergo the same three steps, involving four different states in the process (including the initial state), all depicted on the same Bloch sphere using their Husimi distribution. The initial state (blue) is located on the equator. A first beam splitting operation turns it upright (green). Now the narrow feature of the distribution is orientated along the direction of phase accumulation, making the twin-Fock state highly sensitive to phase changes (yellow). A final beam splitting operation turns the ring one more time (red). As for the initial state, the narrow width of the distribution is orientated along the J_z axis translating the phase change into a change in occupation number. **d-f** Below, the resulting J_z distribution for each case are shown for a twin-Fock state consisting of $N = 20$ particles. These distributions always stay centered around the same mean value, rendering the mean useless for the estimation of the underlying phase.

[87, 88]. The width $(\Delta J_z)^2 = \langle J_z^2 \rangle$ of the distribution is one way to track a change in the phase θ [36, 46, 88]. To date, a twin-Fock interferometer has been realized in photonic [89, 90] and ionic [48] systems. An accompanying sensitivity increase of 1.61 dB below the standard quantum limit for a bosonic system has also been demonstrated experimentally at an optimal phase shift of 15 mrad using a twin-Fock state created by spin changing collisions of 7000 ^{87}Rb atoms within a Bose-Einstein condensate [36]. These results were mainly limited by the experiment's detection system that offered a counting uncertainty of about

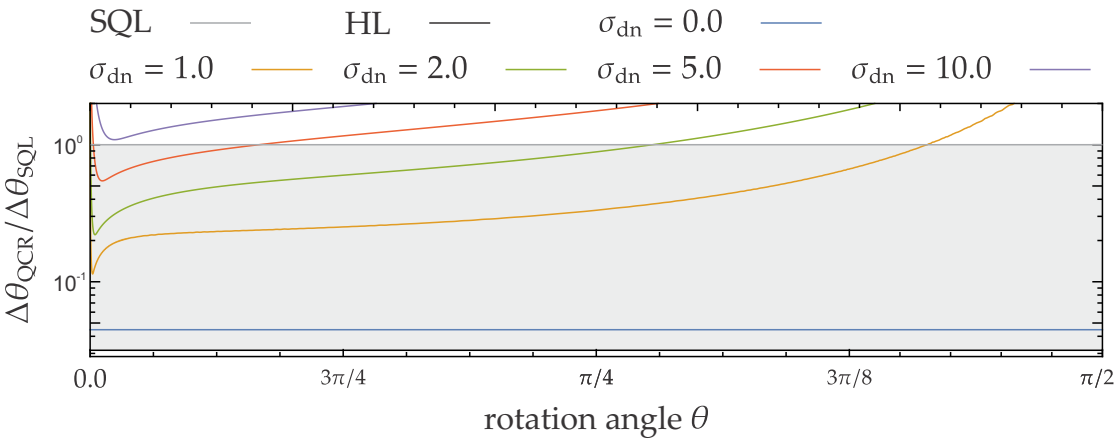

Figure 2.8: The quantum Cramer-Rao bound on the phase estimation for the twin-Fock state and achievable phase sensitivities limited by detection noise. This graph shows the phase sensitivity for a twin-Fock interferometer based on its Fisher information for different levels of detection noise depending on the rotation angle θ within the interferometer for $N = 1000$ atoms. The standard quantum limit (SQL) and Heisenberg limit (HL) are shown as a dashed black and a solid black line, respectively. The grey shaded area between these two lines marks the region of fundamental improvement below the SQL. The solid curves depict the expected phase sensitivity for different levels of detection noise. While a detection noise of $\sigma_{dn} = 10$ (violet) would not allow to break the SQL, a detection noise of $\sigma_{dn} = 5$ (red) already reaches below the SQL. Even better is the performance of a detection noise $\sigma_{dn} = 1$ (orange), where a wide range of rotation angles can be detected with a sensitivity below the SQL. Decreasing the detection noise even further allows to scale towards the true quantum Cramer-Rao bound of the twin-Fock state for vanishing detection noise $\sigma_{dn} = 0$ (blue).

$\sigma_{dn} = 20$ atoms. A detection that provides single atom counting precision could immediately push the limit for the phase sensitivity towards the Heisenberg limit for the range of small phase shifts. Beyond that, the full counting statistics of the final state $|\psi\rangle_{out}$ would be revealed, ultimately allowing to use the shape of the entire distribution for phase estimation purposes (Fig. 2.7 lower panel). A striking feature of this distribution is, that given a symmetric mixing of the two modes with a $\pi/2$-pulse, only odd or only even numbers of atoms can be observed at the output ports, depending on the phase shift within the interferometer. This leads to a strong dependence of the parity on the phase shift close to multiples of $\theta = \pi/2$ and in fact a parity measurement is sufficient to achieve Heisenberg scaling [45, 91, 92]. This behaviour is a many-particle variant of the two-particle Hong-Ou-Mandel effect, first observed on photons [93]. Eventually, a detection that performs at a single atom counting level will fully unlock the potential of the experimental concept of a twin-Fock interferometer, as it will

allow to satisfy the Cramer-Rao bound for the twin-Fock state and push the phase sensitivity towards the fundamental Heisenberg limit for a broad range of the phase values θ (Fig. 2.8) by using either a Bayesian method or a maximum likelihood estimator [87, 94, 95].

2.2 Characterization and reconstruction of non-classical quantum states

Harnessing the power of non-classical quantum states for the purposes of quantum information technology implies the need for full knowledge of and control over those states, from creation and characterization to manipulation and interpretation. In photonic systems a wide variety of fundamental non-classical quantum states have been realized and characterized experimentally [96]. A particular highlight is the creation of heralded single-photon, two-photon and even three-photon Fock states as well as the reconstruction of their corresponding Wigner functions and density matrices by means of homodyne quantum tomography [97–100]. Further the photon-added coherent state [101, 102] first characterized the result of the action of the bosonic creation operator on a coherent state. Beyond this characterization of quantum states goes the concept of quantum process tomography of the creation and annihilation operators for single photons [103]. This progress is enabled by three key techniques and technologies available to photonic quantum optics: optical homodyne tomography [104], parametric down conversion [105, 106] and efficient single photon detectors. Homodyne detection has been demonstrated for atomic systems [107] and has been used to implement an interaction free measurement scheme based on the quantum Zeno effect [108]. Spin dynamics in spinor Bose-Einstein condensates are spontaneously occurring spin changing collisions that can be understood as the atomic analogon to optical parametric down conversion [109]. They similarly create excitation pairs of opposing spin orientation, ultimately generating entanglement in between the particles. It is the efficient detection of single atoms that is needed in order to not only translate the progress in creation and characterization of quantum states from photonic systems onto atomic systems, but also to access the benefits that atomic systems can offer when it comes to the synthesis of non-classical quantum states. This section outlines the necessary concepts and techniques to advance the characterization of fundamental atomic quantum states.

2.2.1 The Wigner function

For a classical particle, the simultaneous determination of position and momentum allows to depict its state as an exact point in phase space. An ensemble of

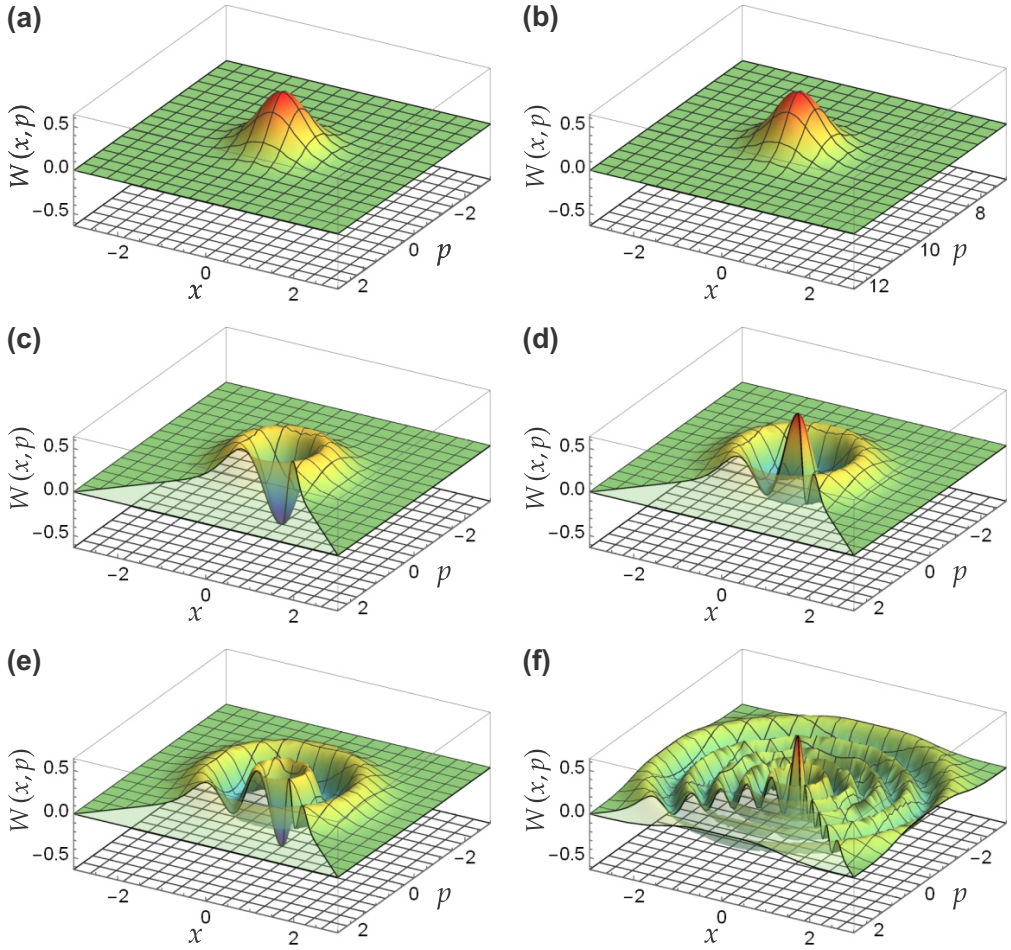

Figure 2.9: Wigner Functions. This panel shows the Wigner functions of a few exemplary quantum states. **a** The vacuum state $|0\rangle$ forms a gaussian distribution around the origin. **b** A coherent state for $\bar{n} = 10$ particles is created by displacing the vacuum state but maintains its gaussian shape. **c-f** Fock states $|n\rangle$ with a defined particle number n show oscillating characteristics while still being centered and symmetric with respect to the origin. **c** Most strikingly already for a single particle state $|1\rangle$, the Wigner function takes on negative values. Similar features are seen for two, three and 10 particles ($|2\rangle$ in **d**, $|3\rangle$ in **e** and $|10\rangle$ in **f**). The number of oscillations is determined by the number of particles.

classical particles is best described by a probability distribution, the Liouville density, that quantifies the likeliness of finding a particle with a given combination of position and momentum. For quantum-mechanical particles, this kind of description cannot be readily adopted, since the uncertainty relation forbids a simultaneous determination of position and momentum, necessitating the use

of a quasi-probability distribution for even a single particle. The Wigner function takes over this role[78, 110, 111]. For an arbitrary density operator $\hat{\rho}$, the Wigner function is defined as

$$W(x,p) = \frac{1}{2\pi\hbar}\int_{-\infty}^{\infty}\left\langle x+\frac{1}{2}x'\right|\hat{\rho}\left|x-\frac{1}{2}x'\right\rangle e^{ipx'/\hbar}\,dx', \tag{2.35}$$

where $\left|q\pm\frac{1}{2}x\right\rangle$ are the eigenstates of the position operator[5]. Since it is linked to a state's density matrix it can readily be used to calculate any property of the quantum state, such as its quadratures which are linked to the Wigner function by the Radon transformation [112]. Conversely the density matrix can be obtained from the Wigner function via a Fourier transformation. For pure states the marginal distributions are given by the states momentum and position distribution, e.g.

$$\int_{-\infty}^{\infty} W(x,p)\;dp = \left|\psi(x)\right|^2. \tag{2.36}$$

While positivity is a property that classical probability distributions over phase space have to obey strictly, non-classical quantum states force the Wigner distribution to take on negative values. For this reason, it is usually referred to as a quasi-probability distribution. Its negativity can thus be used to demonstrate that a quantum state has no classical analogon. This makes the Wigner function a useful tool for the characterization of quantum states and an interesting property to obtain experimentally.

Figure 2.9 depicts the Wigner functions for different classical and non-classical quantum states. For a coherent state $\left|\beta\right\rangle$, the Wigner function can be written as

$$W(\alpha) = \frac{2}{\pi}\exp\left(-2|\alpha-\beta|^2\right), \tag{2.37}$$

while the Wigner function of a Fock state $|n\rangle$ is given by

$$W(\alpha) = \frac{2}{\pi}(-1)^n L_n\left(4|\alpha|^2\right)\exp\left(-2|\alpha|^2\right), \tag{2.38}$$

where $L_n(\zeta)$ is the n-th Laguerre polynomial.

2.2.2 Homodyne detection

Homodyne detection and tomography have proven themselves to be valuable experimental tools in quantum optics [78, 113, 114]. The corresponding concepts

[5] In general any pair of conjugate variables, i.e. the real and imaginary parts of the electric field, will work as a phase space description.

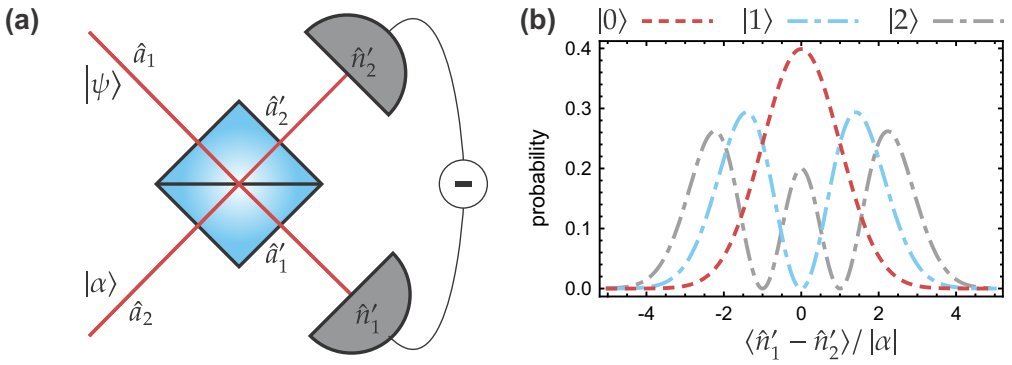

Figure 2.10: Sketch of the experimental realization of homodyne detection. a A balanced homodyning setup analyzes an unknown state $|\psi\rangle$ with the aid of a strong coherent state $|\alpha\rangle$. The states are mixed using a balanced beam splitter and the particle number difference at the output ports is recorded. **b** Normalized counting statistics vary greatly with the unknown input state. For the vacuum state $|\psi\rangle = |0\rangle$ a normal distribution is found (solid red line). If the input state is a Fock-state $|\psi\rangle = |n\rangle$ the probability distribution changes drastically as it is described by the Hermitian polynomials. Shown are the cases $|\psi\rangle = |1\rangle$ (dashed blue line) and $|\psi\rangle = |n\rangle$ (dash-dotted grey line).

have also been applied to ultracold atoms using the same quantum physical foundation by applying microwave or radio-frequency pulses that act as beam splitters. In a typical homodyne detection setup the quantum state of interest $|\psi\rangle$ is mixed with a strong coherent state $|\alpha\rangle$ on a symmetric beam splitter[6] (Fig. 2.10 a). This strong coherent state $|\alpha\rangle$ is named the local oscillator. The difference signal of the two particle numbers on the output ports is recorded for multiple realizations. Characteristics of the input state $|\psi\rangle$ can be inferred from the counting statistics of this signal (Fig. 2.10 b). For a given value of the phase θ of the local oscillator, the particle difference can be expressed using the corresponding particle number operators as

$$\hat{n}_1 - \hat{n}_2 = \frac{|\alpha|}{2} \hat{X}(\theta) \,. \tag{2.39}$$

Thus the particle number difference is proportional to the quadrature operator of the input state

$$\hat{X}(\theta) = \frac{1}{2} \left(\hat{a}_1 e^{-i\theta} + \hat{a}_1^\dagger e^{i\theta} \right) \tag{2.40}$$

where $\hat{a}_1$ and $\hat{a}_1^\dagger$ are the annihilation and creation operators of the input state, respectively. Amplification of the quadrature signal by the amplitude of the

[6] This type of homodyne detection is also referred to as balanced homodyne detection.

coherent state, which is the square root of the mean number of particles in the coherent state $|\alpha| = \sqrt{\langle n \rangle}$, can be deciding in scenarios with finite detection efficiency, detection noise or small quadrature signals.

The resulting counting statistics show distinguishable features depending on the input state $\left|\psi\right\rangle$. In Fig. 2.10 b, the probability of observing a certain particle number difference in the homodyne detection for the vacuum state $\left|\psi\right\rangle = |0\rangle$, the single-particle Fock state $\left|\psi\right\rangle = |1\rangle$ and the two-particle Fock state $\left|\psi\right\rangle = |2\rangle$ is shown.

2.2.3 Homodyne tomography

Instead of measuring only a single quadrature $\hat{X}(\theta)$ the phase θ of the local oscillator can be varied, effectively rotating the sampled quadrature For each phase value θ a probability distribution $P_\theta(x_\theta)$ can be recorded. This set of probability distributions characterizes the underlying quantum state and can be used to reconstruct the states' density matrix and the Wigner function, both equally providing a full characterization of the state itself. This has successfully been demonstrated for the photonic vacuum squeezed state by employing an inverse Radon transformation to link the probability distributions to the Wigner function [104, 112]. A more graphic way of understanding this is viewing the collected distributions as projections of the Wigner function. For example, the distribution $P_\theta(x_\theta)$ is given by integrating the Wigner function along the corresponding conjugate variable $x_{\theta+\pi/2} = p_\theta$, such that

$$P_\theta(x_\theta) = \int_{-\infty}^{\infty} W(x_\theta \cos\theta - p_\theta \sin\theta, x_\theta \sin\theta + p_\theta \cos\theta)\, dp_\theta. \tag{2.41}$$

In this manner, each different phase angle θ of the local oscillator provides information about the Wigner function along a certain direction, resulting in a tomographic representation. Besides the inverse Radon transformation, more recent reconstruction techniques are available. A more direct way to obtain the density matrix from the measured quadrature distribution, avoiding the detour via the Wigner function, uses so-called pattern functions and allows for a straightforward representation of the density matrix in the Fock basis [115–118]. Moreover, these advances also consider the impact of nonideal detectors with less than unit detection efficiencies η. Furthermore, a maximum likelihood reconstruction method omits even the calculation of marginal distributions and directly finds the most probable quantum state to produce the measured data [119–121].

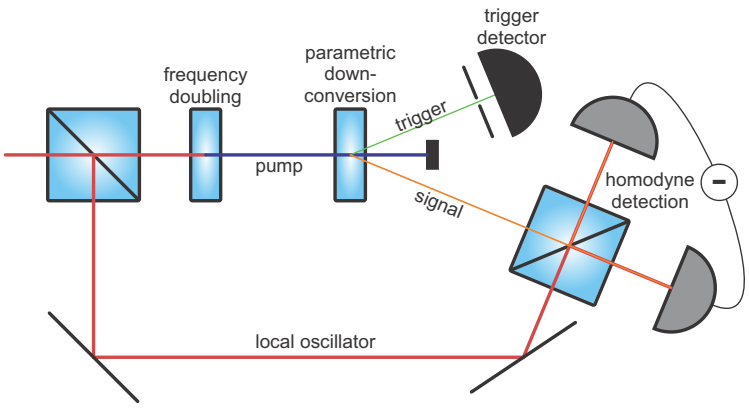

Figure 2.11: Sketch of the experimental apparatus to measure the photonic single Fock state Wigner function. Redrawing of the experimental setup used in [97]. The single photon state is generated by parametric down-conversion of a previously frequency-doubled pump beam. Spontaneous annihilation of a pump photon may produce a photon pair of lower energy separated into two emission channels. Detecting one of these photons in the trigger channel (green) causes a collapse of the photon pair and projects the quantum state in the signal channel (orange) into a single photon state. A major challenge of such a setup is the mode matching between the local oscillator and the signaling mode for the homodyne detection [122].

2.2.4 Experimental setup the for creation and the detection of Fock states

Reviewing the experimental details of the successful advances in the characterization of the single-photon [97, 101], two-photon [99] and three-photon Fock states [100] reveals a common scheme, that relies on the three key techniques discussed in the previous sections. Figure 2.11 shows a sketch of the experimental setup used to characterize the single-photon Fock state. The creation of photon pairs is achieved by consecutive frequency doubling and parametric down conversion of a pulsed laser source.

The detection scheme is two tiered. Firstly, a spatial filter defines a spatial mode in the trigger arm of the experiment that is detected by a single photon counting device (avalanche photo diode). A successful event detection heralds the creation of a desired Fock state in the signaling arm of the experiment. Secondly a strong coherent source is used to analyze the state in the signaling arm.

For the higher order Fock states $|2\rangle$ and $|3\rangle$ not only one single photon counter is used in the trigger arm, but an array of detectors corresponding to the size of the desired Fock state is needed [99, 100]. Only a simultaneous detection of the right

number of photons on all devices heralds the creation of the desired Fock state. The detection events project the quantum state of the photon pair(s) onto a Fock state within the signal arm that can be characterized by the homodyning setup. Spatial and spectral filtering in the heralding arm of the experiment ensures sufficient overlap with the local oscillator [122]. Especially when this scheme is extended to many particles, an efficient parallel detection becomes exponentially important. In atomic systems the parallel and accurate detection of many atoms with only one collective detection setup is experimentally feasible and will aid in the heralded creation of single- and many-particle states.

2.3 Entanglement and Bell tests

As one of the core features of quantum mechanics, entangled states are involved in thew wide range experiments fundamental test of quantum mechanics to applications in quantum metrology (Chapter 2.1.3). Even before the creation of pairwise entangled photons [123], the concept of entanglement, including its quantum mechanical description, has been a core topic among the physical community and gave rise to two of the world's most famous paradoxes. Still today, the test of quantum mechanics as a valid description of reality is an active research topic. This section reviews the idea of the EPR paradoxon and how it gave rise the a whole research field of Bell tests, before concluding with a proposed experiment that requires a single-particle detection to violate a Bell inequality.

2.3.1 The origin of entanglement: The Einstein-Podolsky-Rosen paradox

The peculiarity of the quantum mechanical concept of entanglement has inspired physicists to challenge their notion of reality ever since the famous publication by Einstein, Podolsky and Rosen that today is best known as the Einstein-Podolsky-Rosen (EPR) thought experiment [1]. In their pivotal work in which they brought the completeness of quantum mechanics into question they consider a pair of perfectly correlated quantum particles $\mathcal{A}$ and $\mathcal{B}$ (Fig. 2.12 a). These particles are emitted from a source in which their initial interaction causes them to pose equal but opposing momenta $p_{\mathcal{A}} = -p_{\mathcal{B}}$. Both particles will always occupy a position at the same relative distance with respect to the source - the only difference being the direction, such that $x_{\mathcal{A}} = -x_{\mathcal{B}}$ holds for their respective position. A measurement performed on the value of either position or momentum of one of the particles will allow to precisely predict the corresponding position or momentum of the respective other particle. This would imply, that even though neither position nor momentum have been measured on particle two,

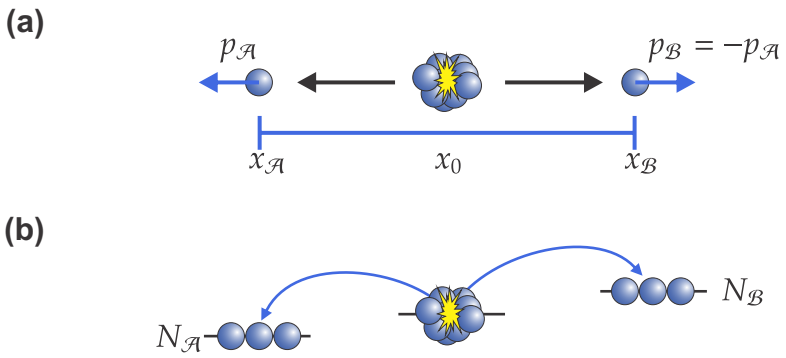

Figure 2.12: Sketch of the original Einstein-Podolsky-Rosen thought experiment and the principle of spin changing collisions in spinor Bose-Einstein condensate. a In the original version of their Gedankenexperiment [1] , Einstein, Podolsky and Rosen envisioned a physical system where two particles $\mathcal{A}$ and $\mathcal{B}$ poses perfectly correlated positions $x_{\mathcal{A}}$ and $x_{\mathcal{B}}$ and perfectly anti-correlated momenta $p_{\mathcal{A}}$ and $p_{\mathcal{A}}$. The paradox arises, when measuring both particles simultaneously allows to infer on the state of the respective other particle with arbitrary precision which stands in contradiction to the Heisenberg uncertainty relation. This contradiction challenged the notions of locality and reality in the context of quantum mechanical predictions. **b** Spin changing collisions in a ^{87}Rb spinor Bose-Einstein condensate create entangled particles in pairs in two different Zeeman levels that can be considered as spin-1/2 system. By tuning the microwave dressing necessary to start the dynamics an excited trapping mode can be targeted for the pair creation.

the corresponding quantity would be determined with precision. Since the measured quantity can be chosen at random after the particles parted ways, both outcomes must be predefined. This idea is referred to as realism and is in contradiction to the Heisenberg uncertainty principle which states, that the product of the uncertainties of two complementary observables such as position and momentum must of any quantum particle always fulfill [124]

$$\Delta p_j \Delta x_j \geq \frac{1}{2} \qquad \text{with } j \in \{\mathcal{A}, \mathcal{B}\}\,. \tag{2.42}$$

The only resolve for this conflict would be to allow, that a measurement on the state of one particle would influence the state of the other particle — even when the measurements were made in such rapid succession, that not even light could communicate any state change between the two particles. This explanation comes with its own complications, as it would seemingly allow for information to travel faster than the speed of light and violate the principles of locality.

Concluding that the theory of quantum mechanics is incomplete, EPR argued that a more precise theory including so-called hidden variables would solve the seeming paradox while still following the principles of locality and realism. Such hidden variables could carry the information about the outcome of the measurements disregarding whether the measurements actually take place.

The existence of hidden variables would make quantities like momentum and position "real"[7], allowing the theory to be guided by the principle of realism. This further would rule out the need for any kind of interaction that takes place at a speed faster than light, upholding the idea that actions are only conveyed locally or using an intermediate field thus maintaining the principle of locality. The combination of the two assumptions of locality and realism is often referred to as "local realism".

The ensuing discussion with their peers produced the ideas of entangled and seperable states, steering in EPR states, as well as the famous thought experiment nowadays known as Schrödinger's cat [2–4]. About 30 years after the initial formulation of the divide between quantum mechanics and local realism, Bell published inequalities that allowed to test quantum mechanics against the existence of hidden variables [125]. Bell based his theory on a simplified reformulation of the original EPR problem by Bohm and Aharonov that uses spin-1/2 particles [126]. Better suited to experimental realizations is the generalization of Bell's inequalities by Clauser, Horne, Shimony and Holt, known as CHSH inequalities [127]. An experimentally provided violation of Bell's or CHSH inequalities provides an indication towards the failure of local realism and rule out hidden-variable theories as a solution for the EPR paradox.

2.3.2 Experimental Bell tests

In the subsequent years and until the present day, many varying experimental attempts have been undertaken with the goal to test either of these inequalities, often referred to as Bell tests. The polarization correlations of photon pairs emitted by an radiative cascade of Ca atoms were investigated in the first reported violation and following experiments [128]. The use of non-linear laser excitations and two-channel polarizers improved the violation with respect to previous results and provided further support for the predictions of quantum mechanics [129–131]. Also Hg atoms were used as a source to produce correlated photon pairs in an atomic radiative cascade [132, 133]. By employing

[7] According to the wording of the original publication it would assign those quantities an "element of reality".

time-varying polarization analyzers that allowed to change the experimental settings during the flight of the particle an important locality loophole that allowed local theories to explain the violations was closed [134]. A short review on the photonic Bell test experiments up to the year 1998 may be found in a publication by Aspect [131].

Shortly afterwards a first atomic Bell test was carried out using a linear Paul trap loaded with two Be^+ ions [135]. Compared to their photonic counterparts the Bell tests performed on atomic systems have the advantage of detection efficiencies close to unity. While this is a solution to an argument within the detection loophole discussion, the locality loophole opened widely due to the small separation distances between subsystems that atomic experiments could provide initially. In ensuing work the separation distance grew from 3 μm [135], over a seperation of 1 m utilizing two Yb^+ ions in separated traps [136] to a distance of 20 m between two single ^{87}Rb atoms [137]. A more extensive elaboration on the history of photonic and atomic Bell tests as well as an even broader review on the whole concept of Bell nonlocality up to the year 2014 can be found in the publication by Brunner et al. [138].

Only in experimental results dating even more recently conclusive loophole-free Bell tests were demonstrated. Using the electron spins of two nitrogen vacancy centers separated by 1.3 km a Bell inequality violation was reported [139]. Reports for loophole-free experiments employing entangled photon pairs rejecting the hypothesis of local realism were published within the same year [140–142]. In a further experiment, detection and locality loopholes were closed in an atomic Bell test based on a heralded entanglement scheme of two ^{87}Rb atoms separated by 398 m [143]. Combining the effort of 12 institutions on five continents the BIG Bell Test collaboration (BBT) used the random input of 100000 human participants to choose the measurement settings of Bell tests conducted conclusively in 13 laboratories [144].

Striving to find the macroscopic boundary at which the strongest quantum correlation ceases, Bell tests have been performed using larger systems than just pairs of particles. A system consisting of 14 $^{40}Ca^+$ ions captured in a linear Paul trap has been reported to show multipartite Bell violations [52, 145]. Increasing the system size further to hundreds or even thousands of particles draws attention to ultracold atomic gases or even Bose-Einstein condensates which form physical systems that are particularly well suited to generate many-body entanglement. Especially the connection between global properties of the state and the fundamental correlations causing a violation of a Bell inequality can be studied. The top-down approach of ultracold atomic gases allows for entanglement generation of a few thousand particles [146]. Also EPR correlations have

been demonstrated in a Bose-Einstein condensate by violating the Heisenberg inequality for the inferred uncertainties of the conjugate variables certifying symmetric steering [108, 147, 148].

But the lack of identifiable subsystems with individual control, whereby the indistinguishability of the constituting particles is inherently linked to the entanglement generation [149], necessitated a new framework of inequalities. These inequalities were build upon first- and second-order correlation functions, opening tests of nonlocality to many-body systems, such as spin ensembles, by measuring collective spin components [150, 151]. Spin-squeezing a Bose-Einstein condensate of 480 ^{87}Rb atoms was reported to show a violation of a corresponding Bell witness by 3.8 standard deviations [152]. Thermal ensembles of 10^5 ^{87}Rb spin-squeezed atoms exhibited correlations that violated the same witness by 124 standard deviations [153]. Following a different approach, employing a compound system consisting of two silicon optomechanical oscillators made up of approximately 10^{10} atoms each and two optical modes, Bell violations by four standard deviations have been observed [154].

Reintroducing the question for addressability it has been demonstrated, that entanglement within a spinor Bose-Einstein condensate of ^{87}Rb persists between two spatially separated parts of an excited trapping mode of an optical dipole potential [155]. Similar results were obtained for spatial entanglement patterns in a Bose-Einstein condensate of ^{87}Rb including demonstrations of EPR steering in between the spatial regions [156]. Additionally, a similiar physical system provided evidence for spatially distributed multipartite entanglement in Bose-Einstein condensate and EPR steering [157].

2.3.3 Spatially separated Bell test with a Bose-Einstein condensate

In Fig. 2.13 the relation between different classes of entanglement or rather sets of entangled quantum states is depicted. While Bell violations are usually considered the strongest form of correlations caused by quantum entanglement, not all entangled (non-separable) states are suited for this task. The same argument holds for quantum states that exhibit EPR steering features. While the set of steerable states is subset of the entangled states, the set of non-local states is a subset of the steerable states [160]. Further aspects under which states can be classified is their metrological usefulness, best described by their quantum Fisher information content (Section 2.1.1), and their ability to provide spatially separated subsystems that exhibit the desired correlations.

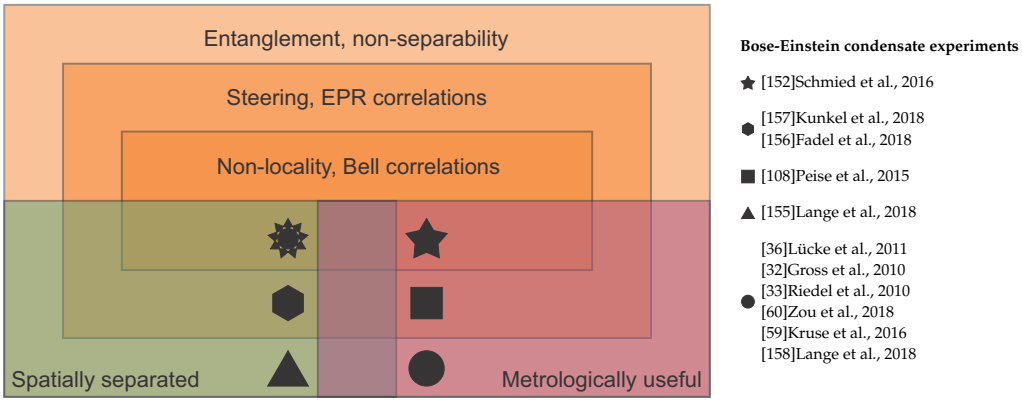

Figure 2.13 & Table 2.2: Classification of entangled states and corresponding experimental demonstrations using Bose-Einstein condensates. The class of entangled states or non-separable states encloses the largest amount of quantum states. Einstein-Podolsky-Rosen correlated states that allow for steering and violations of inferred Heisenberg uncertainty relations are a true subset of the entangled states. All states that demonstrate non-local behavior by violating a Bell inequality are again a true subset of the Einstein-Podolsky-Rosen correlated states. The Fisher information of states naturally imposes a different classification onto the set of all quantum states. Every state providing a quantum Fisher information $N^2 > F_Q > N$ is entangled and provides useful metrological properties, but this is not true for every entangled state. Showing all these properties across spatially separated subsystems is another distinctive classifying aspect. A Bell test with spatially separated parts of a Bose-Einstein condensate (✹) has not yet been performed. Reprinted from Ref. [159].

Hence the next advancement would be to perform a Bell test between spatially separated parts of a Bose-Einstein condensate and provide an answer to the question whether even strong Bell correlations can gap the spatial divide in the range of mesoscopic and macroscopic particle numbers. Taking the quantum state generated in Ref. [155] as a basis and pairing it with a single-atom resolving detection will be particularly fitting to answer this question.

A proposal by Yurke and Stoler suggests a Bell test using two independent single-particle sources [161]. The theoretical setup from the original publication is depicted in Fig. 2.14 a. It consists of two particles originating from independent sources (i.e. setting $N_\alpha = N_\beta = 1$) and entering an array of four balanced beam splitters on opposing sides before being detected in four detection channels. Even though the initial state is a pure product state as opposed to the original EPR idea this setup still allows to observe a Bell violation. The entanglement is generated by the respective first beam splitter (BS_{+1} and BS_{-1})

encountered by the particles on their path, entangling each particle with the vacuum mode entering the open port of the beam splitter. A second pair of beam splitters (BS_{L} and BS_{R}) mixes the four modes pairwise before the resulting four modes are detected with two pairs of particle counters. Correlations between the counts on the four output ports can be analyzed to retain violations of a Bell inequality. By refining the idea originally intended for pairs of single particles, Laloë and Mullin came up with a scheme that is even suitable to be used with higher order Fock states [162] and even three participating Fock states [163].

A possible adaption of the scheme towards the use of atomic twin-Fock states is also schematically drawn in Fig. 2.14 a. The state created by Lange et al. in Ref. [155] utilizes spin changing collisions in a ^{87}Rb Bose-Einstein condensate to populate the first excited mode of an external trapping potential with atoms in the $|F = 1, m_F = \pm 1\rangle$ states. This provides both inputs of the scheme with the same population number $N_\alpha = N_\beta$ resulting in the configuration that produces the maximum violation possible [162]. The mode structure of the excited trap mode itself acts as the first beam splitter pair (BS_{+1} and BS_{-1}) by splitting each magnetic sublevel population into two spatially distinct regions (L and R) divided by a line of zero density. A spatially selective phase shift can be applied by partially illuminating the cloud with a detuned light field after a free fall time that allows the Bose-Einstein condensate to expand. Microwaves can be applied in order to act as beam splitters BS_{L} and BS_{R} by coupling the $|F = 1, m_F = \pm 1\rangle$ states. A Stern-Gerlach pulse can finally spatially separate these states before the resulting four modes $N_{+1,\mathrm{L}}$, $N_{-1,\mathrm{L}}$, $N_{+1,\mathrm{R}}$ and $N_{-1,\mathrm{R}}$ need to be detected.

Fig. 2.14 b shows the expected violation of the Bell witness Q_{Bell} derived in [162] for different numbers of particles $N_\alpha = N_\beta = N/2$ at the input ports of the scheme, where any value $Q_{\mathrm{Bell}} > 2$ constitutes a violation. Solid lines depict the ideal case where all atoms are detected. In each case, a violation can be obtained, but the strength of the violation as well as the phase range $\Delta\varphi$ over which the violation extends decrease with increasing particle number (Fig. 2.14 c and Fig. 2.14 d). Thus initial attempts should focus on the use of Fock states with small atom numbers to make use of both, a larger violation and a more forgiving phase range. The dashed lines indicate the nonideal case where not all particles are detected. Since the Bell test is based on parity measurements already the loss of a single particle causes the violations to vanish, rendering a reliable detection that can resolve single atoms indispensable.

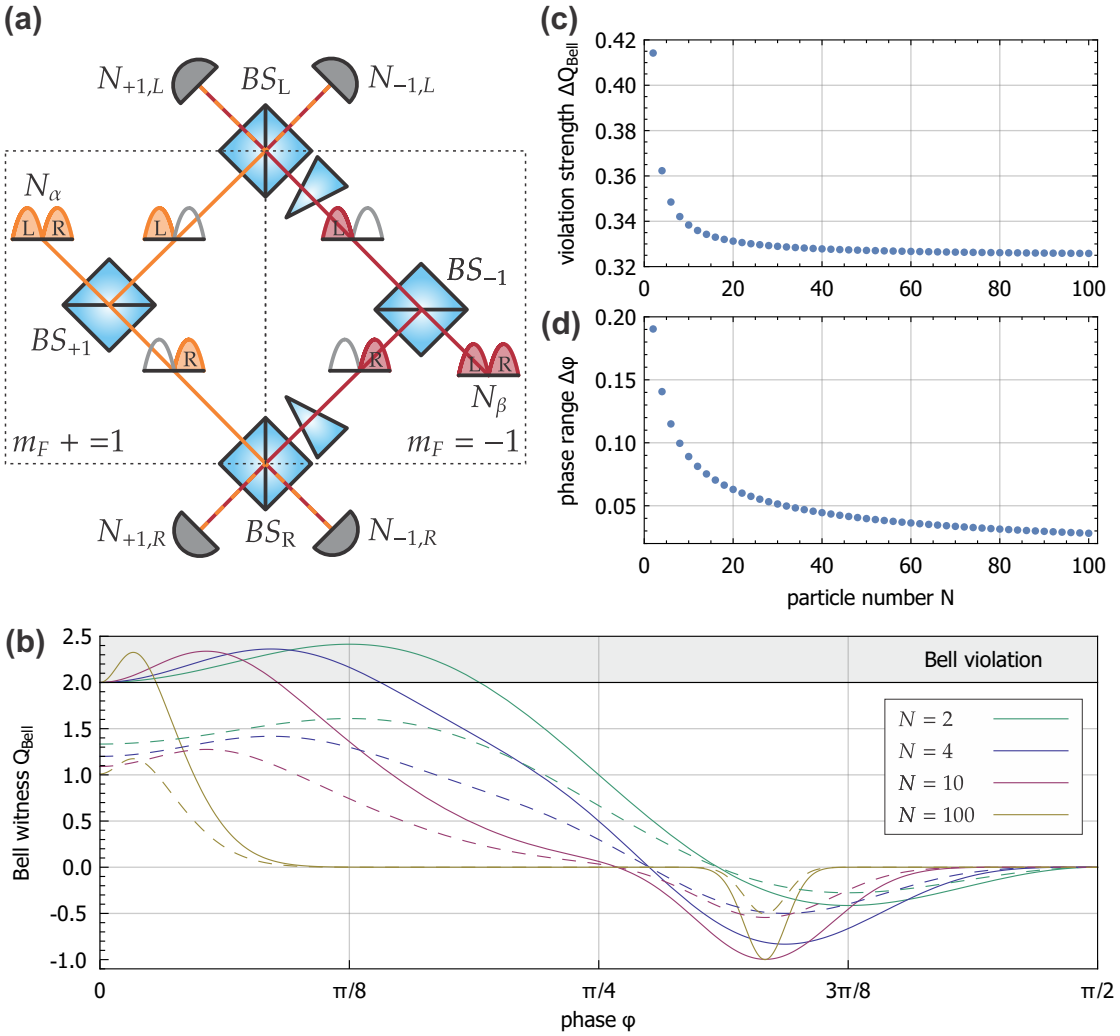

Figure 2.14: Bell test using two independent Fock states. **a** Sketch of the idea from Ref. [162] and translation to an atomic spinor system. Spin changing collisions create two Fock states with particle numbers $N/2$ in the $m_F = \pm 1$ manifolds (red and orange, respectively) of the first excited trap mode, readily incorporating the first beam splitting action of $BS_{\pm 1}$ by dividing each condensate fraction into a left (L) and right part (R). The second pair of beam splitters $BS_{L,R}$ can be implemented by means of microwave coupling between the $m_F = \pm 1$ states. **b** Bell violation witness Q_{Bell} as a function of the phase difference φ. A Bell violation occurs for values larger than $Q_{\text{crit}} = 2$. Colors indicate different absolute particle numbers N. Colored dashed lines show that detection losses for the corresponding initial particle numbers destroy the desired correlations. **c** Maximum violation strength of the witness Q_{Bell} for different particle numbers. Even for larger particle numbers a relatively strong violation of Bell inequalities can occur. **d** Range $\Delta\varphi$ over which a violation can be detected as a function of the total number N of particles used.

Chapter 3

Detecting single atoms in atomic quantum gases

The preceding chapter reported on the current state quantum metrology with atom interferometers, the creation and detection of non-classical quantum states and Bell tests with Bose-Einstein condensates. These research topics share the characteristic, that single-particle detection will play a crucial role in pushing the boundaries of the respective state-of-the-art experiments. This chapter briefly reviews currently available techniques for the detection of neutral atoms within ultra-cold atom experiments with respect to their capability of reliably detecting single atoms and accurately determining atom numbers. The concept of fluorescence detection in a magneto-optical trap will be discussed in more detail, as the detection system implemented within the scope of this work pursues this approach. The review follows a more exhaustive overview on this topic, covering the detection of single neutral atoms as well as ions, in Ref. [164].

3.1 Techniques

Since the term single-atom detection can be understood in a few different ways, a distinction has to be made between those detection approaches that offer single atom sensitivity and those that offer spatially resolved detection of single atoms[8]. The experiments proposed in Chapter 2 all rely on a detection scheme

[8]Single-atom detection could also be understood as a temporally resolved detection of many atoms. While this aspect is mainly important in the detection of ionized atoms with microchannel plates, this aspect will not be discussed within the scope of this thesis.

that can accurately determine atom numbers, but not necessarily resolve single atoms spatially. Hence the term *accurate atom counting* is chosen to refer to this type of detection. Alternatively, this kind of detection may be described as a *number resolving detection*. The act of determining the atom numbers of sub-ensembles depending on their internal state will be referred to as a *state-selective detection*. This task can be accomplished by sequencing or paralleling an accurate atom counting technique. Spatially resolving individual atoms in a quantum gas imposes the strongest requirements on the apparatus' spatial resolution capabilities, as it is typically performed in optical lattices that operate at inter-site distances of about 1 μm or less [165].

The challenge of accurately detecting atom numbers is twofold. Firstly, a single atom needs to be distinguished from the background or more precisely from the noise of the background. Secondly, the addition and removal of single atoms for large numbers of atoms needs to be discerned from the collective noise of all the other atoms. This second requirement makes it challenging to uphold the atom counting ability for larger ensembles.

3.1.1 Direct detection

By utilizing the energy stored in the metastable internal state of Helium atoms it is possible to directly detect neutral atoms that collide with a microchannel plate [166–168]. After being released from a trap and a time of flight, the atoms hit the microchannel plate that is located below the atom cloud. Upon impact, the internal state of the atoms is quenched and the excess energy ejects electrons from the surface, leading to a detectable signal. A big advantage of this detection scheme is, that in principle it offers two dimensional spatial resolution and temporal information, allowing for a reconstruction of the three-dimensional shape of the cloud. However, the detection efficiencies reached in this kind of setups of about 10 % [169] are far from unity and thus accurate particle counting cannot be achieved.

3.1.2 Ionization

Instead of detecting a neutral atom directly it can be ionized using two different experimental approaches: electron impact ionization and photoionization.

Electron impact ionization

Microchannel plates are also used to detect charged particles, such as atoms that were ionized by electron impact. Using a scanning electron beam with a diameter of only 500 nm a high resolution imaging of single atoms in a quantum gas was achieved [170–173]. In this case, the detection efficiency is limited by the ratio of electron collisions leading to an ionization of an atom and non-ionizing collisions of about $10 - 20\,\%$. This caveat renders electron impact ionization unfeasible for accurate atom detection.

Photoionization

A similar scanning method can be applied using the concept of photoionization based on single- or multiphoton absorption. On a chip, photoionization of ^{87}Rb atoms [174, 175] reaching single-atom detection efficiencies of 60 % [176] has been demonstrated. By means of three-photon ionization, a 67 % detection efficiency was achieved using a channel electron multiplier for single magnetically trapped ^{87}Rb atoms in a chip setup [177]. For larger atom numbers three-photon ionization was used to probe sub-Poissonian number statistics of atomic samples [178]. State-selective two-color photoionization detection for a single, optically trapped ^{87}Rb atom with with an efficiency as high as 98 % using a joined channel electron multiplier to capture the resulting ion and electron was reported [179]. Two-photon ionization was also achieved for ensembles of rubidium atoms in a magneto-optical trap and a Bose-Einstein condensate, where the detection efficiency for ions from the condesate reached 35 % [180].

3.1.3 Optical detection

The most common detection techniques in ultra cold atom experiments rely on the interaction of the atomic specimen with some kind of probe light field. This interaction can either result in a change of the polarization of passing light (Faraday rotation), the absorption of near-resonant illumination light or the emission of fluorescence light - all of which can be detected and in turn be used to refer back to the number of atoms within the atomic sample.

Absorption imaging

In absorption imaging, an atomic cloud, typically during free fall after being released from a trap, is being hit with a resonant laser beam for a few ten microseconds. By scattering light, the atoms reduce the laser beam's intensity that is recorded on a CCD camera. Comparing the shadow of the atoms with a reference image of just the illumination beam and an additional background image allows to deduce the optical density of the atomic sample and hence the

number of atoms in the column above each pixel. A final summation over the pixels yields the total atom number. Any photon scattered out of the probe beam contributes to the detected signal. The combination of the spatial resolution of the pixel detector and a preceding Stern-Gerlach pulse in form of a magnetic field gradient enables the simultaneous detection of multiple internal states or spin components (i.e. state-selective). Exactly this technique was used to obtain the results for the twin-Fock interferometer discussed in Chapter 2.1.3 and provided a counting uncertainty of 14 atoms for 10^4 atoms [34, 46]. Optimization for clouds of 300 atoms achieved a counting uncertainty of 3.7 limited by the strongest contribution of 3.6 atoms from photon shot noise [37]. By exposing a single ^{87}Rb atom in a far-off-resonant optical dipole trap (FORT) to a strongly focused weak gaussian beam for about $130 - 140$ ms, the scattering probability of a single neutral atom was measured, showing that in principle the detection of even a single particle is possible with an absorption detection scheme [181]. This technique is intrinsically limited by the photon shot noise of the bright illumination beam that enters twice into the signal.

Fluorescence imaging

In contrast to absorption imaging, fluorescence imaging relies on detecting light that is emitted by the atoms after they have been excited. The collection of the emitted fluorescence photons suffers from the fact, that the emission direction is chosen randomly and the signal is hence distributed isotropically across the full solid angle of 4π. Due to the limited optical access in typical ultracold quantum gas experiments, only a fraction of the available signal can be detected by an imaging system. A freely falling Bose-Einstein condensate of ^{87}Rb atoms passing a resonant light sheet consisting of two counter propagating laser beams has been used to demonstrate single-atome sensitivity [182–185]. Fluorescence emission occurs naturally from repeated excitation during laser cooling schemes. The combination of fluorescence imaging and cooling or trapping techniques enables prolonged interrogation times. In turn, the collected amount of photons is increased, scaling the signal-to-noise ratio favorably. Especially for spinor Bose-Einstein condensates, a typical experiment may end with the condensate being trapped in an optical dipole trap. Hence the combination of optical dipole traps and optical tweezers[9] has been investigated heavily and can be considered a group of *in situ* methods. Combinations of optical dipole traps with MOT beams [186] and polarization gradient cooling provided by a blue-detuned standing-wave probe beam resulted in the successful detection of individual atoms. The distinction of atom numbers up to three in terms of characteristic steps in the fluorescence signal was observed [187, 188]. Further

[9] An optical tweezer or microtrap refers to a very small optical dipole trap typically holding only individual to a few atoms.

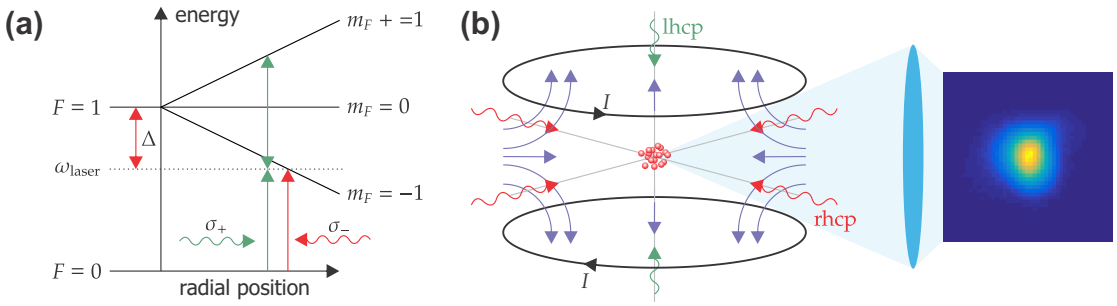

Figure 3.1: Principle of magneto-optical trapping. a Configuration for a MOT in 1D. Assuming simple hyperfine states F and Zeeman levels m_F split up by a linear magnetic field. The vertical axis depicts the internal energy of the atom, the horizontal axis the radial distance from the center of the trap. The dashed line illustrates the laser frequency ω_{laser} with a detuning Δ from $m_F = 0$. Due to the spatially dependent Zeeman splitting only atoms at certain position in space are resonant with the light field. The σ^- polarization of the beam allows only the incoming beams to excite the atoms. **b** Configuration for a MOT in 3D. Two coils in anti-Helmholtz configuration create a magnetic quadrupole field. Six laser beams with polarizations depending on the direction the magnetic field need to be polarized accordingly as left-handed or right-handed circular (lhcp and rhcp) for them to be recognized as σ^- light when approaching the center of the trap. The atoms in the trap run through many absorption and emission cycles during the cooling process. Using a lens with large numerical aperture the fluorescence signal can be collected and used to derive the number of atoms residing in the trap.

improvements of this method relied on sophisticated modeling and characterization of the dominant loss mechanisms, i.e. light assisted two-body collisions [189, 190]. This led to a phenomenon called collisional blockade [186, 191] and a prolonged imaging sequence but could not extend the unambiguous signature of single atoms to significantly larger samples [192]. Similar limitations apply to attempts of imaging neutral atoms in optical lattices.

3.2 Fluorescence detection in a magneto-optical trap

Magneto-optical traps (MOTs) are at the heart of almost every experiment that deals with ultracold neutral atoms and the working principle can be found in many textbooks [193–195]. Figure 3.1 briefly sums up the working principle of a MOT. A spatially varying magnetic field splits the Zeeman sublevels. At the origin the direction of the magnetic field reveres together with the quantization axis of the atoms. An appropriately polarized σ^- red detuned light beam approaches

the origin will at some point along the way become resonant with the atoms. This of course is reflected in a high scattering rate. Due to the random isotropic direction of the emission a net force pushes the atoms towards the origin. Once the light has passed the origin the atoms experience the opposite polarization of the light, as their quantization axis has turned. By applying a counterpropagating beam of equal intensity and detuning the same argument can be made for the opposing direction. The extension of this principle to three dimensions and six beams is the basic idea of the MOT. Usually their large capture velocity is used to load atoms from a background gas into an atomic cloud that serves as the starting point of the experiment. But due to the long life time, that can reach hundreds of seconds, and the large amount of fluorescence photons send out by them atoms they are a natural candidate for fluorescence detection – especially on the single to few atom level [38–42]. Even mesoscopic atom numbers of up 1200 atoms were detected by fluorescence imaging of a MOT [43] and up to 500 in a MOT split by a blue detuned light sheet [44]. One of the most important parameters in the MOT detection is the scattering rate

$$R_{\mathrm{sc}} = \frac{\Gamma}{2} \frac{s_0}{1 + s_0 + 4\left(\Delta/\Gamma\right)^2}, \tag{3.1}$$

where $s_0 = I/I_{\mathrm{sat}}$ is the saturation parameter given by the ratio of light intensity I and saturation intensity I_{sat}, Γ the natural linewidth of the transition and Δ the detuning of the light field with respect to the transition frequency. Two processes inherently limit the measurement precision of N_{ats} atoms even for perfectly known and stable parameters of the trap. Firstly, photon shot noise will contribute to the variance $\sigma^2_{N_{\mathrm{ats}}}$ with a term $\sigma^2_{psn} = N_{\mathrm{ats}}/n_{\mathrm{ph}}$, where $n_{\mathrm{ph}} = \eta R_{\mathrm{sc}} \tau_{\mathrm{exp}}$ is the number of photons detected per atom during the exposure time τ_{exp}. The detection efficiency of the detector is reflected by the parameter η. Secondly, the contribution of atom loss to the variance is described by $\sigma^2_{\mathrm{loss}} = N_{\mathrm{ats}} \tau_{\mathrm{exp}}/\tau_{\mathrm{life}}$, where τ_{life} is the life time of a single atom in the trap. This simple noise model reads

$$\sigma^2_{N_{\mathrm{ats}}} = \frac{N_{\mathrm{ats}}}{(\eta R_{\mathrm{sc}} \tau_{\mathrm{exp}})} + \frac{N_{\mathrm{ats}} \tau_{\mathrm{exp}}}{\tau_{\mathrm{life}}} \tag{3.2}$$

and can be used to derive an optimal detection time $\tau_{\mathrm{exp,opt}} = \sqrt{2\tau_{\mathrm{life}}/(\eta R_{\mathrm{sc}})}$ and single-particle resolution threshold of $N_{\mathrm{ats,max}} = \sqrt{\eta R_{\mathrm{sc}} \tau_{\mathrm{life}}/2}$ by setting $\sigma^2_{N_{\mathrm{ats}}} = 1$.

For typical fluorescence detection setups, the excitation light can be brought in from a direction perpendicular to the imaging axis. This minimizes the chances of scattering unwanted stray light from the excitation beam into the detection. [10] This is different for fluorescence detection schemes that utilize a MOT. Here the

[10] Because illumination light and fluorescence light in this case share the same frequency the signal cannot be separated from the background by an optical filter.

direction of the six beams is dictated by the magnetic gradient field, offering way more potential to scatter light into the detection lens. Additionally, to optimize the amount of light captured by the detection, the detection lens has to be big and as close to the MOT as possible. Hence, great attention must be paid to estimating any cooling light that could be scattered into the detection. If the detected background is so large that the fluorescence signal of single atoms is smaller than the background noise, no accurate atom counting detection will be possible.

In conclusion the fluorescence detection in MOT faces three main challenges that can be overcome by technical means. The photon shot noise influence can be reduced by collecting more of light and by detecting it more efficiently. From the experimental side this can be approached using a detection lens with a large numerical aperture, choosing a camera with high quantum efficiency and taking care of any possible losses due to reflections on optics surfaces. The life time of atoms in the MOT can be optimized by low background pressure and good vacuum conditions. Additionally, well balanced cooling beams, as well as stable powers and frequencies help with increasing the life time. Background light impact can be managed by careful design of the optical path by considering probable scatter centers in advance. Blocking off any direct reflections into the detection system and reduction of stray light inside the detection system by spatial filtering are applicable strategies. With these technical solutions at hand fluorescence imaging in a MOT is the best candidate for an application as an accurate atom detection.

Chapter 4

Experimental apparatus

The following chapter outlines the details of the experimental apparatus, that has been designed and set up during the work of this thesis. The demands on a modern quantum optics experiments are diverse, at times even irreconcilable. A careful assessment of all involved aspects has to be made in order to be able to fulfill the various requirements of the ambitious goals of the quantum-enhanced atom interferometer and pose the right respective requirements on the various subsystems of the setup. These goals and requirements were in part derived in the previous chapters and are summarized in the first section of this chapter and put into context of the experimental concept. The ensuing section lays out the vacuum system with its various components. The third and fourth sections deal with the components creating the light fields and magnetic fields of the setup, that steer the desired interactions with the atoms and will allow for capture and manipulation. Finally, the fifth section delineates the detection system, the details of which are decisive for one of the central design goals: achieving accurate atom counting.

4.1 Experimental procedure

The design goals for the experimental apparatus are aimed at the ability to perform high-precision atom interferometry using many-particle entangled states of ^{87}Rb atoms created by spin changing collisions. They can best be understood in context of a schematic experimental sequence (Fig. 4.1). A very coarse yet helpful classification allows to distinguish between three main parts of the sequence: Preparation, experiment and detection. The following three subsections describe the planned experimental procedure, before the ensuing sections cover the already implemented hardware.

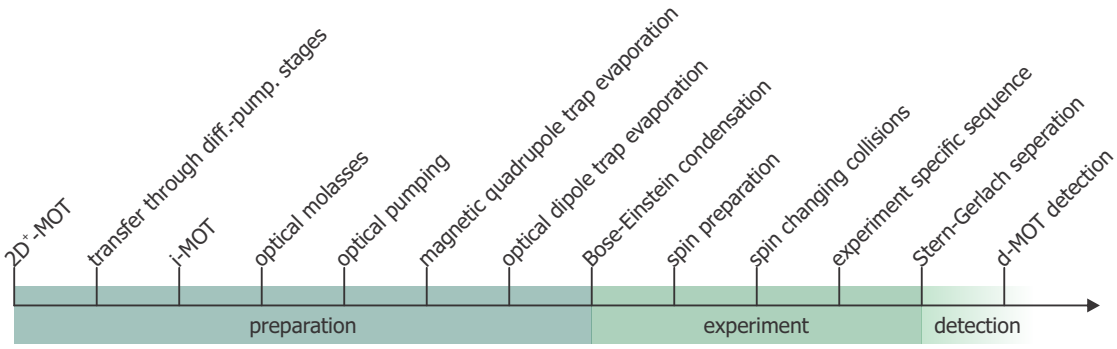

Figure 4.1: Experimental concept. A $2D^+$-MOT is employed to load ^{87}Rb atoms from the background gas and feed them through two differential pumping stages into a initial 3D-MOT (i-MOT) that is operated in the octagonal science glass cell. The sequential application of an optical molasses, optical pumping into a magnetically sensitive sub-state, a magnetic quadrupole trap and an evaporation process in a strong dipole trap will eventually cool the atomic sample until it reaches Bose-Einstein condensation. This will conclude the preparation process that will be followed by entanglement generation through spin-changing collisions and a specific experimental sequence, for instance a twin-Fock interferometer scheme. A Stern-Gerlach pulse can be used to spatially separate the spin components. Fluorescence detection in a special magneto-optical trapping configuration (d-MOT) will allow to accurately detect atom numbers as a result of the experiment.

4.1.1 Preparation

The generation of large ultracold atomic samples at high repetition rates is mandatory for a state-of-the-art atom interferometer. Fast sample generation allows for short averaging times featuring an increased temporal resolution and decreased sensitivity to long-term drifts. The repetition speed of a BEC apparatus depends on a large group of its components, yet two main steps in preparing a Bose-Einstein condensed spinor sample are typically very time consuming. On the one hand, the initial loading of atoms from a background gas into a three-dimensional magneto-optical trap can take several seconds. On the other hand, the evaporation process in a magnetic trap or optical dipole trap is inherently slowing down for shallow trapping confinement. Both challenges will be taken on by the newly build apparatus.

The loading of the initial three-dimensional magneto-optical trap (i-MOT), be-

ing the first step in the sequence, is performed by means of an atomic beam originating from a two-dimensional magneto-optical trap setup with a pusher beam (2D$^+$-MOT). Cooling light for this process is driving the $|5^2S_{1/2}, F = 2\rangle \rightarrow |5^2P_{3/2}, F' = 3\rangle$[11] transition o ^{87}Rb, while additional repump light on the $|F = 1\rangle \rightarrow |F' = 2\rangle$ transition returns atoms that decayed into the ground state to the cooling cycle. This concept already demonstrated a very high atomic flux of 8×10^{10} $\frac{\text{atoms}}{\text{s}}$ used to load a three-dimensional magneto-optical trap with 8×10^9 $\frac{\text{atoms}}{\text{s}}$ within 200 ms [196] in a former setup. First tests on the presented apparatus showed a loading rate of $9.5(1) \times 10^9$ atoms/s and about $3.3(1) \times 10^9$ atoms in the i-MOT after 400 ms (Fig. 4.2). These preliminary values will be subject to optimization of 2D$^+$-MOT cooling light detuning, power and exact gradient fields to best match the double differential pumping geometry, once larger amounts of atoms are needed for evaporative cooling.

Subsequently, an optical molasses phase [195, 197] is planned to cool the atomic cloud further. The i-MOT cooling light already is in the desired configuration of six pairwise counter-propagating beams of opposite polarization. Further, the magnetic fields of the i-MOT will be turned off. Ambient magnetic fields will be canceled by the dedicated compensation coils . Lastly, by increasing the frequency detuning this sub-doppler-cooling technique will be realized.

Afterwards, optical pumping using σ^+-polarized light on the $|F = 2\rangle \rightarrow |F' = 2\rangle$ transition transfers the atoms into the $|F = 2, m_F = 2\rangle$ state. The quantization axis will be defined by the magnetic field created by the homogenous field coils. The magnetic quadrupole trap, that is generated by the magnetic gradient fields of the quadrupole coils, will capture the atoms. After ramping the gradient to 300 G/cm, a brief radio-frequency evaporation will cool the sample down [198]. Further evaporation will be performed in a crossed-beam optical dipole trap [199, 200]. The process will be sped up by employing a high-power 55 W laser beam with a wavelength of 1064 nm (Coherent Mephisto MOPA 55W) to form a strong crossed-beam optical dipole trapping potential. The implementation of acousto-optical deflectors will allow to change the optical trapping potential rapidly [201, 202]. When the gradient field of the quadrupole coils is being ramped down, homogeneous field coils will be used to maintain a controlled quantization axis for the atomic sample. Reaching Bose-Einstein condensation concludes the first major step in the procedure, the preparation. Good vacuum conditions in the science glass cell, where the Bose-Einstein condensate will be situated, will reduce the probability of background collisions. While this is directly beneficial towards the ensemble life times in all trapping geometries, it also aids in preparing and controlling sensitive multi-particle entangled states

[11] In further notation the fine structure levels will not be mentioned explicitly. Instead the hyperfine levels are noted as F and F', referring to $5^2S_{1/2}$ and $5^2P_{3/2}$, respectively.

as it reduces the chances of collisions causing dephasing.

4.1.2 Experiment

In order to drive spin-changing collisions in a ^{87}Rb spinor Bose-Einstein condensate, precise spin-preparation is crucial.[12] After transfer from the magnetic trap, the atoms reside in the state $|F = 2, m_F = 2\rangle$ in the optical trap with the homogeneous field coils dictating the quantization axis. By a sequence of microwave π-pulses between $|F = 2\rangle$ and $|F = 1\rangle$ manifolds, the atomic population is transferred to the $|F = 1, m_F = 0\rangle$ state. Interleaved resonant light pulses on the $|F = 2\rangle \rightarrow |F' = 3\rangle$ transition clean up any residual populations in the $|F = 2\rangle$ manifold. Using microwave dressing [107, 203–205] between the internal Zeeman levels $|F = 1, m_F = -1\rangle$ and $|F = 2, m_F = -2\rangle$, the state $|F = 1, m_F = -1\rangle$ is shifted such, that the asymmetric splitting of $|F = 1, m_F = -1\rangle$ and $|F = 1, m_F = 1\rangle$ due to the quadratic Zeeman shift is canceled. This equalizes the energetic splitting of $|F = 1, m_F = -1\rangle$ and $|F = 1, m_F = 1\rangle$ and with respect to $|F = 1, m_F = 0\rangle$ and allows spin-changing collisions to take place. Generating entanglement between the atoms by means of these collisions is the starting point for all experiments proposed in Chapter 2.

4.1.3 Detection

The introductory Chapter 2 describes multiple atom optics experiments that rely on detecting an accurate atom number. The concept of twin-Fock interferometry is one way to realize a quantum-enhanced interferometer in an atom optics experiment and as such relies on the apparatus' capability to reliably detect accurate atom numbers in the interferometer states. As discussed in Chapter 3, a detection scheme is chosen where the atoms are loaded into a dedicated three-dimensional magneto-optical trapping configuration, referred to as a detection MOT (d-MOT) where their fluorescence signal is recorded. For this type of detection, a stable laser power in the involved cooling laser beams is crucial, making an active power stabilization for them a necessity. Demonstrating the accurate atom counting capability of the apparatus is the first major milestone in the construction process (Chapter 5).

Running a full interferometric sequence will require the accurate detection of

[12] An in-depth description of the spin-preparation process and spin-changing collisions can be found in Ref. [46].

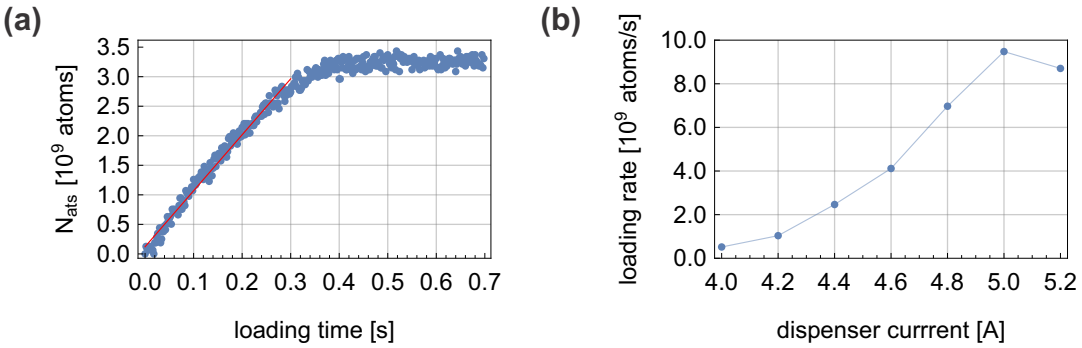

Figure 4.2: Performance of the 2D$^+$-MOT and i-MOTà The number of atoms in the i-MOT as a function of time for a dispenser current of 5 A. The initial linear loading rate is estimated over the first 300 ms and results in 9.5(1) $\times$ 10^9 atoms/s. After 400 ms the saturation of 3.3(1) $\times$ 10^9 atoms is reached.**b** The extracted loading rate as a function of the dispenser current.

multiple output modes rather than just one. A state-selective detection will be needed, to take full advantage of the twin-Fock approach. Using only one detection setup, the selective detection either has to be realized by separating the output states spatially or temporally, i.e. detecting them in sequence. Our approach so far focuses on a spatially separated detection, that builds upon the Stern-Gerlach effect. This makes use of the fact, that the desired outcome of the experiment is measured in terms of the atom numbers in different spin states. Thus employing a magnetic field gradient to separate these states is a natural choice, before recapturing the atoms in the d-MOT. The state-selective detection then can be realized by deploying a blue-detuned light sheet to the center of the d-MOT, which was shown to be able to resolve the atom number difference of two spatially separated clouds for up to 500 atoms accurately [44]. Acting as a repulsive potential barrier, the light sheet allows for a spatial separation of individual modes on the scale of a few micrometers, making a simultaneous detection of the modes feasible without posing strong requirements on the spatial resolution capabilities of the imaging system.

4.2 Vacuum system

In order to perform experiments on samples of ultracold atoms, the vacuum system (Fig. 4.3) has to match a certain set of requirements. A high background pressure of rubidium atoms in the 2D$^+$-MOT glass cell is desirable to quickly and efficiently generate a strong beam of pre-cooled atoms that is sent towards the

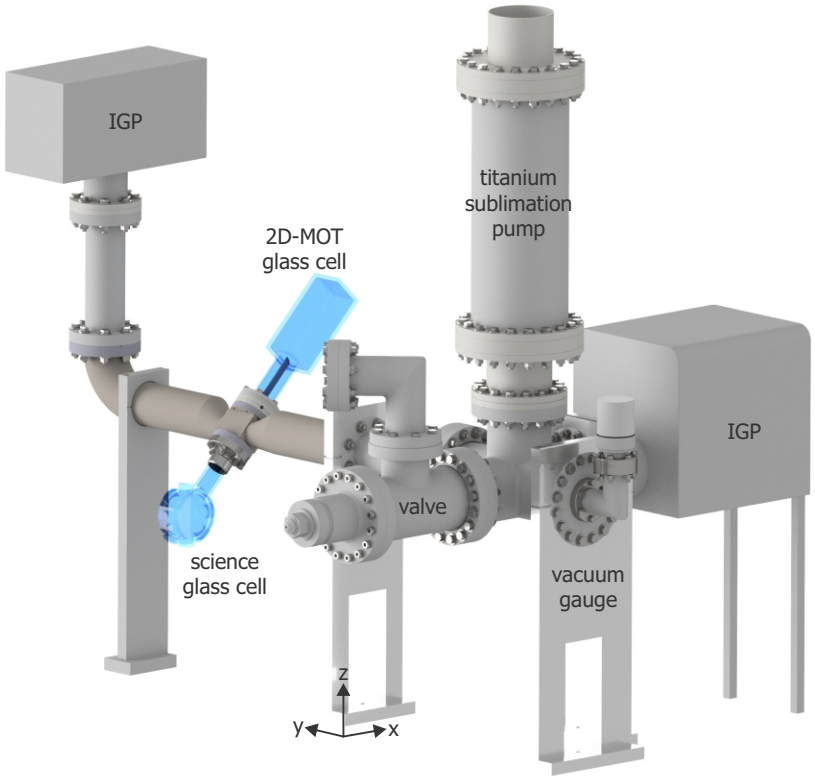

Figure 4.3: Vacuum system overview. This drawing shows all components of the UHV vacuum system. The main components for the experimental operation are the two glass cells (2D$^+$-MOT cell and science cell) at the center. Peripherals are the two differential pumping stages in between the two glass cells, the two ion getter pumps (IGP), the titanium sublimation pump, the valve and the vacuum gauge. All parts are connected using ConFlat (CF) flanges sealed with copper gaskets. The shown coordinate system is used in the description of the apparatus.

3D-MOT [206]. The glass cell for the 2D$^+$-MOT is made out of quartz glass that is anti-reflection coated for a wavelength of 780 nm, allowing the cooling and repumping light needed to drive the 2D$^+$-MOT to be used most effectively. The high background pressure is realized by heating up one of three dispensers that hold a rubidium salt, that during an electric heating process is reduced chemically. The exit slit that allows the rubidium to leave the dispenser is aimed at the trapping region of the 2D$^+$-MOT to avoid condensation on the glass surfaces of the cell.

The 3D-MOT is situated in the science chamber, where all further experimental steps with the atoms are conducted. Thus, this region has to conform a much

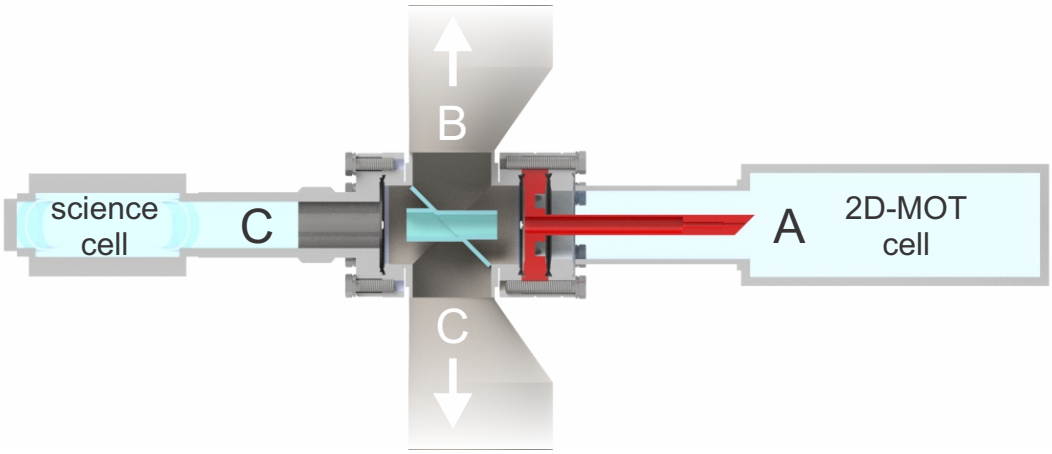

Figure 4.4: Differential pumping stages. This cut through the 2D$^+$-MOT glass cell, the custom four-way cross and the science glass cell shows the separation into three different vacuum ares by the use of two consecutive differential pumping stages (highlighted in red and cyan). Area A only consists of the 2D$^+$-MOT glass cell with a high ^{87}Rb background pressure. It is connected to area B by the first differential pumping stage (red). A first IGP is used to pump area B. The second differential pumping stage (cyan) connects to the science glass cell. Area C is also directly connected (white arrow) to a second IGP, to the Titanium sublimation pump, the valve and the vacuum gauge for maintaining and monitoring the vacuum conditions.

different standard for the background pressure, that usually is referred to as ultrahigh vacuum (UHV) and features a background pressure of $< 10^{-11}$ mbar. These two different requirements for the background pressure between 2D$^+$-MOT and 3D-MOT are in conflict, because the atomic beam requires a direct line of sight between the 2D$^+$-MOT and 3D-MOT regions. The implementation of a succession of two differential pumping stages (Fig. 4.4) resolves this issue elegantly, by internally dividing the vacuum system into three regions of different pressure: the 2D$^+$-MOT region, a pumping region of intermediate pressure and the science or 3D-MOT region that allows for the lowest possible pressure.

The first differential pumping stage is placed such that it separates the 2D$^+$-MOT glass cell from the remainder of the system, shielding it from the comparably high pressure in the 2D$^+$-MOT glass cell. This pumping stage measures 100 mm in length, has an entrance diameter of 2 mm that widens over a distance of 25 mm to an inner diameter of 8 mm. The entrance cap of the differential pumping stage is polished and cut at an 45 ° angle to act as a redirecting mirror for the pushing and retarding light beams. The vacuum area neighboring the 2D$^+$-MOT region is being pumped by an ion getter pump (VacIon Plus 150 Star

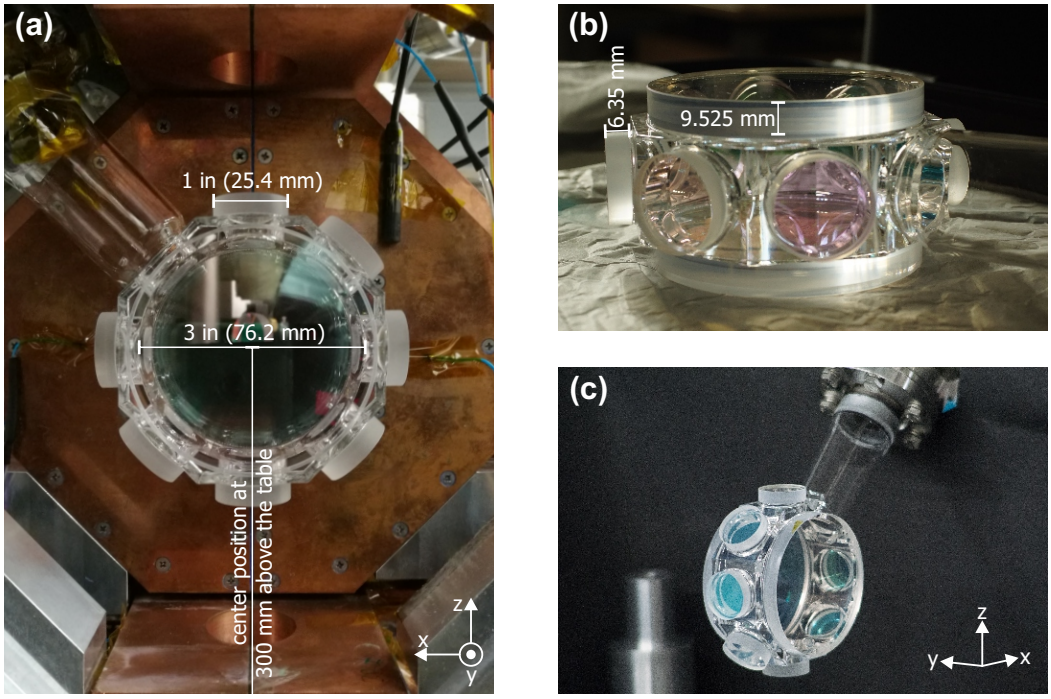

Figure 4.5: Photographs of the science glass cell. The images show the science glass cell from the side in its final mounting position (**a**) and from the side before the installation (**b**). The combination of two large 3 inch side windows and seven smaller 1 inch windows along the perimeter of the octagonal frame allows for maximal optical access to the atomic sample. The bigger side windows enable high numerical aperture (NA) imaging specifically.

Cell Model 919 - 0104) and serves the purpose of shielding the science region from unwanted background gas. Following the first differential pumping is a custom designed four-way vacuum connection, that connects the pumps and the glass cells. Along the diagonal of the four-way crossing, an additional wall further separates the science region from the intermediate region. The second differential pumping stage built into this wall allows the atoms from the $2D^+$-MOT glass cell to travel towards the science region. Via the custom four-way cross science region is also connected to an additional ion getter pump (Varian Large Star cell Model 929 - 0172), a titanium sublimation pump, a vacuum gauge (Balzers IKR 250 Compact Cold Cathode Gauge), as well as a vacuum valve to connect turbo pumps for initial evacuation of the vacuum system.

The glass cell housing of the 3D-MOT and science region is a custom made quartz class cell (modified from the 3 Inch Octagonal MOT/BEC Glass Cell line by Precision Glass Blowing in Denver, CO) that is designed to maximize optical access to the atomic probe at its center (Fig. 4.5). Since the science glass cell

houses the atoms during all stages of the experimental sequence, i.e. 3D-MOT, magnetic and consecutive optical trapping and detection, a large optical access is beneficial and even mandatory for the detection scheme we apply. Future potential extensions of the experiment using optical lattices or painted potentials will also greatly benefit from a design that gives multiple optical access points. It features two large opposing main windows with an outside diameter of 3 in (76.2 mm) of which 2.75 in (69.85 mm) can be used to gain optical access to the sample. The main windows are 0.375 in (9.525 mm) thick and placed at an inner distance of 1.21 in (30.734 mm). This thickness needs to be taken into account when considering aiming any directed light source at the atoms, as it will noticeably displace an optical beam. An anti-reflection coating from both inside and outside ensures that the optical beams for all MOT configurations at a wavelength of 780 nm can pass with maximum transmissivity at an angle of incidence of 45 °. The coating is additionally optimized for a wavelength of 1064 nm, facilitating the use of a high power laser for the generation of an optical dipole potential. The circumference of the glass cell is of octagonal shape and allows optical access through seven 1 in (25.4 mm) windows. These smaller windows are anti-reflection coated for 780 nm and 1064 nm at an orthogonal angle of incidence on the inside and outside. The eighth outside edge is featuring the vacuum connection that links the science glass cell to the rest of the vacuum setup using a CF40 flange.

The orientation of the $2D^+$-MOT and science glass cell at an angle of 45 ° relative to the optical table is connected to the orientation of the detection system and the science glass cell. Since the detection system features large optical elements as well as robust and heavy constructions to hold these optics, mounting it along an horizontal axes, rather than a vertical one, allows for safer, easier repeated handling and adjustments of the devices. Hence the orientation of the science glass cell with the big windows facing sideways is fixed by this principle. The $2D^+$-MOT can be considered a well understood component of the system that has been tested in a previous experimental apparatus and has been proven to be very robust. Thus the decision was made to put the well tested parts of the apparatus into the 45 ° inclined orientation, while the more delicate and more often changed and altered parts would be placed at the positions that are more convenient to access. Additionally, this frees up another horizontal axes through the science chamber for the optical dipole trap.

4.3 Laser system

For the operation of the experiment, multiple laser sources are needed in order to interact with the atomic samples (Fig. 4.6). Exploiting these interactions atoms

can be cooled, trapped, detected and have their internal state specifically manipulated. Thus during different stages of the experiment, different laser systems are used to generate the needed wavelengths, polarizations and powers. This section focuses mainly on the laser sources needed to run the magneto-optical trapping configurations for ^{87}Rb, as they are important for both preparation and detection stage. Since dipole trap optics are being set up during the writing of this thesis and might still be subject to change, they will only be outlined briefly. The optical setup is spread across a dedicated "optics table" holding the cooling and repumping laser systems and the "vacuum table"[13]. On the laser table the needed frequencies and the needed amount of optical power are being generated and delivered to the table with the vacuum setup with the help of optical fibers. On the vacuum table beam shaping, polarization preparation and power distribution is being performed.

Optics table

All frequencies used in the magneto-optical traps are located in the vicinity of the ^{87}Rb D_2 line at 780.241 nm [207]. The light at these wavelengths is supplied by two diode laser sources. The natural linewidth of $\Gamma_{\mathrm{Rb}} = 2\pi \times 6.065(9)$ MHz sets the fundamental requirements for the laser sources and their locking scheme. The first laser uses a Doppler-free saturation spectroscopy setup for frequency stabilization. Choosing the $F = 2 \rightarrow F' = 1/3$ crossover transition in combination with a 200 MHz modulation AOM enables access to all transitions starting at $F = 2$ within the D_2 line by simply employing another 200 MHz AOM within the respective beam path. Thus the first laser can act as a source for deriving light fields driving the $F = 2 \rightarrow F' = 3$ cooling transitions in the 2D$^+$-MOT the two 3D-MOT configurations i-MOT and d-MOT, as well as find its use for a potential absorption detection setup. In accordance with its main application the first laser is referred to as the cooling laser. Also frequencies driving transitions originating at the $F = 1$ level are needed for providing a repumping mechanism in all MOT configurations. Due to the large gap of 6.8 GHz between the $F = 1$ and $F = 2$ levels, it is not possible to use the first laser to generate the appropriate frequencies. Thus, a second laser, referred to as the repump laser, is used and stabilized with respect to the cooling laser by means of a microwave interferometer Here, an adjustable delay stage is used to allow setting of the relative locking point. This light source generates the repumping light on the $F = 1 \rightarrow F' = 2$ transition.

Since the laser diodes only provide output powers in the range of a few 10 mW, but especially 2D$^+$-MOT and i-MOT performance scales favorably with the pro-

[13] The quick-witted reader now may deduce that this table does contain nothing at all, but in fact it supports the vacuum chamber.

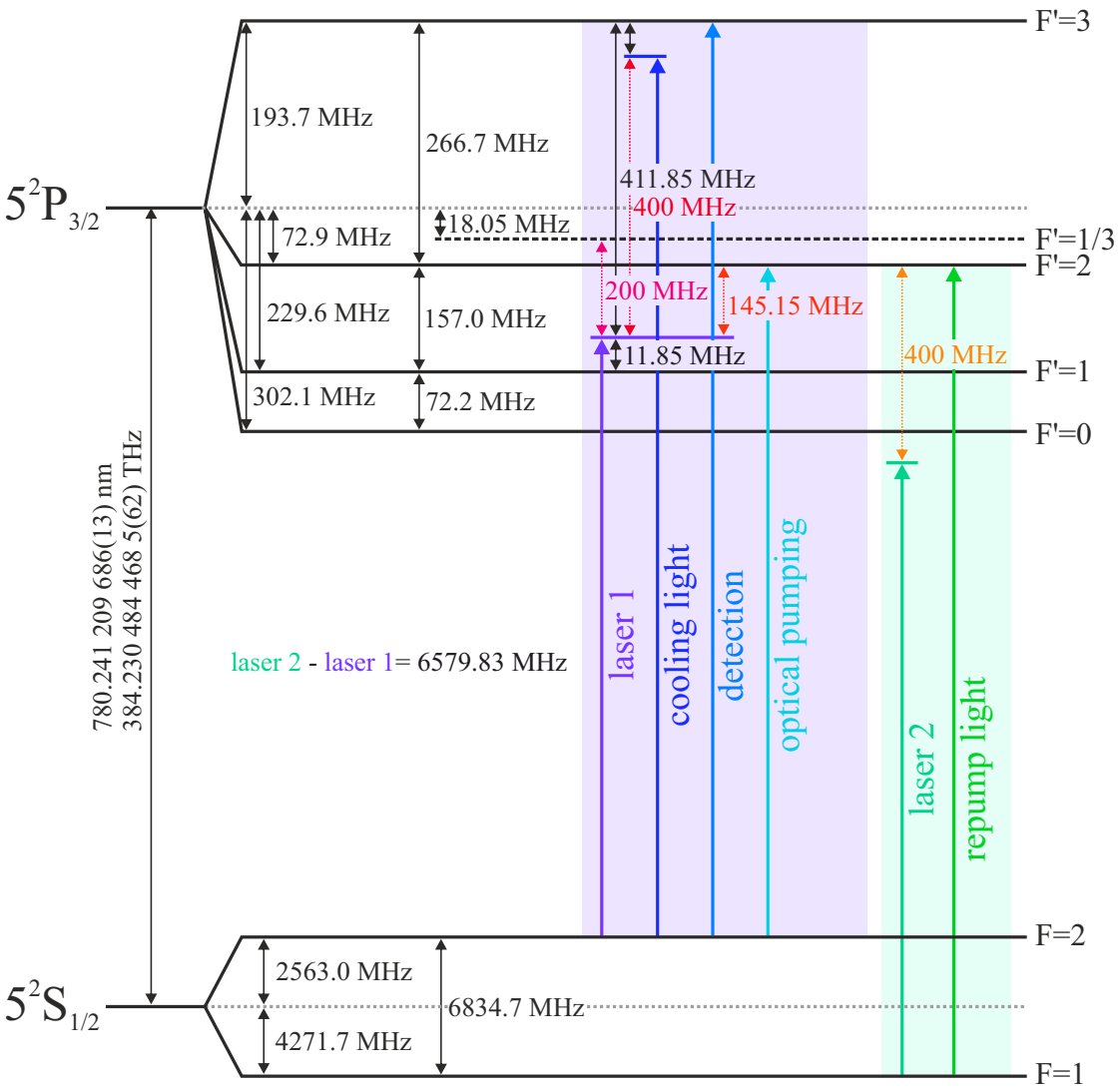

Figure 4.6: Level scheme of ^{87}Rb and laser frequencies used in the experiment. Optical frequencies for the cooling transition, resonant detection and optical pumping (blue hues) are derived from the reference laser (violet and light violet background) that is locked onto the $F = 2 \rightarrow F' = 1/3$ crossover transition with an offset of 200 MHz. Light for pumping the internal atomic state back into the cooling cycle is generated using a second laser diode (green and light green background). Frequency shifts generated by acousto-optical modulators are shown (red to orange hues). The corresponding laser system is shown in Fig. 4.7.

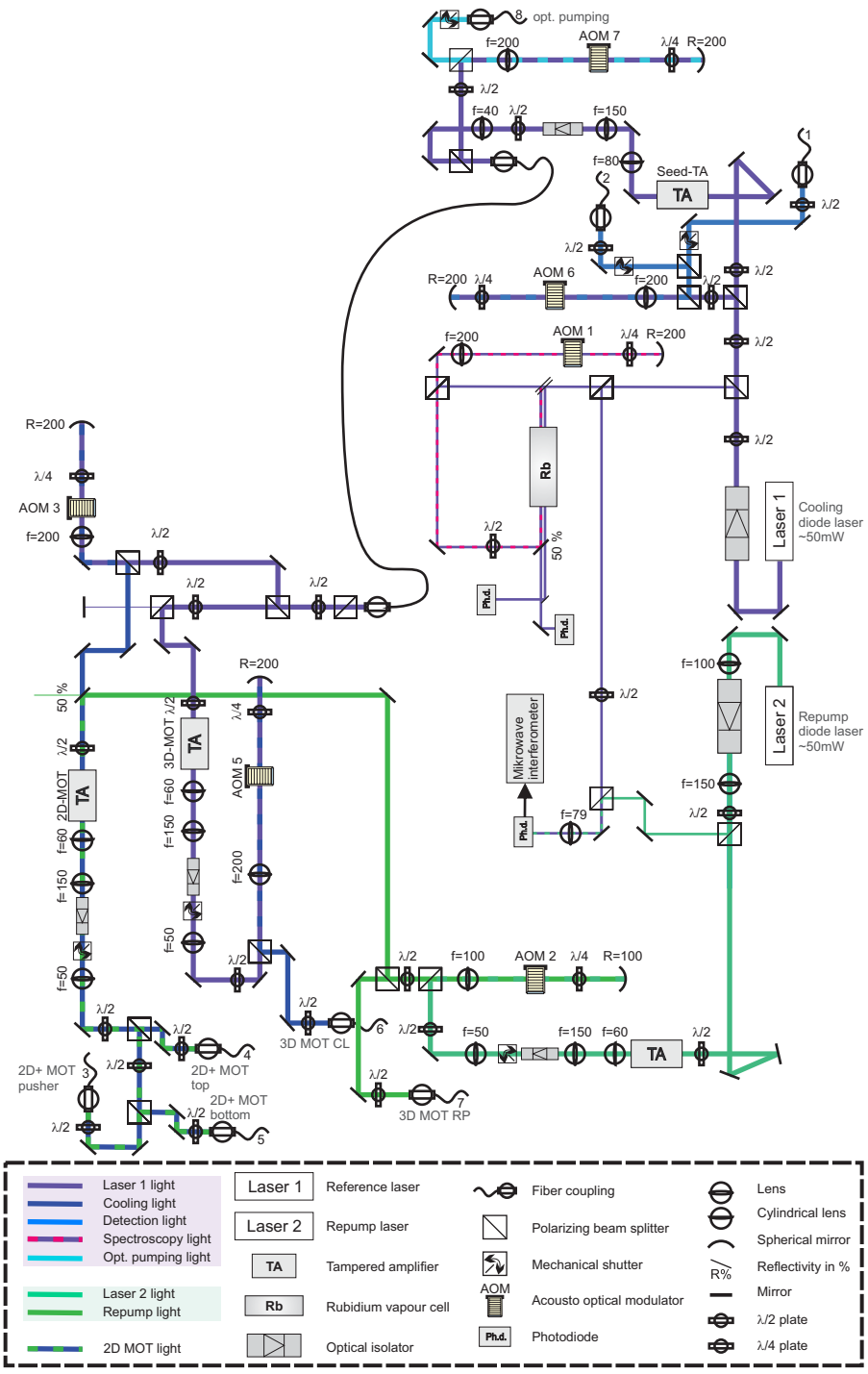

Figure 4.7: Laser light distribution setup on the optics table. Layout of the laser system to generate the desired optical frequencies (compare Fig. 4.6) including all optical components. Fiber couplings are numbered to reference the delivery to different outputs on the vacuum table (Fig. 4.8). This is an updated version of the system shown in [201].

MOT config.	$2w_0$ [mm]	P_{cl} [mW]	Δ_{cl} [MHz]	P_{rp} [mW]
2D$^+$-MOT	87/30	390 mW	13 MHz	-
i-MOT	14	190 mW	13 MHz	210 μW
d-MOT	1.25	146 μW	6 MHz	20 μW

Table 4.1: Laser system parameters. The table lists the Gaussian beam waists w_0, powers P and detunings Δ used to operate the different MOT configurations. The index refers to either the cooling (cl) or the repump (rp) laser system for powers and detunings. The beam waist is in all cases the same for cooling and repump light. The power is to be understood as the total power summed up over all beams. In case of the 2D$^+$-MOT the repump light is generated on the same tapered amplifier as the cooling light and their respective powers cannot be determined easily. For the 2D$^+$-MOT the beam waists refer to the long and short axis of the elliptical beam shape.

vided optical power, a total of four tapered amplifiers (TAs) is used to generate the necessary amount of light for all MOT configurations. One of these TAs is used as a preamplifier for the cooling light, while another is solely amplifing the repump light. The other two generate the needed cooling power for the 2D$^+$-MOT and 3D-MOT, respectively. For the 2D$^+$-MOT repump and cooling light are combined before the last TA, allowing for simultaneous amplification of both needed frequencies. From here on the light is delivered to the dedicated 2D$^+$-MOT optics using three optical fibers. Both 3D-MOT configurations, i-MOT and d-MOT, share a majority of the optical path and components (Fig. 4.8) on the vacuum table. For the operation of the d-MOT a separate power stabilization of the cooling and repump light is needed. The cooling and repump light are being amplified and delivered to the vacuum table separately using two distinct optical fibers. A 200 MHz-AOM in a double-pass configuration as a last element before the fibers in the respective beam paths allows to control the optical power by changing the power of radio frequency input.

Vacuum table distribution optics for 2D$^+$-MOT and 3D-MOT

On the vacuum table the light from the laser table gets feed into different distribution optics for the 2D$^+$-MOT and the 3D-MOT. A total of three fibers delivers the combination of cooling and repumping light to the 2D$^+$-MOT optics. One fiber is specifically used to supply light to the pushing and retarding beam. This beam is collimated to a diameter of 5 mm and split by a polarizing beam splitter. One part acts as the pushing beam, enters the glass cell from the back, gets send

along the zero line of the quadrupole field of the 2D$^+$-MOT coils and is aimed at the reflective front of the differential pumping stage. The other beam acts as a retarding beam and is put into a counter propagating alignment. The other two fibers carry the light used for the two elliptical transversal cooling beams of the 2D$^+$-MOT with a power of about 195 mW each. By passing a quarter wave plate (QWP) the light is polarized circularly. Passing a lens setup of three lenses and a final fourth concave cylindrical lens with a focal length of $f = -150.8$ mm the beams are expended to an elliptical profile of with diameters of 87 mm and 30 mm. On the opposing side of the 2D$^+$-MOT glass cell a highly reflective mirror with a quarter wave plate coating retro-reflects the beams into themselves while changing their polarization in accordance with the magneto-optical trapping principle. Not only does this minimize the amount of optics needed and reduce the alignment effort, it also makes more efficient use of the available optical power.

Cooling and repumping light are delivered by separate fibers to optics for the 3D-MOT configurations. After polarization cleaning, a part of the incoming power is picked off and send onto a dedicated photo diode. In conjunction with a home-build PID controller a control signal is feed back onto the radio frequency power of an AOM in front of the fiber. Both beams are than overlapped by means of a polarization beam splitter and build a common source to drive both i-MOT and d-MOT configuration. Since these two 3D-MOT configurations are spatially superimposed but require different powers and beam diameters, a beam splitter with a splitting ratio of 10 : 90 splits the light into two different paths, one for each configuration. The major part of the power is send into a telescope to become the i-MOT beam with a diameter of about 14 mm. From the remaining light by means of a another telescope the d-MOT beam with a diameter of 1.25 mm is formed. Another balanced beam splitter combines the d-MOT and i-MOT beam again for a super imposed delivery using the same optics. Typical operation points for the 2D$^+$-MOT and 3D-MOT laser systems are listed in Table 4.1. In order not to loose optical power, both output ports of this combining beam splitter each feed into three of the total of six beams of the 3D-MOT configuration. Shutters placed before or after telescopes allow to switch between i-MOT and d-MOT configuration.

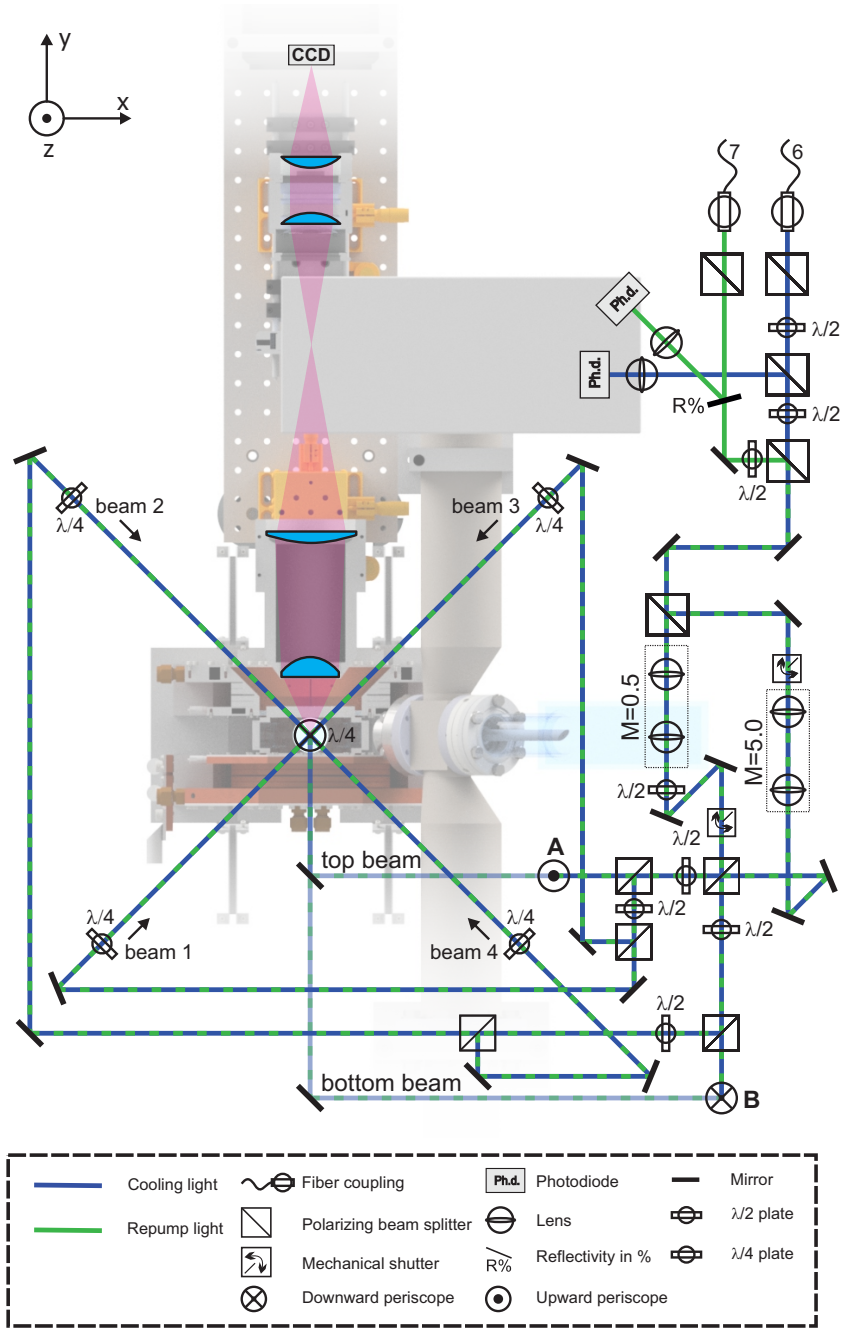

Figure 4.8: Optics of the 3D-MOT for the i-MOT and d-MOT configuration. Layout of the vacuum table optics for both i-MOT and d-MOT configuration overlayed with a top-down view of the experimental setup. The optical pumping beam will enter from the side of the glass cell, aligned with the axis of the homogeneous MOT coils.

4.4 Coil system and magnetic fields

Magnetic fields are essential for the operation of an experiment with ultracold atomic gases. The magnetic moment of the atoms allows the magnetic fields to act on the magnetic sub-levels of the hyperfine structure. Two of the most prominent trapping configurations that require magnetic fields are MOTs and the magnetic trap, both using the minimum of an inhomogeneous magnetic field. In order to drive spin changing collisions, a constant homogeneous magnetic field is needed. This section gives an overview of the coils used within the setup, concentrating on the 3D-MOT, quadrupole coils and homogeneous field coils, as these are the ones especially designed to match the needs of the detection setup. All calculations of circular coils are based on analytic expressions of the magnetic field $\vec{B}$ of a single circular current-carrying wire loop in cylindrical coordintates ρ and z [208]:

$$B_\rho = \frac{\mu_0 I z}{2\pi\alpha^2\beta\rho}\left[\left(a^2+\rho^2+z^2\right)E\left(k^2\right)-\alpha^2 K\left(k^2\right)\right] \tag{4.1}$$

$$B_z = \frac{\mu_0 I}{2\pi\alpha^2\beta}\left[\left(a^2-\rho^2-z^2\right)E\left(k^2\right)+\alpha^2 K\left(k^2\right)\right] \tag{4.2}$$

where the substitutions $\alpha^2 = a^2+\rho^2+z^2-2a\rho$, $\beta^2 = a^2+\rho^2 z^2+2a\rho$ and $k^2 = 1-\frac{\alpha^2}{\beta^2}$ were made. The current through the winding is given by I, the vacuum permeability μ_0, while $K(k^2)$ and $E(k^2)$ are complete elliptic integrals of the first and second kind, respectively, whose results are obtained numerically within Mathematica. In the calculations the spatial extend of the a single wire is taken into account by placing successive turns of a coil at greater distances and radii. The single wire itself is centered with respect to spatial extent of the physical cross section of the wire. The total magnetic field is obtained by summation over all contributing wires. Gradients are calculated by the respective spatial derivatives of the modulus of the magnetic field.

4.4.1 Compensation coils

The compensation coils consist of three pairs of rectangular coils oriented along the principle axis of the experiment with 36 windings each. Their main purpose is to cancel out residual magnetic fields at the position of the atomic sample, like for example the earth magnetic field and stray magnetic fields from the ion getter pumps, by creating a magnetic field that cancels the unwanted residual fields. The dimensions of the box edges formed by the coils are 2000 mm × 2000 mm × 1200 mm.

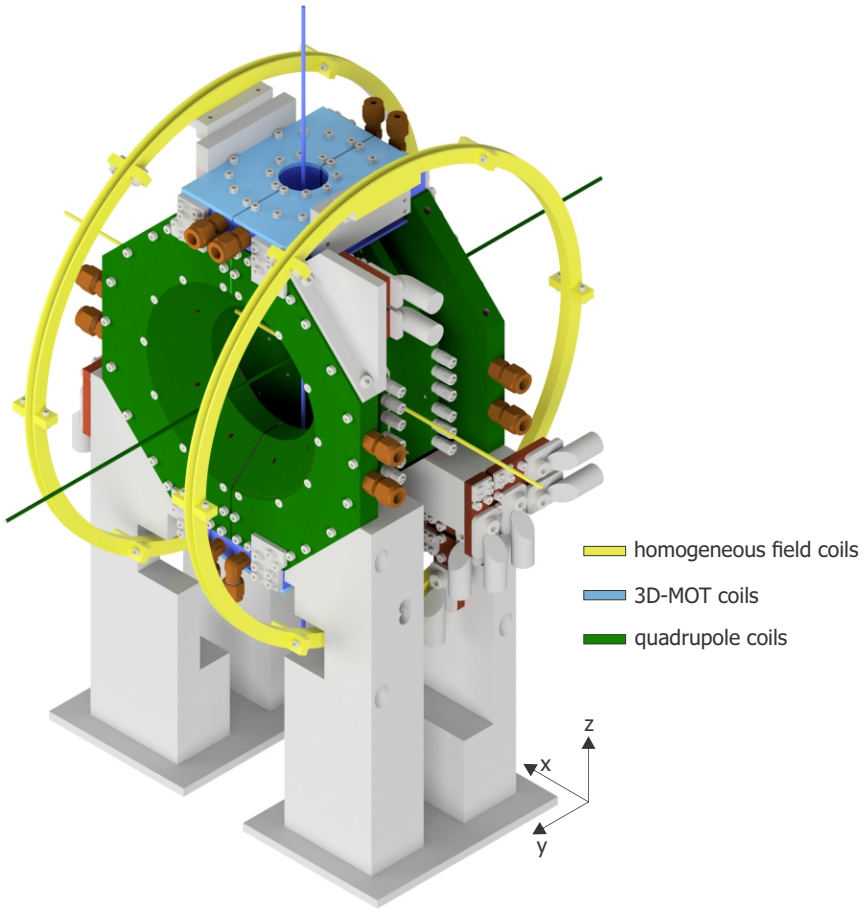

Figure 4.9: Coil assembly. The CAD drawing shows the quadrupole (green), 3DMOT (blue), and homogeneous field coils (yellow) and their mounting structures surrounding the science glass cell. The colored axes through the construction show the main symmetry axis of the correspondingly colored coil pair. For the principle axis of the 3D-MOT coil, quadrupole coil and homogeneous field coil are aligned along the z, y and x axis of the laboratory framework, respectively. The post height is designed to match the common origin of all coil geometries to the center of the science glass cell at a total height of 300 mm above the table surface.

4.4.2 2D$^+$-MOT coils

The 2D$^+$-MOT coils are oriented in a rectangular fashion around the corresponding glass cell and measure 120 mm × 170 mm. Using 81 turns a two dimensional quadrupole field with a gradient of 3.3 $\frac{\mathrm{G}}{\mathrm{Acm}}$ can be created. The currents of the four coils are optimized with respect to the loading speed of the 3D-MOT configuration.

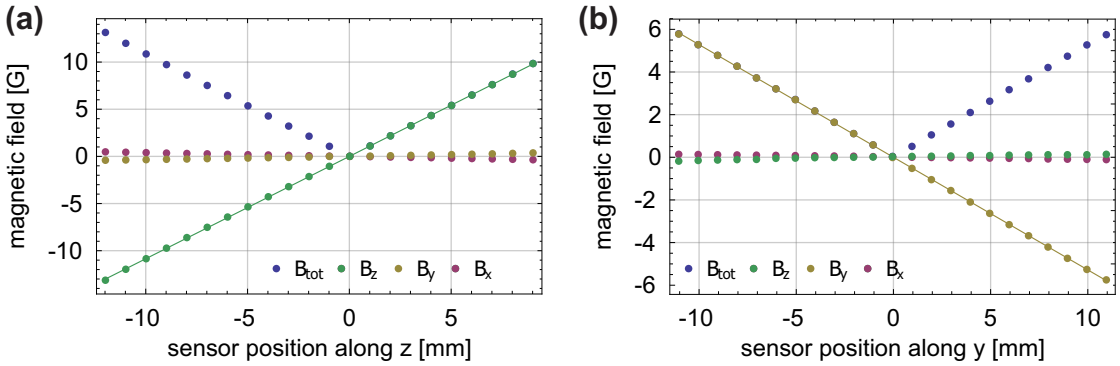

Figure 4.10: Measurement of the 3D-MOT coil field and fitted gradient. All three components of the magnetic field where measured while moving the sensor (F. W. Bell model 7030 Gauss/Tesla meter) along the z (**a**) and y (**b**) direction. **a** The z axis is orientated along the symmetry axis of the 3D-MOT coils and accordingly delivers the stronger gradient of $\mathrm{d}B_z/\mathrm{d}z = 10.85(2)\,\mathrm{G/cm}$ at a current of $I = 92\,\mathrm{A}$. Normalizing for the applied current this results in $0.1180(2)\,\mathrm{G/(A\,cm)}$. **b** Along the weaker y direction a gradient of $\mathrm{d}B_y/\mathrm{d}y = -5.28(1)\,\mathrm{G/cm}$ was measured, yielding $0.0574(1)\,\mathrm{G/(A\,cm)}$.

4.4.3 3D-MOT coils

The 3D-MOT coil pair (Fig. 4.9) aims at generating a gradient of 15 G/cm that is needed to realize both 3D-MOT traps, i.e. the i-MOT and the d-MOT. Each coil is made up of 40 windings in two layers of 20 windings each, fully using up the space that is left between the quadrupole coils. By design the innermost winding starts with a radius of 18.375 mm set by the mounting frame. The two coils are positioned at a distance of 187.5 mm and the wire cross section is 6 mm × 1.12 mm. For the principle axis, according to the design, a value of $0.106\,\frac{\mathrm{G}}{\mathrm{Acm}}$ was estimated, implying that a current of 142 A is needed to create the desired gradient of 15 G/cm. While the coil pair is estimated to have a total resistance of 0.038 Ω, resulting in a needed voltage of 6 V. Figure 4.10 depicts the results of measuring the generated magnetic field gradient of the coils. The measured value of $0.118\,\frac{\mathrm{G}}{\mathrm{Acm}}$ slightly deviates from the designed value just as the measured resistance of 0.04 Ω. The currents were measured using a current transducer (LEM Danfysik IT 200-S Ultrastab). This deviation can be explained by the fact, that during the winding of the coil in two layers, one layer is wound from the outside in, the innermost winding has to make a transition from the lower layer to the top layer, and then the top layer is wound from the inside out. All calculations where based on perfect circular loops, not following the actual spiral shape of a coil. Hence the coil is better described by an inner layer of 21 turns and a top layer of 20 turns, summing up to a total of 41 turns per coil. The calculated values of 0.114 G/(A cm) and 0.04 Ω match the experimentally

determined values much closer.

Splitting the mounting frame into two half circles and merging them with a 1 mm phenolic paper (Pertinax) spacer in between electrically isolates both halves from each other in order to prevent eddy currents. Running the desired gradient continuously generates about 862 W of heat that need to be dissipated, but will be at reduced by half due the duty cycle of the coils. To counter the heat generation, the mounting structure is designed to feature water cooling on its outside surface. Due to the split geometry of the coil mount, it is necessary to cool both halves of each coil separately. To this end, the outside surfaces feature connectors (Serto SO 41121-8-1/8) compatible with 8 mm tubing from Serto as well as tranches that are closed with a lid and surface sealant (Loctite SI 5926). A chiller (H.I.B Industriekühlsysteme RK/W-03000-L-R23-011E-2-IW) with a cooling capacity of 3 kW connected to the coils water cooling circuit. The current is supplied by two Gen-7.5-1000 from TDK Lambda that are connected in series and hence can deliver up to 1000A at 15 V.

4.4.4 Homogeneous field coils

In order to be able to drive spin dynamics in a Bose-Einstein condensate a quantization axis for the magnetic sublevels of ^{87}Rb is needed. The magnetic field created by the homogeneous field coils (Fig. 4.9) lifts the degeneracy between the magnetic sublevels. The coil pair consists of two coils with 12 windings of round enameled copper wire with a diameter of 1 mm, that is wound in three layers of four windings each. The coil mount is split in six parts per coil to allow for electrical isolation and easy installation.

4.4.5 Quadrupole coils

The design goal for the quadrupole coils (Fig. 4.9 and 4.11) is to allow for the generation of a steep magnetic trap, i.e. the creation of a strong gradient field on the order of 300 G/cm. Within the experimental sequence the magnetic trap is used as an intermediate form of trapping, enabling the transition from i-MOT to the optical dipole trap. Additionally it allows to carry out a first step of evaporative cooling.

The desired gradient can be maximized by increasing the current through the coils or by placing the coil pair closer to their geometrical center and making the radius of the windings smaller. These measures find their limits in the physical limitations of the science glass cell, the optical access needed for detection setup and the 14 mm i-MOT beams. Figure 4.11 c helps to gain a geometrical understanding of this situation by superimposing the spatial requirements of

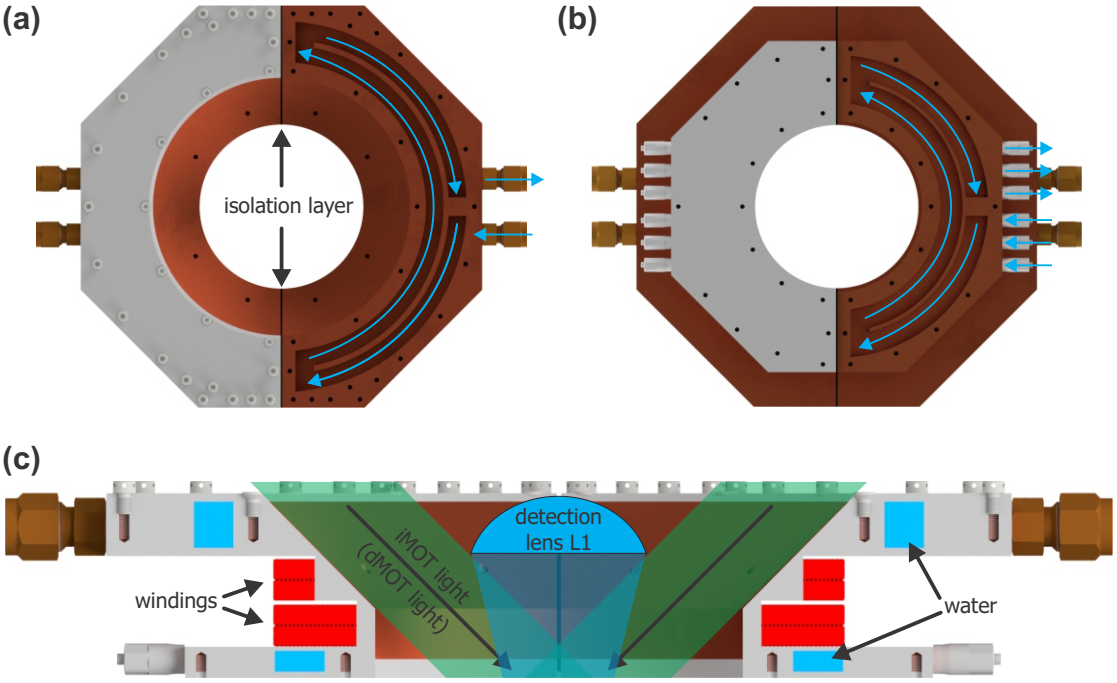

Figure 4.11: Mounting structure of the quadrupole coils. a Outside view. The mount is split along its vertical axis and separated by a 1 mm thick phenolic paper (Pertinax) spacer to prevent eddy currents. The left half is shown with the water cooling lid on, the right half exposes the tranches underneath. The water inlets are compatible with 8 mm tubing from Serto. **b** Inside view. This side is the one facing the science glass cell. It features another layer of water cooling while trying to place the coil as close to the cell as possible. The left side is shown with the lid on, while the right side reveals the tranches of the water cooling. The water inlets are connectors from Festo that are compatible to a 1 mm tube. **c** Cut cross section view. This representation shows the 62 current-carrying windings of the coil in solid red. They are distributed in 4 layers of two times 20 and two times eleven windings. The space occupied by a pair of big 14 mm cooling beams for the i-MOT are depicted as green shaded areas coming in at an angle of 45 °. These beams prohibit the windings to be places closer to the center. The detection lens L1 reaches inside the coil mount to make full use of its large numerical aperture.

the i-MOT beams, the large numerical aperture of the detection and the coils. Only one half of the coil pair is shown, the other being an exact mirror image. Also increasing the current through the coil will increase the dissipated heat and result in an stronger, undesirable temperature increase.

The mounting frame of the quadrupole coils is designed to solve these geo-

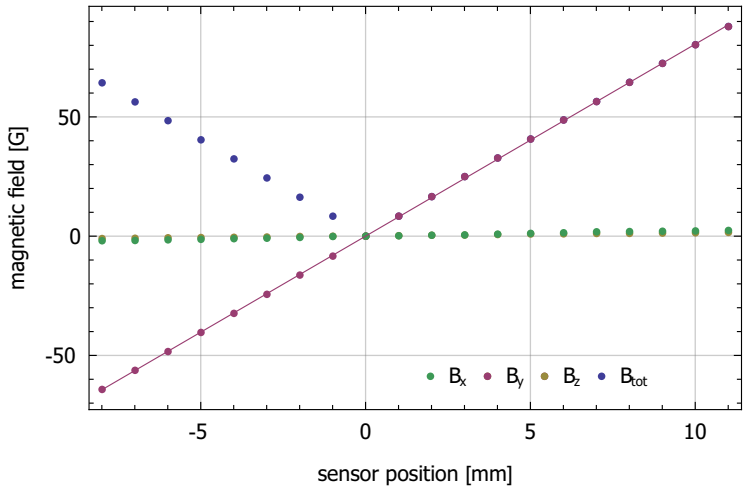

Figure 4.12: Measurement of the quadrupole coil field and fitted gradient along the strong axis. The graph shows the measured field strength of the quadrupole coils for a current of $I = 45\,\mathrm{A}$ along their strong axis. The linear fit yields a slope of $\mathrm{d}B_y/\mathrm{d}y = 80.51(14)\,\mathrm{G/cm}$. This results in a universal gradient of $1.790(3)\,\mathrm{G/A\,cm}$, which is in good agreement with the value of $1.779\,\mathrm{G/A\,cm}$ that was calculated for the designed geometry. The deviations between the measured and calculated value can be explained by the fact that the innermost turn of coils has to move from one layer to another.

metrical and thermal challenges by maintaining a large optical access, hold the desired number of wire turns as well as allow for water cooling of the wire during operation. Copper was chosen as the material for the mount as it has very good heat conductance. The downside of the choice of material is that the good electrical conductance makes the circular mounting structure susceptible to eddy currents caused by switching the coils on and off. These eddy currents in turn can induce magnetic fields that can disturb the control over the atomic sample. To avoid this, the structure is split in two half circles. A gap of 1 mm is filled with isolating phenolic paper (Pertinax) and glued together to form the full mount of one coil.

Water Cooling

Due to the splitting of the coil mounts into half circles to supress eddy currents, the water cooling needs to be incorporated on each half circle separately. Each half circle part features trenches, that are used to actively cool the mounting structure by connecting it to a water cooling circuit. The trenches are milled into the outside and inside plate of the mounting structure. They are closed by respective lids that are screwed to the mounting body and sealed by the

application of sealant (Loctite SI 5926) across the whole surface. While the outside water cooling features deeper trenches of and with a cross section of 104.5 mm^2 and tubing connectors (Serto SI 41121-8-1/8) that connect 8 mm tubing, the inside water cooling close to the science glass cell is especially delicate. Without any water cooling on the inside, the windings located close to the science glass cell would become the hottest part of the coil during operation. These windings were located furthest away from outside water cooling and the heat transport across the layers of windings is deteriorated due to the isolation varnish on the wires as well as the resin holding the layers in place. Having any device close to the science glass cell heating up substantially could cause a temperature gradient across the glass cell resulting in either a leak or broken vacuum. Yet moving the windings away from the glass cell to make room for water cooling also increases the needed current for reaching the desired gradient, and thus also increases the deposited heat and finally the resulting temperature during operation. In essence, the water cooling on the inside of the coils has to take up as little space as possible. The trenches on the inside surface feature a cross section of 60 mm^2 while the copper lid is only 1.5 mm thick. Temperature monitoring is done by a series of 36 negative temperature coefficient thermistors (EPCOS B57861S, NTC 10 kΩ) that are glued (Fischer Elektronik Wärmeleitkleber WLK 120) to the coil mounting structure and read in using home-build electronics in combination with a LabView computer interface. Cooling is provided by a dedicated chiller (H.I.B Industriekühlsysteme RK/W-03000-L-R23-011E-2-IW) with a cooling capability of 3 kW. A huge cooling capacity is needed as a steady state operations and the desired specs would result in about 5 kW Joule heating. By assuming a duty cycle of 20 % or less the heat can rougly be reduced to 1 kW which is well within the chillers cooling capacity.

Windings

Splitting the windings into four cascading layers of a total of 62 windings, i.e. two layers of 20 and two layers of 11, makes the best use of the space available under the geometrical restrictions while trying to keep the number of turns low to reduce the coils inductance. A flat enameled wire with a cross section of 5 mm × 1 mm is used to create the turns. The inner radius of the inner most winding is 48.4 mm and the distance between the coils is 52.75 mm. The simulation shows that with its 1.779 $\frac{G}{Acm}$ along the main axis, the coil pair will be able to produce a gradient of 300 $\frac{G}{cm}$ when supplied with a current of 168.668 A. Due to the total resistance of the coils of 0.18 Ω a voltage of at least 30 V is needed. As a current driver a Gen-60-250 from TDK Lambda able to drive up to 250 A at 60 V is used.

coil pair	∇B or B	I [A]
$2D^+$-MOT	14.85 $\frac{G}{cm}$	4.5
3D-MOT	15.00 $\frac{G}{cm}$	151
QF	300.00 $\frac{G}{cm}$	168.67
HOM	3 G	3.98
COMP	270 $\frac{mG}{A}$	max. 3

Table 4.2: The table lists the desired operation points of the coil pairs involved in the system.

4.4.6 Summary

The integrated design of all three main coil setups (i.e 3D-MOT, quadrupole fiel coils and homogenous field coils) features water cooling for the 3D-MOT and quadrupole coils. Simultaneously, it grants optical access through all nine viewports of the glass cell, especially for the big 14 mm i-MOT beams. Eddy currents are countered by avoiding any closed conductive loop around the glass cell within the mount design. The coil mounts themselves are made up of two identical parts separated by 1 mm phenolic paper (Pertinax). With this coil concept the apparatus is equipped for all magnetic fields that need to be generated during the experimental procedure (Fig. 4.1).

4.5 d-MOT detection system

The d-MOT detection system is built to register as many fluorescence photons from the atoms trapped in the d-MOT as possible. At the same time its equally important task is to reduce the amount of collected background photons. This is achieved by maximizing the amount of initially collected photons and minimizing the photon losses within the imaging system. Additionally background contributions from out of focus areas and scattering centers are to be minimized.

4.5.1 Optical components

A central component of the detection system is the first aspheric lens (Edmund Optics GmbH, ED67283, 50 mm diameter, 48.34 mm working distance, 50 mm

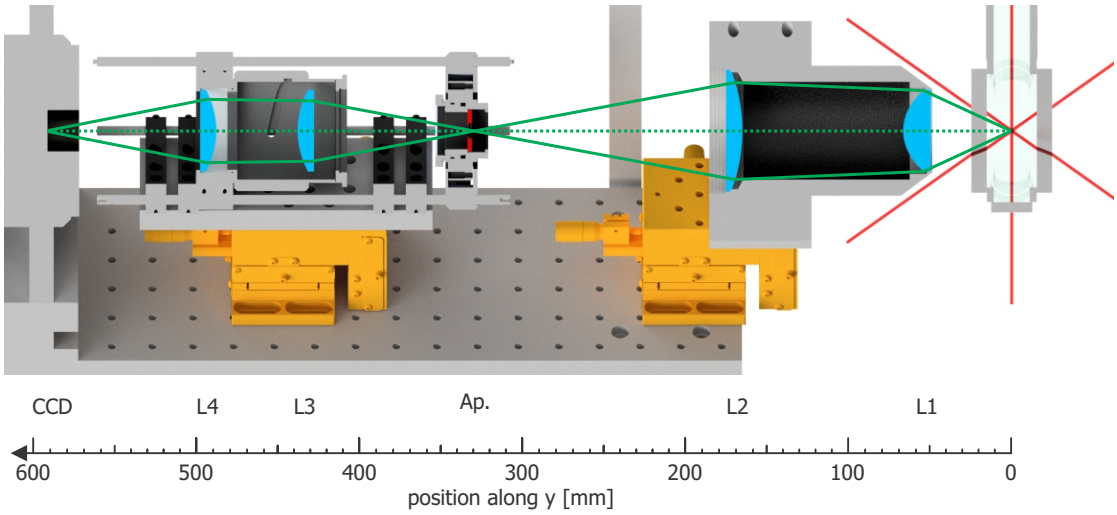

Figure 4.13: Cut through the CAD drawing of the detection optics path of the d-MOT imaging system. On the right hand side the glass cell with the six d-MOT beams (red) is shown. Their cross section marks the position of the atomic sample. Green lines mark the optical path of the detection system. The first imaging lens L1 (blue) gathers about 5 % of the total light emitted by the atoms. Together with the second imaging lens L2 (blue) an intermediate image is formed at the position of an exchangable aperture (red). The aperture reduces unwanted stray light that originates in out-of-focus planes. Another lens pair consisting of L3 and L4 (blue) relays the image from the pinhole plane onto the CCD chip. The solid green lines outline the bounding rays of the imaging path. The dashed green line represents the imaging axis. Two three-dimensional translation stages (orange) allow for precise focusing of the optics onto the position of the atomic sample. An adjustable lens tube (collimation adapter) ensures that the image can always be relayed onto the CCD camera chip. When in operation the detection system is fully enclosed to keep stray light from entering.

focal length), made out of fused silica with an effective numerical aperture NA of 0.448 (L1 in Fig. 4.13). In conjunction with three more ensuing lenses, the collected photons are imaged onto a low noise CCD camera chip (Princeton Instruments, 1024 BR eXcelon liquid cooled, back-illuminated deep depletion CCD). The covered solid angle of about $\Omega = \mathrm{NA}^2/4 \approx 5\,\%$ quantifies the relative amount of collected photons and is the main design parameter. The anti-reflection coating reduces the reflected portion of the collected light at the desired wavelength of 780 nm down to below 0.25 %, i.e. is a transmittance of $T_{1,2} = 99.75\,\%$ per pass. A benefit of the large working distance is, that this allows the positioning of the first lens already outside the vacuum at a distance of 24.9 mm from the surface of the science glass cell.

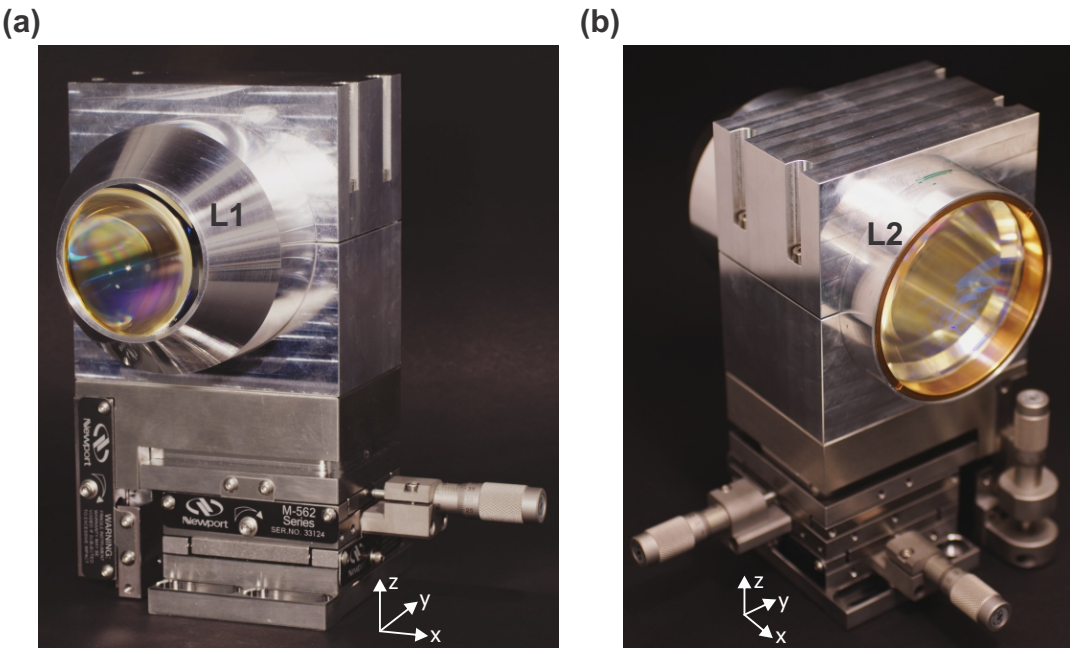

Figure 4.14: Objective lens. a Front view of the objective lens showing its flat front surface with a diameter of 50 mm. **b** The back view of the second lens in the imaging system reveals its diameter of 75 mm and the mounts brass retaining ring. The objective lens tube is mounted as rigidly as possible to rule out the influence of vibrations. A three dimensional translation stage enables tuning the focus of the detection system onto the position of the d-MOT.

The second lens (L2 in Fig. 4.13) within the imaging system is a plano-convex lens (Edmund Optics GmbH, ED86917, 75 mm diameter, 142.45 mm working distance, 150 mm focal length) made from N-BK7 and subjected to the same anti-reflection coating. Together with the first lens it is housed inside a home-built aluminum lens tube to fix the relative position of the lenses. Painting the inside of the tube black (Albrecht Schultafellack, matt) reduces the stray light that enters the first lens. In combination, the first two lenses form an intermediate image 158.35 mm behind the second lens. A three-dimensional translation stage (Newport M562-XYZ) with micrometer actuators (Newport SM-13) allows to focus precisely on the position of the atomic sample.

At the intermediate image plane a pinhole is positioned (Fig. 4.13). This confocal setup blocks light, that originates behind or in front of the focus region. Any light source that is not located within the focal plane will appear to be defocused in the intermediate image plane, allowing for a spatial filter to cut out only the region of interest and to remove unwanted background light. The three-dimensional translation mount (Thorlabs CXYZ1M) allows positioning the

pinhole in the intermediate image plane and select the desired region of interest in the lateral directions.

Lenses three and four (L3 and L4 in Fig. 4.13) are both plano-convex aspheric lenses made of N-BK7 (Thorlabs, AL50100-B, 50 mm diamater, 100 mm focal length). The applied broadband anti-reflection coating reduces reflections at 780 nm down to 0.19 %. This allows to assume a transmittance of $T_{3,4} = 99.81\,\%$ per pass. These last two lenses relay the intermediate image without any further magnification and are mounted in a threaded lens tube (Thorlabs SM2F) that allows for the adjustment of the distance between the lenses in order to focus the image correctly onto the camera's (Princeton Instruments PIXIS 1024BR eXcelon) CCD chip (CCD in Fig. 4.13). An additional three-dimensional translation stage (Newport M562-XYZ and SM-13) supports the two lenses (L3 and L4).

The total magnification $M = 2.62$ of the imaging system is determined by the choice of the first two lenses. In combination with the physical pixel size of the CCD camera chip of $13\,\mu\text{m} \times 13\,\mu\text{m}$ for the total of 1024×1024 pixels this results in a total image size of $5.08\,\text{mm} \times 5.08\,\text{mm}$. Alternatively, one pixel corresponds to a distance of $4.96\,\mu\text{m}$ in the object plane. For the application in an accurate atom counting detection, the CCD camera's most important property is its quantum efficiency QE = 98 %, describing the ratio of the number of primary electrons generated by the CCD chip to the number of incident photons hitting the CCD chip. The window in front of the chip features an angled cut at 1.5 ° to avoid etalon effects and an anti-reflection coating on both sides that allows for a transmittance of $T_{\text{CCD}} = 99.8\,\%$.

The total detection efficiency is given as a product of all the factors mentioned above and can be written as

$$\eta = \Omega \times \text{QE} \times \prod_i T_i^{k_i}, \tag{4.3}$$

where Ω and QE are the relative covered solid angle and the quantum efficiency of the CCD camera chip, respectively. The transmittances T_i need to be considered for every surface within the detection path and the exponents k_i simply take care of multiple passes of comparable surfaces, e.g. same anti-reflection coatings. A detailed overview of the relevant influences is given in Tab. 4.3, showing that the total expected detection efficiency is $\eta = 4.71\,\%$, a value that is more than four times higher than in comparable systems [209]. The advantages of the setup presented in this work are the large numerical aperture of the first lens, vastly increasing the covered solid angle as well as the anti-reflection coat-

component	symbol	factor	occur.	total contribution
science cell glass surface	T	98.92 %	2	97.85 %
lens 1 solid angle	Ω	5.02 %	-	5.02 %
lens 1,2 surface	T	99.75 %	4	99.00 %
lens 3,4 surface	T	99.81 %	4	99.26 %
camera window surface	T	99.80 %	2	99.60 %
CCD chip quantum efficiency	QE	98.00 %	-	98.00 %
			total η	4.71 %

Table 4.3: Detection efficiency of the d-MOT detection system. The table lists the different quantities influencing the total detection efficiency of the d-MOT detection setup and their respective contribution to it. The comparably large numerical aperture for a MOT detection system paired with the excellent quantum efficiency of the camera enable excellent photon counting rates (Chapter 5.3).

ing of the vacuum science cell windows[14].

While for a single d-MOT only the photons emitted from the atoms within the trap need to be collected and counted, this becomes different when considering counting the atoms in multiple traps. Spatial separations that are typically reached in split magneto-optical trapping setups of a few 10 μm [209] do not pose requirements comparable to single site resolution of an optical lattice. The theoretical resolution of 1.2 μm of the imaging system is limited by the pixel size due to the small magnification of $M = 2.6$. Any feature on a scale below 5 μm will be imaged onto a single pixel. But then again a smaller magnification distributes the signal across fewer pixels and thus reduces readout noise, increases read out speed and picks up less background across the signal area on the CCD chip. Although, for larger atom numbers the amount of pixels in the region of interest can become important in order to avoid saturation of single pixels.

The gain factor of the camera's conversion from primary electrons to digital counts was measured to be $g = 1.089(4)$ (Fig. 4.15). Additionally the manufacturers value for the quantum efficiency was verified as QE = 97(1) %. In order to relate the camera counts to a fluorescence signal it is plausible to gather all

[14]Typical comparable glass cells without anti-reflection coating only offer a transmittance of $T = 96$ % per pass.

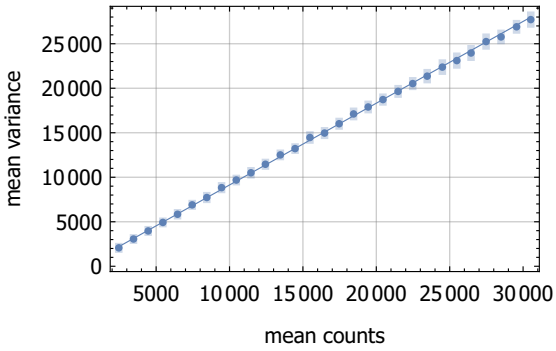

Figure 4.15: Calibration of the camera gain. Using the slope of the linear relation between the variance and the mean number of digital camera counts the gain of the camera is estimated to be $g = 1.089(4)$. This procedure is described in more detail in the Appendix of [46].

the factors that determine how many of those photons that an atom emits are converted to camera counts, forming an effective detection efficiency

$$\tilde{\eta} = \eta / g = 4.33\,\%. \tag{4.4}$$

4.5.2 Scattering estimation

In order to reliably derive accurate atom numbers from the detected photons, the background signal and the corresponding noise of the background signal need to be sufficiently small. Thus, the potential background signal during the imaging process needs to be considered and estimated already in the design process as well as characterized experimentally. For the estimation, possible scattering sources that could interact with the d-MOT beams as well as probable optical paths through the imaging system onto the CCD chip are being reviewed. The only light source that necessarily is turned on during the d-MOT imaging sequence are the six d-MOT cooling and repumping light beams. By reducing the size of these beams to 1.25 mm, the likeliness of scattering events is reduced from the first. Due to the immediate vicinity to the detection lens, the science glass cell is the most likely source for reflections and scattering events that may cause photons of the cooling beams to be captured by the detection setup (Fig. 4.16). In a typical detection scenario, the d-MOT may run at a power of about $P_{\mathrm{d-MOT}} = 150\,\mu\mathrm{W}$. Dividing this by the energy $E_{\mathrm{ph}} = hc/\lambda$ of a single photon at a wavelength $\lambda = 780\,\mathrm{nm}$ yields the total rate of incident photons

$$r_{\mathrm{inc}} = \frac{P_{\mathrm{d-MOT}}}{E_{\mathrm{ph}}} = \frac{\lambda P_{\mathrm{d-MOT}}}{hc} \approx 6 \times 10^{14}\,\mathrm{photons/s}, \tag{4.5}$$

where h is the Planck constant and c the speed of light. Depending on the amount of reflections and the potential encounter of a scattering center, only a

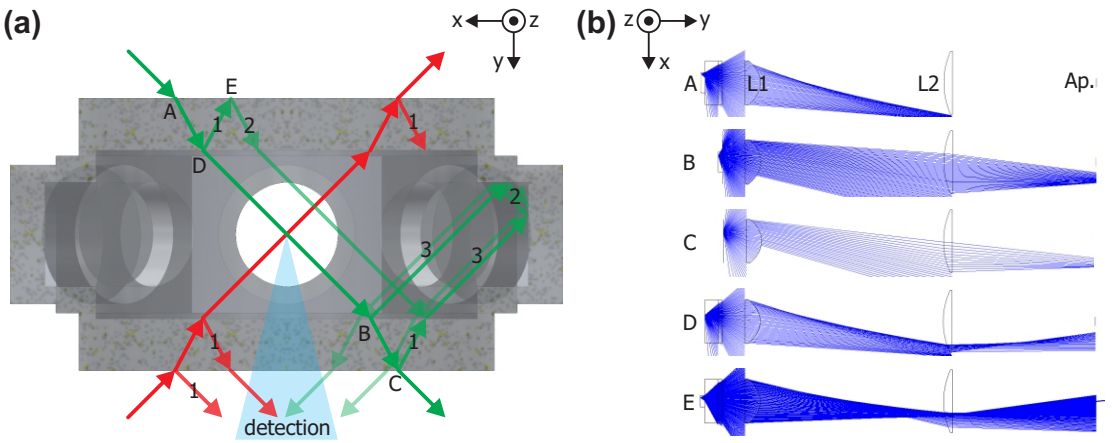

Figure 4.16: Possible reflections and scattering sources of the d-MOT beams and suppression of out-of-focus light sources by the detection aperture. a The top view shows a horizontal cut through the science glass cell with the large side windows on the top and bottom of the sketch respectively. The blue cone depicts the solid angle that is covered by the detection lens. Cooling light beams for the d-MOT entering from the front (back) are shown in red (green). Each surface is a potential source for reflections and surface scattering. The numbers display the multipe orders of reflection that can occur on surfaces of the glass cell. **b** Ray tracing simulation of possible scattering light entering the detection system originating at the positions marked by the corresponding capital letters in **a**. L1, L2 and Ap. mark the position of the first and second detection lens as well as the aperture in the intermediate image plane. As can be seen from position E only close to the detection axis it is possible for light from out-of-focus sources to pass the detection 1 mm aperture.

fraction of these photons will be caught by the detection system. Table 4.4 gives an overview of the relevant parameters for the estimation of these background contributions. The noise of the background signal is the real quantity of interest. If the background noise is larger than the signal of a single atom, no accurate atom number detection will be possible. In fact, the background noise level should only be on the order of a fraction of a single atom signal for the detection to work reliably. In anticipation of Chapter 5, a single atom signal for our applied experimental parameters is on the order of $r_{\mathrm{atom}} = 6 \times 10^5$ photons/s. Assuming the noise of the background follows a Poisson distribution, the standard deviation is given by the square root of its mean. From these assumptions, a critical suppression value of 6×10^{-4} can be derived.[15] When the incident cooling light enters the detection setup with a weaker attenuation, it becomes a thread to the

[15]This critical suppression is an overestimation in the sense, that it does assume a perfect spatial overlap between the background signal and the atom signal on the camera chip. In reality this will never be the case.

source	symbol	probability
reflections inside of the chamber (multiple $n > 1$)	$P_{\text{ref}}^{(n)}$	0.83 %
science cell surface quality (scattering)	P_{scat}	0.02 %
detection efficiency	η	4.71 %
pinhole suppression	P_{supp}	0.07 %

Table 4.4: Scatter estimation. This table lists the different estimated probabilities involved in scattered light from the cooling laser beams entering the detection system. The reflection probability is derived from the reflectivity curves of the applied coating supplied by the manufacturer. Scattering can occur when the cooling light beams hit an imperfection in the glass cell surface. The surface quality is described by the scratch-dig specifications that can be used to estimate the probability of the beam hitting an imperfection. This value has been verified experimentally in a dedicated setup [201]. The detection efficiency is derived in Table 4.3. The pinhole suppression is an estimate derived from ray tracing simulations for different points across the in- and outside surfaces the big windows of the science glass cell.

detection principle.

Because of the symmetry of the problem, it is sufficient to consider only two cooling beams. One entering from the front, along the detection setup and one from the back, entering through the window opposite to the detection (Fig. 4.16). For the parallel beam, direct first order reflections pose the biggest threat, as they are still very powerful and will contribute the most of the background offset. While these first order reflections might enter the first detection lens they will inevitably end up on the aperture, such that they are not directly hitting the CCD chip. Indeed, if the first order reflection were to be distributed across the same area on the CCD chip, accurate atom detection would not be possible. Hence, to reduce their chance of scattering inside the lens tube, the inside surface of the lens tube has been painted black (Albrecht Schultafellack, matt).

Higher order reflections might bring the beam in a position, where scattering on a surface of the science glass cell could allow a portion of the light to pass the aperture (Fig. 4.16b). But then again, reflecting the beam twice should reduce its intensity below the threshold needed for accurate atom detection. In cases where one reflection followed by a scattering event occurs, only a fraction of 8×10^{-8} of the incident photons will reach the position of the aperture. For

the presented use case, this turns out to be about 5×10^7 photons/s. In conclusion, all combinations of the probabilities listed in Table 4.4 will result in small background contributions compared to the first order reflections and can be neglected. The experimental results in chapter 5.2.2 demonstrate that painting the lens tube from the inside is sufficient to reduce the background noise to a level that corresponds to 6 % of the signal of a single atom, as during the experiment neither the beam blocks nor the detection aperture where in place. This also suggests that the background level was dominated by contributions from the first order reflections. Extrapolating the measured background count rate of 3.76(3) Mcts/s to the whole CCD chip size yields rate of $5.30(4) \times 10^8$ photons/s. Comparing this to the a direct reflection of the incident photons on the glass cell window results in a suppression of about 10^{-3} by only painting the inside of the lens tube. In a previous stage of the apparatus, the addition of beam blocks along the edges of the detection cone proved useful to keep these reflections from even hitting the first lens at the cost of an insignificant reduction of the numerical aperture. Even for the first order reflections, applying only one of three possible means (i.e. reflection beam blocks, detection aperture and darkened lens tube) to reduce the background signal is sufficient.

4.6 Experimental control

Running an atom optics experiment requires the control of many experimental parameters. Light fields need to be controlled in power and frequency by means of the radio frequency and power supplied to an acousto-optical modulator. Beam paths are altered by closing and opening optical shutters. Magnetic fields are created by running a particular current through special coil geometries. All these variables need to be controlled meticulously and timed precisely in the form of digital and analog control voltages that are sent to the respective drivers. The experimental control used for this apparatus is based on the system used in a former experiment described in [210]. Here, only the most important technical aspects are rounded up.

The experimental control is driven by a LabView software that is run on a field-programmable gate array (FPGA, Virtex-II 3M) on a commercial PCI-card (National Instruments NI PCI-7813R R Series Digital RIO) in a designated computer system. The FPGA features an internal clock cycle of 40 MHz with an accuracy of ±100 ppm and a minimal time step of 5 ns. A total of 160 binary output ports (TTL-standard) is available. Digital-analog converters (National Instruments NI 9263) convert 10 of the TTL-channels into 4 analog channels that can deliver ±10 V with a 16 bit resolution at sampling rate of 100 kSamples/s. They are used in three groups of four (National Instruments 9151 - R Series

Expansion Chassis) to create a total of 48 analog channels. The remaining 40 TTL channels are directly made accessible through a breakout board equipped with BNC and SMA connectors.

4.7 Summary

This section outlined the design process, main features and construction process of an experimental apparatus that aims at performing quantum-enhanced atom interferometry. The successful build up of $2D^+$-MOT, i-MOT and d-MOT together with the detection system allows for a first test the systems' accurate atom counting capabilities (Chapter 5) — they key subsystem will enable atom interferometry at the Heisenberg limit. Beyond this, the implemented coil system is able to supply the needed magnetic fields and gradients for all steps of the experimental procedure (Fig. 4.1). Optical molasses and magnetic trapping are the next subsystems to be tested with all their components already in place. Pending the finalization of the deployment of the optical dipole trap optics, optical trapping and Bose-Einstein condensation will be possible.

Chapter 5

Accurate atom counting

Within this chapter, the experimental sequence to operate and calibrate the detection MOT (d-MOT) is outlined. The gathered fluorescence signal of atoms captured in the d-MOT as well as the background signal is analyzed. In this process the characteristic steps that correspond to integer atom numbers in the d-MOTare revealed. A calibration of the atom number is performed that will allow for on-the-fly evaluation of the atom number. Further analysis of the statistics of the steps in the fluorescence signal yields an estimate of the trapping life time of the atoms of $\tau_{\text{life}} = 540(150)\,\text{s}$. A noise model for the two-point variance of the atom counting signal is presented, revealing the limiting noise contributions from scattering rate fluctuations. The noise model further demonstrates that the single-atom counting limit will be reached at $N_{\text{ats}} = 390(20)$ atoms, when a successful scattering rate drift compensation is applied.

5.1 Experimental sequence

In order to verify and characterize the accurate atom counting capabilities of the experimental apparatus, statistics of the background signal of the d-MOT configuration and of the fluorescence signal of atoms trapped in the d-MOT need to be gathered. Thus, the experimental sequence includes an initial background image that is taken right at the beginning, before any atoms enter the science glass cell. During this exposure, the d-MOT cooling laser beams are turned on and running at the operational parameters with a saturation parameter of $s_0 = 6.65$ and a detuning of $\Delta = 2\pi \times 6\,\text{MHz}$. The exposure time of 90 ms is also matched to that of the fluorescence acquisition that happens later during the sequence. Once the background image has been acquired and the camera picture is being read out, the 2D^+-MOT and i-MOT are activated simultaneously to transfer atoms from the 2D^+-MOT glass cell into the science chamber where

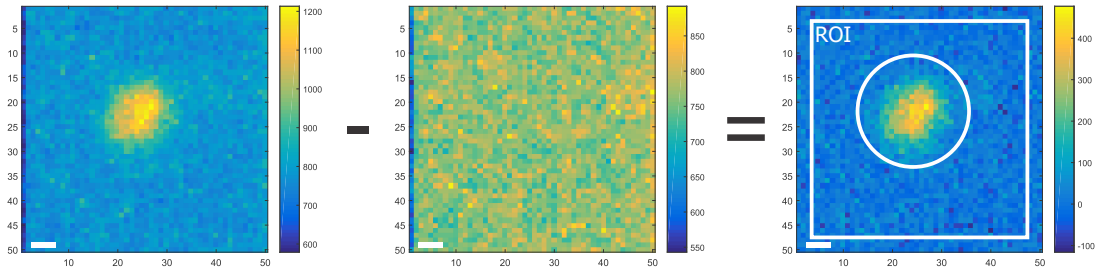

Figure 5.1: On-the-fly image processing. Color bars represent the scale of digital counts within the image. The size of the images is 50 pixels in both directions, while 2×2 binning was used. The white scale bar measures the length of five recorded pixels (i.e. a length of 10 physical pixels on the CCD chip), corresponding to 49.6 μm in the object plane. **left** Example image of a single atom trapped in the d-MOT. **center** Subtracting an initially acquired background image enables to estimate the digital counts due to the fluorescence of atoms within the d-MOT. **right** Only a central region of interest (ROI) is chosen by removing the outer pixels in order to avoid edge artifacts. An additional mask can (white ring) be applied to the resulting image, only selecting the atomic clouds' fluorescence signal. By summing up the counts of the pixels within the mask or even within the ROI the fluorescence signal can be estimated.

they are trapped in the i-MOT. Since the characterization of the d-MOT only requires small numbers of atoms, a loading time of 15 ms suffices. For another 10 ms, all laser lights are turned off to allow for a dilution of the cloud to reduce the initial atom number. Afterwards the d-MOT configuration utilizing the small MOT beams with a diameter of only 1.25 mm is activated to recapture the a small amount of the atoms. Following an initial holding time of 500 ms that absolutely ensures all untrapped atoms have dropped out of the detection region, the fluorescence signal emitted from the atoms trapped in the d-MOT is imaged for $\tau_{\mathrm{exp}} = 90$ ms. This is followed by an additional holding time of 230 ms, during which the camera image is being read out. These last two steps of fluorescence imaging and holding (readout) time are then repeated 10 more times, such that the time from finished exposure to the next finished exposure is 310 ms. One full cycle of the sequence thus delivers one background image and 11 images containing an atomic signal from the d-MOT. Continuously tracking the background signal interleaved with the atomic data, allows to not only observe potential drifts in the light intensity, but also to estimate the drift during the acquisition of the atomic data.

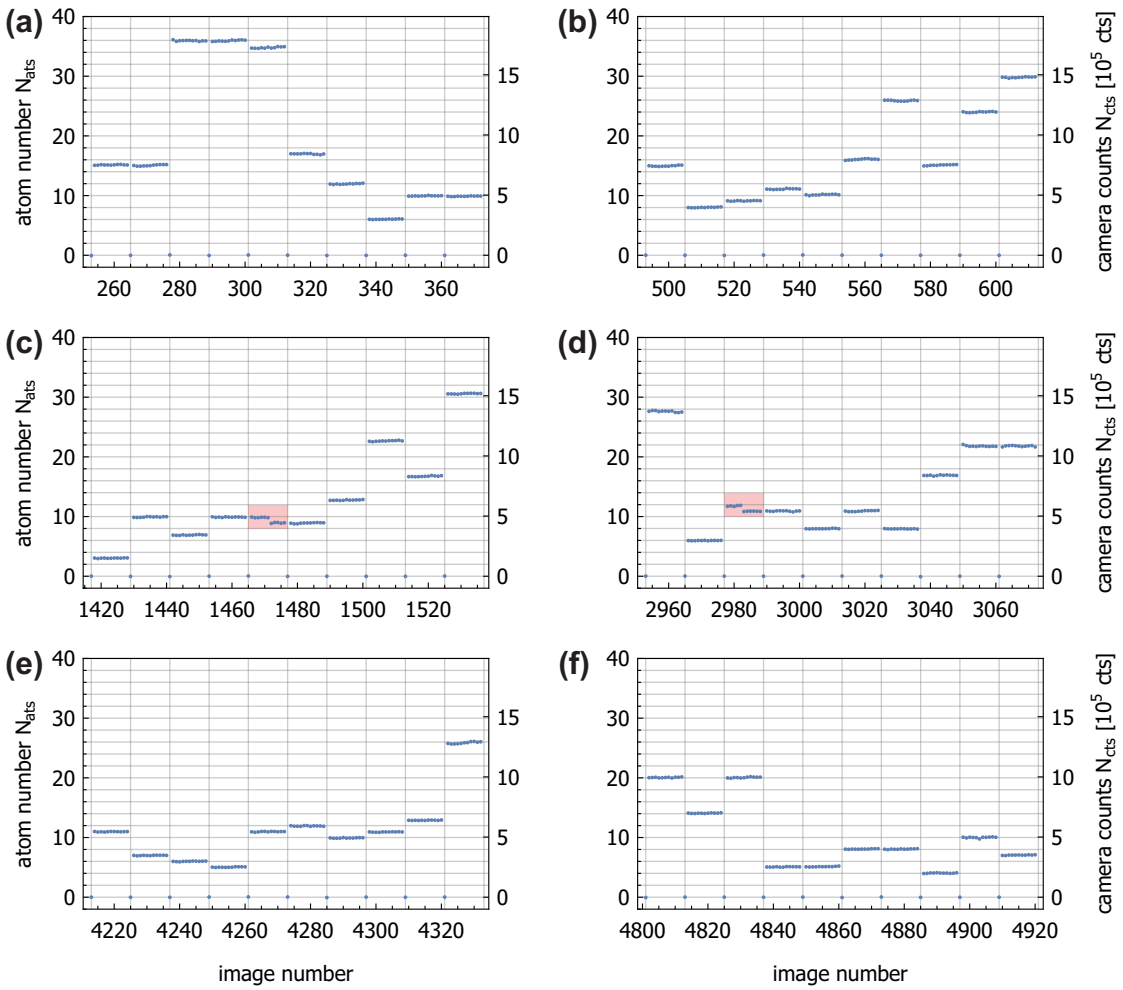

Figure 5.2: Time traces of the experimental sequence. Six graphs show time traces of the fluorescence signal gathered from the d-MOT. Each graph contains 10 full repetitions of the experimental sequence. Each repetition consists of one initial background image, marked by the vertical grid lines in the graphs, followed by 11 images containing fluorescence signal of atoms in the d-MOT. The horizontal axis shows the running image number N_{img}, while the right and left vertical axis measure the signal strength in digital counts N_{cts} and atom number N_{ats}. The calibrated scaling for the atom number is derived in the following section. Exemplary single atom loss events are highlighted with a red shaded background.

5.2 Data analysis

5.2.1 On-the-fly image handling and time traces

The acquired images displaying the acquired camera counts (cts) are handled as shown in Fig. 5.1. Only the minimally necessary region of interest of 100 by 100 physical pixels on the CCD chip is readout to speed up the read out process and data handling. In data processing, the 5 edge pixels are removed to exclude any edge effects from entering the calculations. By binning the pixels in a 2×2 fashion on camera, the readout speed is further increased. While pixel binning also reduces readout noise, the camera in use features a readout noise level of 10.1 cts at the single pixel level that renders it negligible for the presented measurements. Even when summed over the full region of interest of 100×100 physical pixels, the total readout noise contributes only 1000 cts. For pixel binning, this number scales approximately linearly with the binning size, i.e. about 500 cts (250 cts) for 2×2 (4×4) binning with respect to the same region of interest. All images taken during the sequence described in the previous section have a previously acquired base background image subtracted. This is necessary to enable an on-the-fly estimation of the signal strength relative to the background. By summing up the counts of all the pixels within the mask, the total fluorescence signal of the d-MOT is obtained. Typical time traces of the fluorescence signal across many sequences are shown in Fig. 5.2 a-f for a total of 60 experimental realizations in both units of camera counts and converted atom number. The single traces show clear constant atom numbers, where repeated measurements of the same cloud show very reproducible signal — a strong indication of successfully counting single atoms. Visible steps within some time traces are caused by the loss individual atoms due to the finite life time of the trap (Section 5.2.4). These events especially further emphasize the discriminability of two adjacent atom numbers, and hence herald the achievement of true single-atom counting resolution.

5.2.2 Background characterization and correction

The total amount of counts of the background images is comprised of ambient light hitting the camera chip, occurring dark counts, the light background from the cooling laser and additional offset counts per pixel, that get added during the pixel readout procedure. While the former two sources proved negligible in separate experiments, the additional offset counts of 604(11) cts per 2×2 binned pixel are subtracted to retrieve the actual amplitude of the background signal (Fig. 5.3). The evaluation of this background time trace shows that the background performance with a mean signal of 338(3) kcts (i.e. a mean background counting rate of 3.76(3) Mcts/s) is sufficient. Note, that these background levels

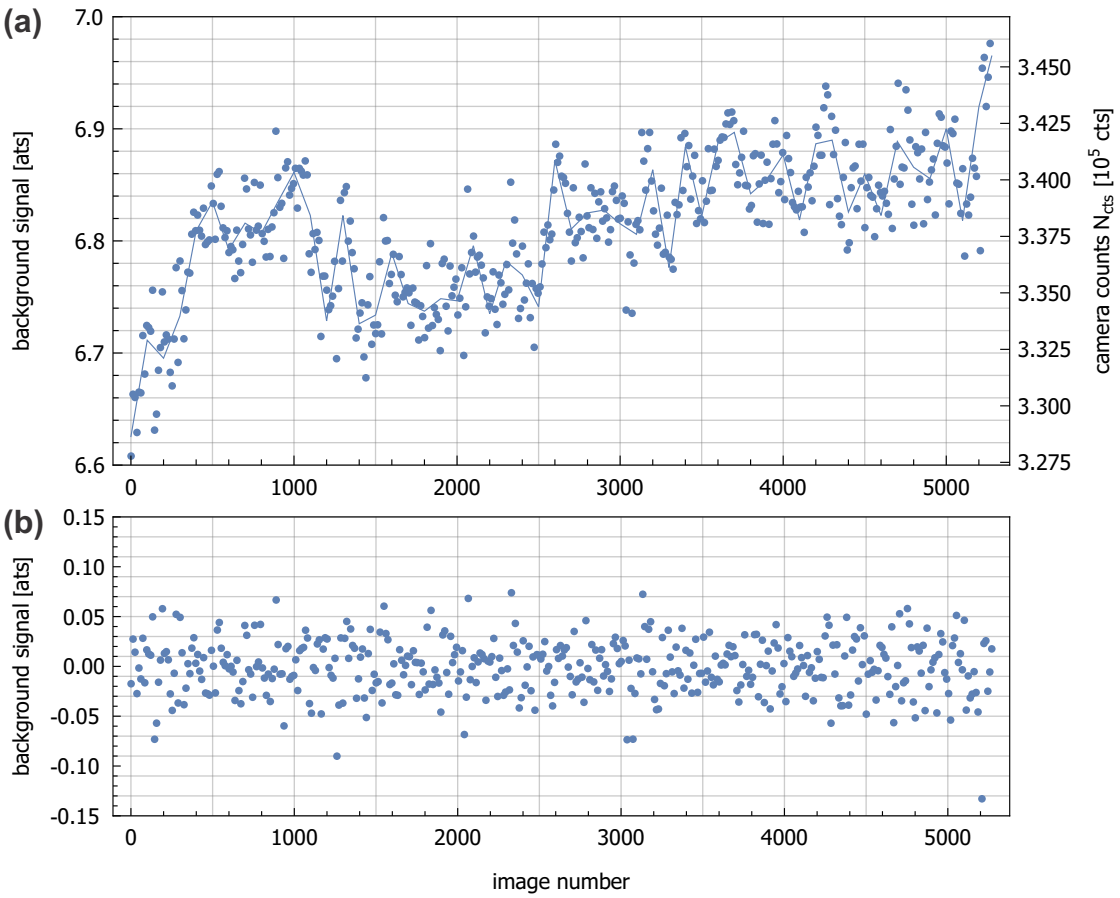

Figure 5.3: Absolute background signal time trace and background correction. **a** The acquired background signal (data points) is shown in units of atoms (left vertical axis) and in units of camera counts (right vertical axis). It exhibits a maximal drift equivalent to 0.5 atoms over the measurement time. This can be partially corrected for by grouping the background images and fitting a piecewise linear function (blue solid line). Here, the first background image is used as a reference. The atomic data has been taken in between the shown background images The corresponding offset corrections are calculated from the fitted function. **b** Correcting the background signal itself by yields a remaining background a standard deviation of about $\sigma_{\mathrm{bkg}} = 3 \times 10^{-2}$ atoms.

are referring to the extracted region of interest of 90×90 physical pixels. This average signal strength offsets the atomic signal by 6.81(6) atoms in the d-MOT. More important than the overall background strength is its very small standard deviation compared to the signal of a single atom. Such a low background noise is a crucial prerequisite in order to be able to operate a detection setup capable of counting atoms accurately. If the background noise would outscale the signal of a single atom no single-atom detection would be possible.

However, a good part of the noise can be attributed to a slight drift in the background signal over the course of the measurement. Using a piecewise linear function that minimizes the squared deviations, a background offset estimation is made that is used to correct the camera counts in the atom images (Fig. 5.3 a). Applying the background correction to the background data itself yields a remaining background standard deviation of $\sigma_{\mathrm{bkg}} = 3 \times 10^{-2}$ atoms (Fig. 5.3 b). This strategy of repeated background calibration is also applicable beyond the presented calibration procedure. When the detection system is used to evaluate atom numbers as the outcome of an experiment, interleaving the acquisition of background images with the experimental sequence is strongly advised.

Beyond the background estimation the background signal can be used to analyze the fluctuations in the cooling intensity in terms of the saturation parameter s_0 and their contribution to the counting noise beyond the background noise. By interpreting the background signal as a measurement of the cooling light intensity stability, the variance of the saturation parameter can be estimated as

$$\sigma_{s_0} = \sqrt{s_0^2 \, \sigma^2_{N_{\mathrm{cts}},\mathrm{bkg}} / \langle N_{\mathrm{cts,bkg}} \rangle^2} = 6 \times 10^{-2}. \tag{5.1}$$

After applying the background correction the corresponding saturation parameter variance becomes $\sigma_{s_0,\mathrm{corr}} = 3 \times 10^{-2}$. The comparison of these two values already hints, that a non-negligible portion of the scattering rate noise is caused by a drift in the intensity stabilization. A probable cause for this can be found in the temperature dependent polarization properties of the optical fibers. This becomes especially important as the imperfect polarization beam splitter that feeds a small part of the cooling light onto the photo diode for the stabilization will reflect a disproportional amount of the polarization drifts.

5.2.3 Atom number detection

The most precise way to determine the atom number in the d-MOT is to extract the signal strength of a single trapped atom experimentally. To this end, a histogram (Fig. 5.4) of the acquired camera counts across all images is build up, after the background signal has been subtracted. As the main result of this work, the histogram reveals the formation of distinct equidistant peaks. Here, the first peak corresponds to the corrected background data. The second peak is the signal of a single atom trapped in the d-MOT and each further peak corresponds to the addition of another atom to the trap.

To determine the center position of the peaks, the first 20 peaks of the histogram are selected. Peaks belonging to higher atom numbers are neglected in this

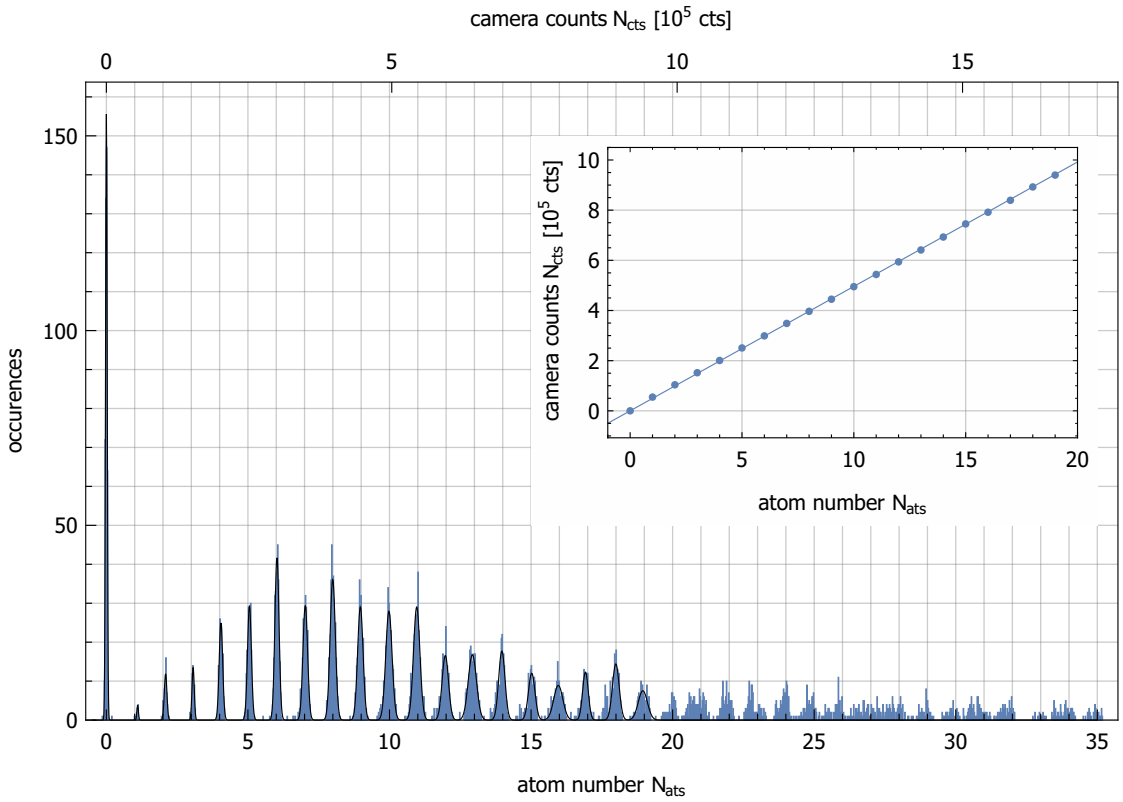

Figure 5.4: Atom signal histogram and atom scaling calibration (inset). The histogram shows the collected atomic signal on the horizontal axis units of atoms after calibration (bottom) and in units of camera counts after offset subtraction (top) with a bin size of about 1280 cts or 0.026 atoms. Clearly distinguishable peaks correspond to different integer atom numbers. A sum of Gaussian distributions is used as a modeling function (black line) for the first 20 peaks including the background peak. **Inset** The resulting center positions of the Gaussian fits are fitted linearly against the integer peak number yielding a linear scaling factor $n_{\mathrm{cts}} = 49.60(9)$ kcts/atom that gauges the ratio of camera counts per atom. The error bars are smaller than the symbol size.

procedure due to the limited size of contributing data points. A simultaneous fit of a sum of Gaussian distributions

$$f_{\mathrm{hist}}(\tilde{N}_{\mathrm{ats}}) = \sum_{j=0}^{19} h_j \exp\left(-\frac{\left(\tilde{N}_{\mathrm{ats}} - \langle \tilde{N}_{\mathrm{ats}} \rangle_j\right)^2}{2\sigma_j^2}\right) \tag{5.2}$$

with a set of three free parameters for each peak is performed. The result yields the corresponding center positions $\langle \tilde{N}_{\mathrm{ats}} \rangle_j$, widths σ_j and heights h_j of the peaks. Plotting the fitted center positions against the corresponding atom number, i.e. the integer position of the peak counting from the background peak, shows a

linear relation (Fig. 5.4 inset). To obtain a scaling factor[16], a linear function[17] is fitted yielding a slope value of

$$n_{\mathrm{cts}} = 49.60(9)\,\mathrm{kcts/atom}. \tag{5.3}$$

This calibrated scaling factor is the key parameter of the presented accurate atom counting detection. A precise determination of the signal of individual atoms is only possible due to the sufficiently low detection noise, reflected in the well resolved peaks and their corresponding width.

The most general way to express the found scaling for the atom number is by correcting it for the exposure time, yielding a counting rate that describes the camera counts generated per atom captured in the d-MOT and per second of camera exposure:

$$r_{\mathrm{cts}} = \frac{n_{\mathrm{cts}}}{\tau_{\mathrm{exp}}} = 551.1(9)\,\mathrm{kts/(s\,atom)}. \tag{5.4}$$

This very high single atom counting rate is a result of the careful design of all relevant parts of the d-MOT detection scheme and will enable scaling the accurate atom detection to higher mesoscopic atom numbers.

The experimental sequence parameters, i.e. detuning of the cooling light $\Delta = 6\,\mathrm{MHz}$ and the saturation parameter $s_0 = 6.65$, allow to estimate the expected scattering rate of the atoms within the d-MOT according to equation 3.1 as

$$R_{\mathrm{sc}}^{\mathrm{expected}}(\Delta, s_0) \approx 1.096 \times 10^7\,\mathrm{photons/s}. \tag{5.5}$$

Based on the design parameters of the d-MOT detection setup, an effective conversion factor of photons originating isotropically in the focus of the detection system to digital camera counts[18] is calculated $\tilde{\eta}_{\mathrm{det}} = 4.33\,\%$. The expected camera counts per atom per second can be estimated

$$r_{\mathrm{cts}}^{\mathrm{expected}} = \tilde{\eta}_{\mathrm{det}}\, R_{\mathrm{sc}}(\Delta, s_0) \approx 474\,\mathrm{kcts/(s\,atom)}. \tag{5.6}$$

During the exposure time of $\tau_{\mathrm{exp}} = 90\,\mathrm{ms}$ a total of

$$n_{\mathrm{cts}}^{\mathrm{expected}} = r_{\mathrm{cts}}^{\mathrm{expected}} * \tau_{\mathrm{exp}} = 43\,\mathrm{kcts/atom} \tag{5.7}$$

[16] This quantity by nature is unit-less as it gives the value of digital camera counts generated per atom in the d-MOT. But in order to maintain readability with all the different amounts of photons, counts and atoms within the detection scheme, an explicit notation seems appropriate.

[17] Quadratic contributions proved to be negligible. This justifies the intrinsically made assumption, that no non-linearity, for example by reabsorption of fluorescence photons, has to be considered for the presented atom numbers.

[18] This conversion factor already takes into account the measured gain $g = 1.089(4)$ of the camera model.

are expected.

The calibrated scaling factor n_{cts} (Eqn. 5.3) differs from the expected value $n_{\text{cts}}^{\text{expected}}$ calculated above. Errors may be found in the assumptions made about the detection system alignment that was based on the designed values and not measured after optimizing its focus on the atomic position.

The presented accurate atom counting detection can be considered self-calibrating, as it does not rely on any external value or a priori knowledge to identify a single atom unambiguously. An initial estimation of the single-atom signal served as a means to run the experiment in the correct regime and ensure the sampling on the single-atom scale. Once all designed parameters and experimental parameters are controlled well enough to obtain a reasonable estimate for the signal of an individual atom, the experimental data itself provides the best scale.[19] This is a huge advantage when compared to typical fluorescence or absorption detection setups, that cannot provide a natural, experimentally extractable scale for the atom number and rather have to rely on a priori knowledge or multiple measurements of all involved experimental parameters, each further being another potential source of inaccuracy.

5.2.4 Life time and loading rate analysis

For optimal performance of the accurate atom counting detection the knowledge of the d-MOT life time τ_{life} is inevitable, as the ideal exposure time $\tau_{\text{exp,opt}}$ depends on it (Chapter 3.2). Utilizing the occurrence of loss events during the experimental repetitions while holding the atoms in the d-MOT, the life time of the d-MOT can be evaluated. In a Poissonian loss process, loss events are independent and during a sufficiently small time interval $[t, t + \Delta t]$ only one loss process is assumed to occur. This assumption holds true, as long as the time interval is small compared to the characteristic time scale τ_{life}, i.e. the life time, of the process. Further, the probability p_1 for a single loss event to happen during a time interval of length Δt scales linearly with the length of the time interval, s.t.

$$p_1(\Delta t) = g\Delta t. \tag{5.8}$$

Consequently, the probability p_0 for no loss event to take place is given by

$$p_0(\Delta t) = 1 - p_1(\Delta t) = 1 - g\Delta t. \tag{5.9}$$

[19] Of course this is somewhat a double-edged sword as the knowledge of the constituents to the scaling factor is crucial to both designing the experimental setup and future improvements concerning the systems noise.

Hence, the probability for no loss event to have happened until the time $t + \Delta t$ can be expressed as

$$p_0(t + \Delta t) = p_0(t)\, p_0(\Delta t) = p_0(t) - p_0(t)\, g\Delta t \tag{5.10}$$

leading to the differential equation

$$\frac{\mathrm{d}p_0(t)}{\mathrm{d}t} = -g p_0(t) \tag{5.11}$$

that is solved by using an exponential ansatz under the condition that $p_0(t = 0) = 1$. Therefore, the solution reads

$$p_0(t) = \exp(-gt) = \exp\left(-\frac{t}{\tau_{\mathrm{life}}}\right). \tag{5.12}$$

Thus, the life time τ_{life} is given as the inverse of the linear scaling factor

$$\tau_{\mathrm{life}} = g^{-1} = \frac{\Delta t}{p_1(\Delta t)}. \tag{5.13}$$

The probability $p_1(\Delta t)$ of a loss event to happen during the experimental sequence spanning the time interval $\Delta t = 310\,\mathrm{ms}$ can be evaluated by counting the steps in the fluorescence time traces. This is performed by pairing up atom numbers from consecutive images within the sequence runs. The first in the pair determines the atom number $N_{\mathrm{ats}}^{\mathrm{pre}}$ before the time step Δt by rounding it to the nearest integer. This is used to group the paired data according to the atom number in the first image. The second image determines the atom number N_{ats} after the time step. Depending on a loss or possibly a loading event this atom number might have changed or not. Figure 5.5 shows histograms of the resulting atom numbers after the time step for fifteen initial atom numbers from $N_{\mathrm{ats}}^{\mathrm{pre}} = 1$ to $N_{\mathrm{ats}}^{\mathrm{pre}} = 15$. Losses of more than one atom during a time step are not present in the statistics, underlining the initial assumption of maximally one loss event during the time window Δt and justifying the negligence of higher order loss events. The histograms show that single-atom loss events and loading events are rare, as the time traces in Fig. 5.2 suggested. The most common case appears to be an unchanged atom number, depicted by the strong peak in the center of each histogram. Approaching this analysis by treating each time step as an independent experiment with one of three possible outcomes, i.e. loss, survival and loading, allows to quantify the characteristics of the loading and loss process. Hence, the number of times an event occurs are called $M_{j,\mathrm{loss}}$, $M_{j,\mathrm{surv}}$ and $M_{j,\mathrm{load}}$. These numbers can be extracted from each histogram in Fig. 5.5, where the index j refers to the corresponding initial atom number $N_{\mathrm{ats}}^{\mathrm{pre}}$. By suppressing the index dependence on j in

$$M_k = \sum_{j=1}^{15} M_{j,k} \qquad k = \mathrm{loss}, \mathrm{surv}, \mathrm{load}\,, \tag{5.14}$$

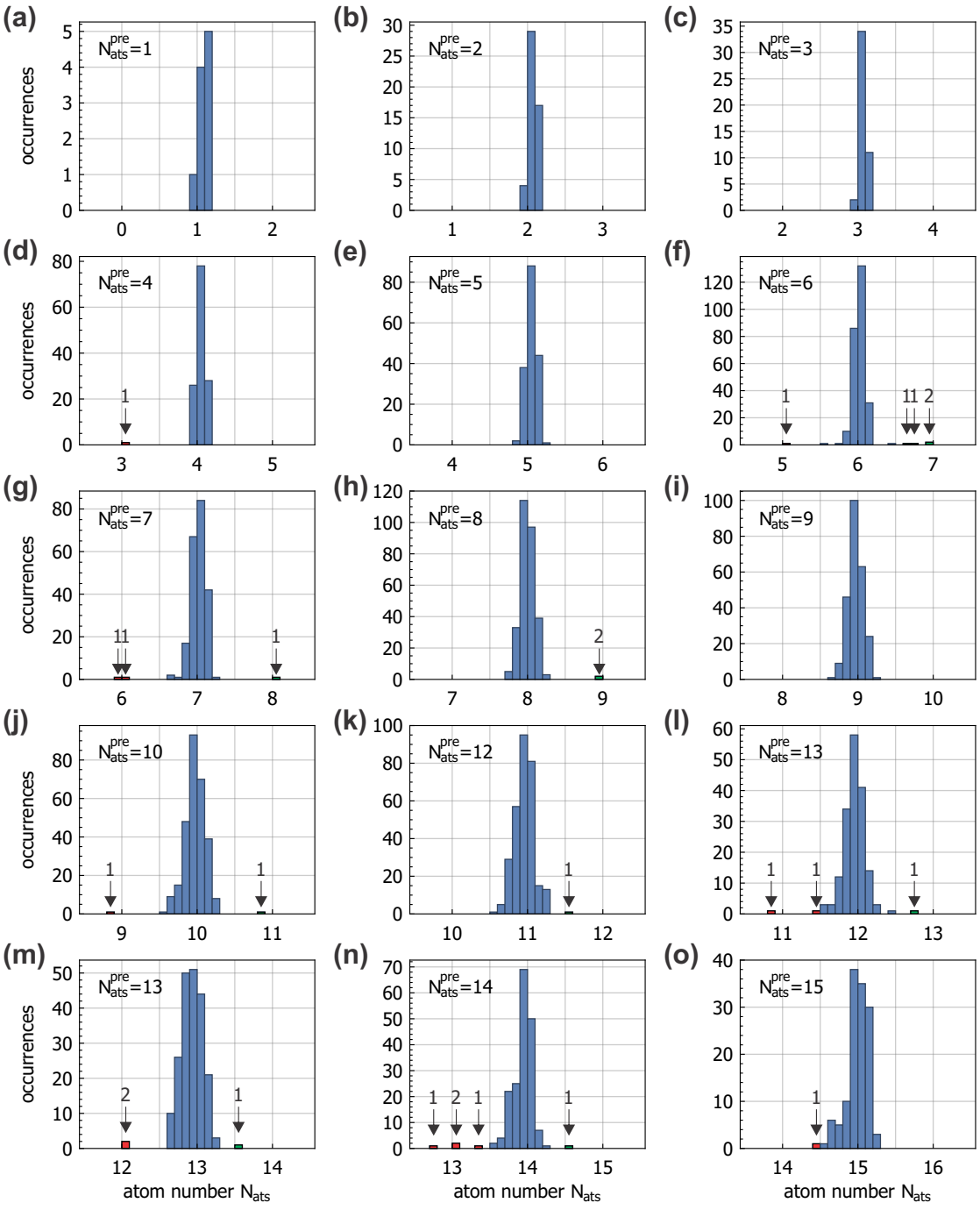

Figure 5.5: Histograms of single-atom loss and loading events. The histograms show the measured atom number N_{ats} depending on the atom number $N_{\mathrm{ats}}^{\mathrm{pre}}$ measured in the previous time step. Data for atom numbers from $N_{\mathrm{ats}}^{\mathrm{pre}} = 1$ to $N_{\mathrm{ats}}^{\mathrm{pre}} = 15$ is considered in the histograms **a-o**, respectively. Possible loss and loading events are highlighted in red and green, respectively. The blue contributions are considered survival events.

event	occurences M^{event}	M^{attempts}	result
single-atom loading	12	2710	$R_{\text{load}} = 0.014(4)\,\text{s}^{-1}$
single-atom loss	14	24482	$\tau_{\text{life}} = 540(150)\,\text{s}$

Table 5.1: Life time and loading rate analysis. This table sums up the statistics and the results of the time step analysis from the time traces of the atomic signal from the d-MOT.

these quantities are considered the respective sums across all values of $N_{\text{ats}}^{\text{prev}}$. The loading probability of the d-MOT configuration is determined by comparing M_{load} to the count of all single time step experiments where a loading event could have possibly occurred:

$$p_{\text{load}} = \frac{M_{\text{load}}}{M_{\text{loss}} + M_{\text{surv}} + M_{\text{load}}}. \tag{5.15}$$

Dividing this loading probability by the time step of the experimental sequence allows to extract the loading rate $R_{\text{load}} = p_{\text{load}}/\Delta t \approx 0.014(4)\,\text{s}^{-1}$. The low loading rate can be explained by the combination of small cooling beams used in the d-MOT configuration, leading to a lower capture velocity, and low background pressure in the science cell.

To calculate the loss probability the number of loss events M_{loss} is compared to the number of experiments that could have exhibited a loss event. This time not only all time steps need to be considered as independent experiments, but also each atom captured in the d-MOT that undergoes a time step is regarded an individual loss test. The is considered by appropriately scaling the number of survival events with the atom number $N_{\text{ats}}^{\text{prev}}$ present in the trap:

$$p_{\text{loss}} = \frac{M_{\text{loss}}}{M_{\text{loss}} + \sum_{j=1}^{15} jM_{j,\text{surv}} + M_{\text{load}}}. \tag{5.16}$$

According to Eq. 5.13 the life time is given by $\tau_{\text{life}} = \Delta t/p_{\text{loss}} \approx 540(150)\,\text{s}$. While life times in magneto-optical traps can reach values up to 200 s [43], the presented d-MOT system exhibits an exceptional life time performance. While the pressure in the science chamber is not measurable directly, this long life time can very well be interpreted as the result of a low background pressure enabled by the double differential pumping scheme in the vacuum setup. The results are summed up in Tab. 5.1.

5.2.5 Noise analysis

The fitted Gaussian distributions from Fig. 5.4 d yield not only the positions of the respective peaks belonging to integer atom numbers, but also their widths. These widths and the corresponding variances are a measure for the detection noise with the caveat, that they are largely made up out of long term drifts of the cooling intensity and frequency that accumulated during the extend of the measurement. Additionally, the results of a mathematical fit that is based on a least squares method, may not accurately reflect the statistical properties of the underlying sample. But turning to the use of the statistical variance of the distinct distributions in the histogram in Fig. 5.4 still will lead to a drift dominated noise description. The goal here is to characterize the typical fluctuations that occur during a single experimental realization of the detection scheme. These shot-to-shot deviations are aptly described by the two-sample variance:

$$\sigma^2_{N_{\mathrm{ats}}} = \frac{1}{2}\left\langle \left(N_{j+1,\mathrm{ats}} - N_{j,\mathrm{ats}}\right)^2 \right\rangle_j . \tag{5.17}$$

There are two main benefits to this approach. Firstly, it allows to include data from atom numbers where the statistical sample is too small to fit a full Gaussian function. Secondly, long term drifts in the scattering rate due to intensity or frequency drifts do not affect this quantity. It rather captures the short behavior of the intensity and frequency fluctuations. In fact the simple noise model from Equation 3.2 only includes contributions from the photon shot noise as of the atomic sample as σ^2_{psn} and single-atom losses due to a finite trapping life time as σ^2_{loss}. A more general noise model additionally includes the background noise, the scattering rate noise and even two-body losses due to light-assisted collisions as a higher order loss process:

$$\sigma^2_{N_{\mathrm{ats}}} = \sigma^2_{\mathrm{bkg}} + \sigma^2_{\mathrm{psn}} + \sigma^2_{\mathrm{srn}} + \sigma^2_{\mathrm{loss}} , \tag{5.18}$$

where σ^2_{bkg} is an additional offset variance from the background signal that is independent of atom number and σ^2_{srn} captures the scattering rate noise. According to section 5.2.2 the background noise after application of the background correction is estimated to be $\sigma^2_{\mathrm{bkg}} = 8.4 \times 10^{-4}$.

Photon shot noise and scattering rate fluctuations

Contributions from the photon shot noise and scattering rate fluctuations induced by frequency and intensity noise are best understood by reviewing how the camera counts emerge from the fluorescence signal. The number of detected fluorescence photons is on the order of a few 10^4 photons per atom. For a fixed number of atoms N_{ats}, the detected photons can be assumed to follow a Gaussian distribution with a mean value of $\langle N_{\mathrm{cts}} \rangle = N_{\mathrm{ats}}\, \tilde{\eta}\, \tau_{\mathrm{exp}}\, R_{\mathrm{sc}}\,(\Delta, s_0)$. The variance is

determined by contributions from photo-electron shot noise and scattering rate noise:

$$\begin{aligned}\sigma^2_{N_{\mathrm{cts}}} &= \sigma^2_{N_{\mathrm{cts}},\mathrm{psn}} + \sigma^2_{N_{\mathrm{cts}},\mathrm{srn}} \\ &= \langle N_{\mathrm{cts}}\rangle / g + \left(\sigma^2_{\Delta}\,(\partial_{\Delta} R_{\mathrm{sc}})^2 + \sigma^2_{s_0}\,(\partial_{s_0} R_{\mathrm{sc}})^2\right) N^2_{\mathrm{ats}} \tilde{\eta}^2 \tau^2_{\mathrm{exp}}\,,\end{aligned} \tag{5.19}$$

where the symbol ∂_j denotes a partial derivative with respect to the variable j. Dividing the variance of the camera counts by $(\tilde{\eta}\,\tau_{\mathrm{exp}}\,R_{\mathrm{sc}})^2$ reveals the corresponding contribution to the atom counting variance to be

$$\begin{aligned}\sigma^2_{N_{\mathrm{ats}}} &= \frac{N_{\mathrm{ats}}}{\eta\,\tau_{\mathrm{exp}}\,R_{\mathrm{sc}}} + N^2_{\mathrm{ats}}\left(\left(\frac{\sigma_{\Delta}}{R_{\mathrm{sc}}}\partial_{\Delta} R_{\mathrm{sc}}\right)^2 + \left(\frac{\sigma_{s_0}}{R_{\mathrm{sc}}}\partial_{s_0} R_{\mathrm{sc}}\right)^2\right) \\ &= \sigma^2_{\mathrm{psn}} + \sigma^2_{\mathrm{srn}}.\end{aligned} \tag{5.20}$$

Noteworthy are the different dependencies on the atom number for these noise contributions. While photon shot noise depends linearly on the atom number, scattering rate noise scales with the square of the atom number. This kind of dependence reflects that the scattering rate noise is correlated for all the atoms, i.e. they all experience the same scattering rate noise. In the histogram picture a fluctuation in the scattering rate changes the distance between the different peaks, which scales linearly with their distance from the origin. On average this increases a peak's width linearly with the corresponding atom number and in turn the variance will exhibit a quadratic dependence for this process. The scattering rate noise can be summed up using a common parameter

$$\alpha^2 = \tau_{\mathrm{exp}}\left(\left(\frac{\sigma_{\Delta}}{R_{\mathrm{sc}}}\partial_{\Delta} R_{\mathrm{sc}}\right)^2 + \left(\frac{\sigma_{s_0}}{R_{\mathrm{sc}}}\partial_{s_0} R_{\mathrm{sc}}\right)^2\right) \tag{5.21}$$

such that the scattering rate noise term finally reads

$$\sigma^2_{\mathrm{srn}} = \frac{\alpha^2}{\tau_{\mathrm{exp}}} N^2_{\mathrm{ats}}, \tag{5.22}$$

while the photon shot noise contribution can be written as

$$\sigma^2_{\mathrm{psn}} = \frac{N_{\mathrm{ats}}}{\eta\,\tau_{\mathrm{exp}}\,R_{\mathrm{sc}}}. \tag{5.23}$$

For the scattering rate noise, the inverse scaling with the exposure time reflects that for longer exposures, the influence of scattering rate noise is reduced due to the increased averaging time. In the last line of Equation 5.20, this dependence is hidden in the variances of frequency detuning Δ and saturation parameters s_0 as they must be considered in reference to a certain averaging timescale.

Atom loss noise

In case of the two-sample variance, the noise stemming from loss events, both single-atom loss and two-body loss, can be derived using a master-equation approach [43, 209][20] and read

$$\sigma^2_{\text{loss}} = \frac{N_{\text{ats}}\tau_{\text{exp}}}{2\tau_{\text{life}}} + \beta N^2_{\text{ats}}\tau_{\text{exp}} + \frac{1}{2}\left(\frac{N_{\text{ats}}}{\tau_{\text{life}}} + \beta N^2_{\text{ats}}\right)^2 \tau^2_{\text{exp}}, \tag{5.24}$$

where β describes the two-body loss rate.

Table 5.2 gives an overview of the expected contributions from all considered noise sources in Equations 5.22, 5.23 and 5.24 for the data presented in an effort to reduce the amount of terms to consider. From low atom numbers on, the scattering rate term is expected to largely contribute to the noise. Only for atom numbers as high as 10^5 orders higher than the quadratic order in N_{ats} are expected to match the scattering rate contribution. Atom numbers this high are outside of the range of atom numbers that are detectable accurately. Lastly, for the presented data it suffices to truncate the noise model at the second order, only including the scattering rate term and disregarding loss related terms of higher orders in N_{ats}. With this the reduced noise model reads

$$\begin{aligned}
\sigma^2_{N_{\text{ats}}} &= \sigma^2_{\text{bkg}} + \sigma^2_{\text{psn}} + \sigma^2_{\text{srn}} + \sigma^2_{\text{loss}} \\
&= \sigma^2_{\text{bkg}} + \frac{N_{\text{ats}}}{\eta\,\tau_{\text{exp}}\,R_{\text{sc}}} + \frac{\alpha^2 N^2_{\text{ats}}}{\tau_{\text{exp}}} + \frac{N_{\text{ats}}\tau_{\text{exp}}}{2\tau_{\text{life}}} \\
&= \sigma^2_{\text{bkg}} + N_{\text{ats}}\left(\frac{1}{\eta\,\tau_{\text{exp}}\,R_{\text{sc}}} + \frac{\tau_{\text{exp}}}{2\tau_{\text{life}}}\right) + N^2_{\text{ats}}\,\frac{\alpha^2}{\tau_{\text{exp}}}
\end{aligned} \tag{5.25}$$

Before this noise model can be applied to the two-sample variance of the experimental data, the influence of the loss contribution needs to be considered carefully. An atom getting lost during the exposure will only contribute a fraction of the expected fluorescence signal, depending on at which exact point in time during the exposure it left the trap. Section 5.2.4 showed that only very few loss events are present within the complete dataset. This means that not even at every atom number a loss event has occurred. As a consequence, the loss contribution to the two-sample variance will only affect certain atom atom numbers. Additionally, the experimental sequence (Section 5.1) features a dead time between the images to allow for the image readout. This dead time of $\tau_{\text{dead}} = 220\,\text{ms}$ gives each atom an additional probability to leave the trap proportional to the duration of the dead time. Thus, an atom is about two times more

[20] The inclined reader might find interest in the lengthy derivation presented in [209].

order	coefficient	value	source
—	σ^2_{bkg}	8×10^{-4}	background noise
N_{ats}	$(\eta\, R_{\mathrm{sc}} \tau_{\mathrm{exp}})^{-1}$	2×10^{-5}	photon shot noise
	$\tau_{\mathrm{exp}}/(2\,\tau_{\mathrm{life}})$	8×10^{-5}	single-atom loss
N^2_{ats}	$\alpha^2/\tau_{\mathrm{exp}}$	4×10^{-5}	scattering rate noise
	$\beta\tau_{\mathrm{exp}}$	3×10^{-8}	two-body loss
	$\tau^2_{\mathrm{exp}}/(2\,\tau^2_{\mathrm{life}})$	1×10^{-8}	mean atom loss
N^3_{ats}	$\beta\tau^2_{\mathrm{exp}}/\tau_{\mathrm{life}}$	4×10^{-12}	mean atom loss
N^4_{ats}	$\beta^2\tau^2_{\mathrm{exp}}/2$	4×10^{-16}	mean atom loss

Table 5.2: Noise model terms and their expected contributions. Different contributions for the noise model are estimated using the values $\tau_{\mathrm{life}} = 540(150)$ s, $\alpha = 1{\times}10^{-3}\ \mathrm{s}^{1/2}$ (derived from $\sigma_{s_0} = 6{\times}10^{-2}$, negelecting the presence of frequency noise σ^2_Δ in Equation 5.21) that were obtained in the life time and background analysis sections of this chapter, respectively. Since no two-body loss events are present in the statistics the two-body loss rate is assumed to be $\beta = 3 \times 10^{-7}\ \mathrm{s}^{-1}$ [43].

likely to get lost off camera, than on camera. For this reason the experimental sequence detects full steps in the signal with increased probability, rather than the expected uniform distribution of expected fractional signals from an atom leaving the trap at a random time during the exposure. This would lead to an overrepresentation of loss induced noise for those atom numbers where losses occurred and a simultaneous underrepresentation for atom numbers where no loss was detected. Thus, the two-sample variance is only considered for the data set excluding detected loss events. While this removes the full steps, where the loss occurred during the dead time, it leaves those events where the atom got lost during the first half of the exposure unaffected[21]. By estimating the atom loss noise contribution based on the exposure and life time values (Table 5.2) and adding this back onto the two-sample variance, it is ensured that despite the exclusion of the loss events, the loss contribution to the noise is at best overestimated and evened out across all detected atom numbers.

Also the photon shot noise can be derived from the inverse of the calibrated

[21] These losses are identified as losses on the next image, when the signal crosses the halfway mark between integer atom numbers

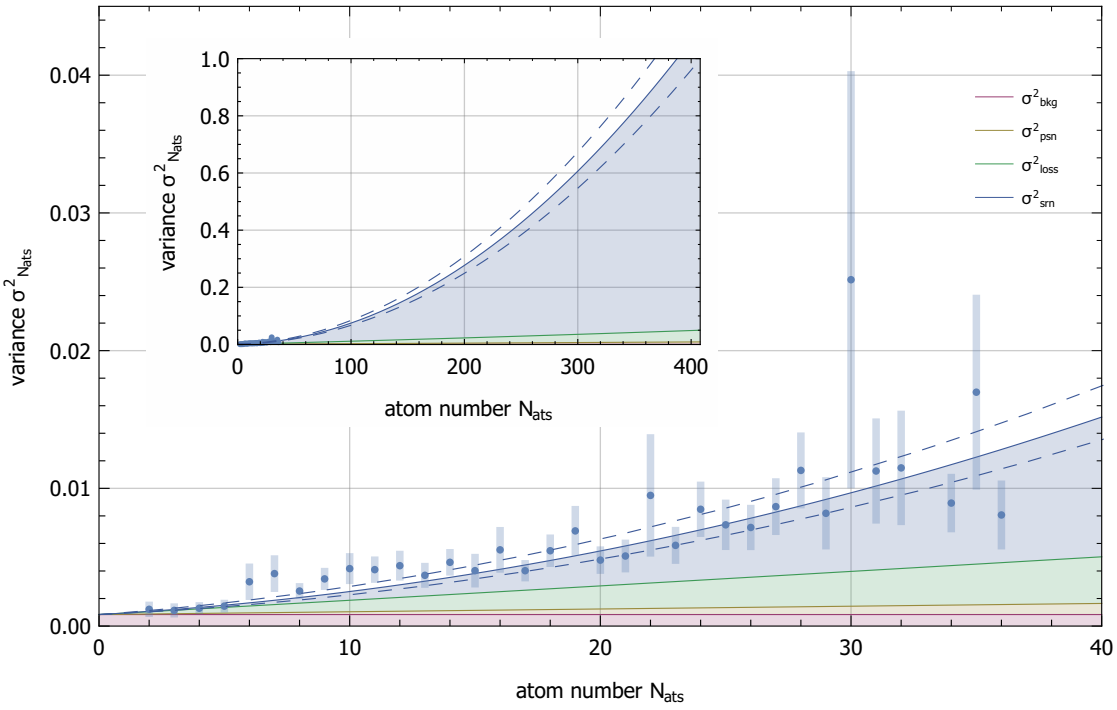

Figure 5.6: Two-point variance and noise model extrapolation. The two-point variance for atom numbers up to $N_{\mathrm{ats}} = 38$ was calculated and fitted with the noise model from Equation 5.25 only using the scattering rate parameter $\alpha = 7.6(4) \times 10^{-4}\,\mathrm{s}^{1/2}$ as a free parameter. Already for small atom numbers the scattering rate noise is the dominant noise contribution. Error bars show the one standard deviation interval. The blue dashed lines outline the model's error band in terms of one standard deviation of the fit parameter α. **Inset** The model can be extrapolated up to the limiting atom number $N_{\mathrm{lim,ats}} = 390(20)$ where $\sigma^2_{N_{\mathrm{ats}}} = 1$, beyond which no accurate atom detection is possible for the chosen exposure time of 90 ms. Only data points with at least 20 counting events are considered.

single-atom signal from Section 5.2.3. The scattering rate noise term includes the most unknown factors as the estimation in Table 5.2 neglects additional noise in the detuning of the cooling light. Using the fluorescence noise parameter as the only free parameter when fitting the noise model from Equation 5.25 to the two-point variance of the atomic signal, a value of $\alpha = 7.6(4) \times 10^{-4}\,\mathrm{s}^{1/2}$ is obtained (Fig. 5.6). From Equation 5.21, the standard deviation of the cooling light detuning[22] $\sigma_\Delta = 15.6$ kHz can be inferred when applying the drift corrected saturation parameter uncertainty.

[22]This frequency fluctuation is calculated from the two-sample variance. Thus, it does not include any long term drifts with respect to the imaging time.

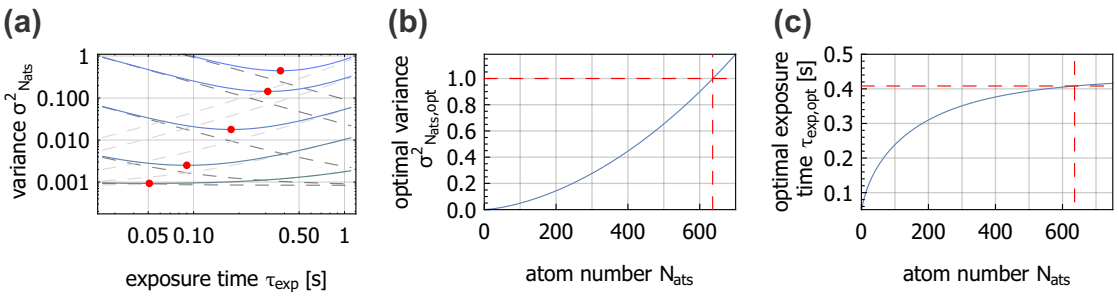

Figure 5.7: Exposure time optimization. **a** Exposure time dependence of the atom number variance for different atom numbers: 1 –, 10 –, 50 –, 200 – and 400 –. The red points mark the position of minimal variance for the respective atom numbers. The dashed lines show the limiting contributions of scattering rate and photon shot noise for short timescales (dark gray) and atom loss contributions for longer time scales (light grad). **b** The highest detectable atom number $N_{\mathrm{ats,maxlim}} = 640$ with a variance below unity is found by optimizing the exposure time to $\tau_{\mathrm{exp,maxlim}} = 408\,\mathrm{ms}$ to best accommodate to the specific noise environment. This does not consider that the dynamic range of the camera pixels is finite and hence for the current choice of magnification and binning **c** The optimal exposure time changes with atom number as the long life time allows to compensate for the scattering rate noise that grows quadratically with the atom number. Nevertheless with increasing atom number the optimal exposure time seems to saturate, but only around the point where the fluctuations inhibit accurate atom counting.

Beyond this, the noise model can be used to extrapolate the atom counting performance towards higher atom numbers, finally reaching the accurate atom detection threshold $\sigma^2_{N_{\mathrm{ats}}} = 1$ for $N_{\mathrm{ats}} = 390(20)$ atoms (Fig. 5.6 inset). Note, that this accurate counting limit depends on the exposure time τ_{exp} applied when taking the data. The known contributions from the different noise sources can be utilized to estimate an optimal exposure time $\tau_{\mathrm{opt,exp}}$ for every atom number. Revisiting the noise model in Equation 5.25, it becomes clear that scattering rate and photon shot noise will reduce with increasing exposure time. However, life time driven atom loss will at some point dominate the fluctuations. Figure 5.7 a shows the dependence of the atom detection variance on the exposure time for different atom numbers. Due to the strong scattering rate noise, the optimal exposure time shifts towards longer times for increasing atom numbers. For the presented data with an exposure time of $\tau_{\mathrm{exp}} = 90\,\mathrm{ms}$ the average atom number $\langle N_{\mathrm{ats}} \rangle \approx 15$ shows a variance of $\sigma^2_{N_{\mathrm{ats}}}(N_{\mathrm{ats}} = 15) = 0.004(1)$. Compared to the ideal exposure time of $\tau_{\mathrm{exp,opt}} = 106\,\mathrm{ms}$ for 15 atoms with minimal fluctuations of $\sigma^2_{N_{\mathrm{ats}},\mathrm{opt}}(N_{\mathrm{ats}} = 15) = 0.004$ our measured result aligns very well and justifies

the chosen exposure time in retrospect.

From the model, an ultimate limit with respect to the current noise performance of the system can be derived by solving for the maximum atom number $N_{\mathrm{ats,maxlim}}$ at which the ideal exposure time still allows for detection fluctuations below the single-atom detection threshold. At $N_{\mathrm{ats,maxlim}} = 640$ for an ideal exposure time of $\tau_{\mathrm{exp,maxlim}} = 408\,\mathrm{ms}$, even the minimal detection fluctuations reach unity (Fig. 5.7 b and c). In order to realize this in the current setup without being stopped by the saturation of the camera, the binning and also the magnification may need to be adapted to accommodate for the increased single-atom signal.

5.2.6 Scale factor optimization

Building on the insight that scattering rate noise in the form of long term drifts and short term fluctuations contributes most of the noise to the atom counting signal, a reevaluation of the data that incorporates a varying scale factor is justified. The atom counting data for less than 15 atoms from the histogram in Fig. 5.4 split into a set of 100 consecutive groups. For each group a linearly changing scale factor that minimizes the squared distance to integer atom numbers is found (inset of Fig. 5.8 a). Applying this scale factor changes the shape of the individual peaks in the histogram and the peaks experience a reduction in width. Especially noteworthy are the improvements for the data beyond $N_{\mathrm{ats}} = 15$ atoms. This shows that the scale factor optimization successfully used a smaller part of the data to infer on the scattering rate drift of the whole sample. Most interestingly, at the position for $N_{\mathrm{ats}} = 27$ a peak becomes visible (Fig. 5.8 b and c). This result underlines the observations made during the noise analysis, that scattering rate noise is the currently limiting noise source in the system.

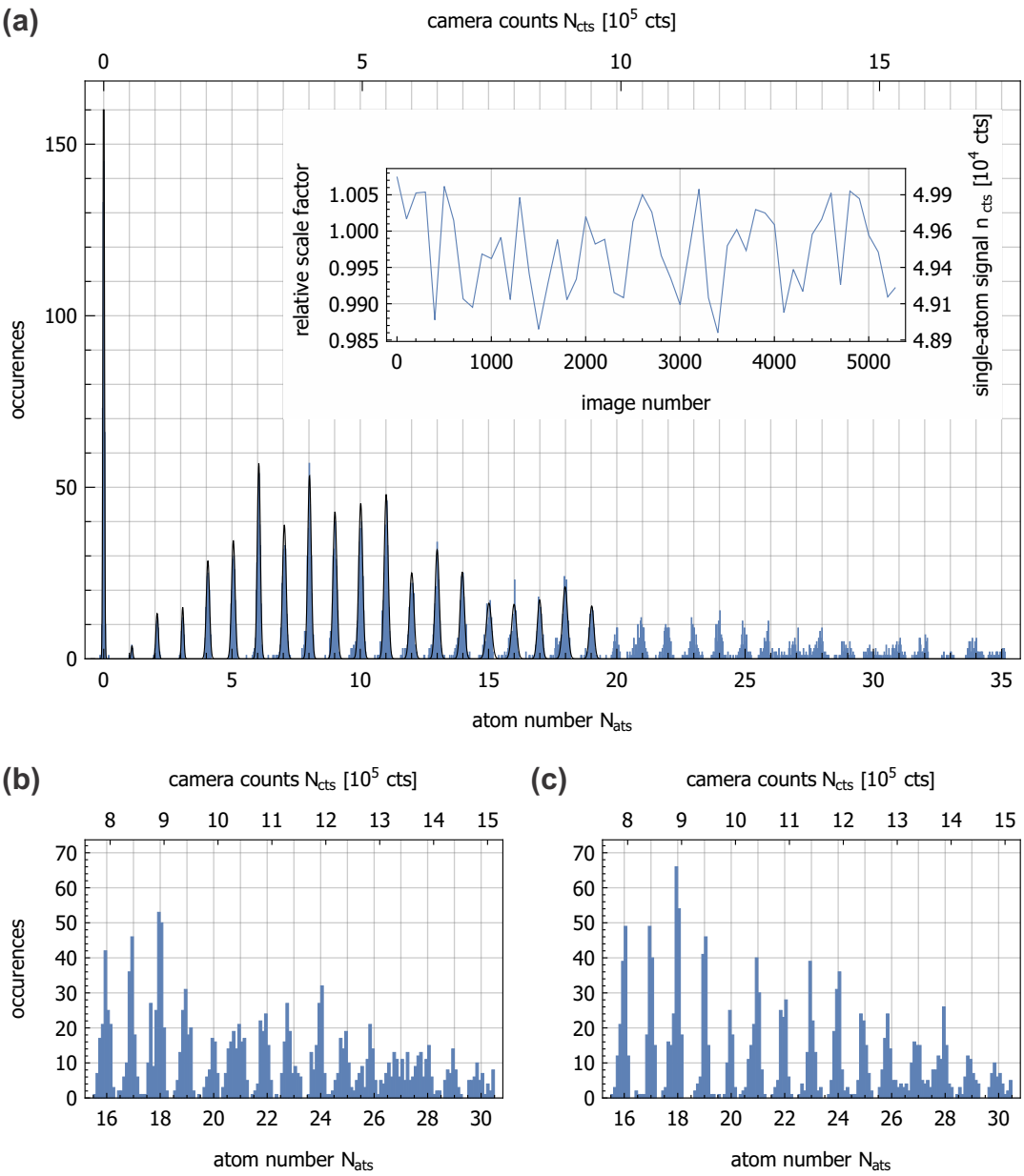

Figure 5.8: Scale factor optimization. Inset a Piecewise optimized scaling factor plotted against the image number. **a** Histogram of the atomic data after rescaling with the optimized scale factor and subsequent fit using multiple Gaussian distributions. **b,c** Close up on the histogram for the atom numbers $N_{\mathrm{ats}} = 16$ through $N_{\mathrm{ats}} = 30$ using the non-optimized (**b**) and the optimized (**c**) scale factor. While the distributions around atom numbers $N_{\mathrm{ats}} = 16$ through $N_{\mathrm{ats}} = 30$ qualitatively demonstrate a narrowing effect, the peak for $N_{\mathrm{ats}} = 27$ only becomes visible when using the optimized scaling factor.

Chapter 6

Outlook

Within this thesis, accurate atom counting has been accomplished. This was demonstrated by stable and reproducible fluorescence time traces, distinct equidistant peaks in the fluorescence histogram for more than 30 atoms and the extraction of an scale factor. Characterizing the atom number fluctuations beyond long term drifts predicts that the single-atom resolution threshold is reached at $N_{\mathrm{ats}} = 390(20)$ atoms. This thesis has outlined the important role, that such an accurate atom counting detection scheme will play in the advancement of atom optics experiments. It will enable pushing the interferometric sensitivity of interferometers operating with mesoscopic numbers of massive neutral particles towards the Heisenberg limit. Further it will aid in gaining insight in more fundamental physical concepts, such as Bell-tests and single-particle Wigner functions applied to ultracold atoms. A detailed description of these concepts was already given in Chapter 2 as it served as the motivation for the construction of a dedicated experiment that will be able to perform entanglement-enhanced atom interferometry. Around these requirements, the apparatus was designed and set up. The following sections focus on short and midterm progress with the experimental apparatus.

6.1 Improve counting performance

In order to improve the accurate atom counting performance the noise analysis of Chapter 5 already hinted that the currently limiting noise source are the scattering rate noise and drift. Thus, the frequency and intensity stability of the cooling light needs to be revisited. Automated full time monitoring of the laser powers available to the 3D-MOT configurations and the temperature on the optics tables could be used to characterize and investigate the causes of long term drifts.

If the setup is to be used as a dedicated atom number detection only, the kinetics mode of the CCD camera can be used to take images in faster succession. The kinetics mode works by physically blocking a part of the chip, only exposing a finite number of rows along its edge. After an exposure is completed, the image gets shifted within 1 ms onto the covered part of the CCD chip and a new exposure can be started. From the presented region of interest about 100×100 physical pixels it follows that up to ten images can fit on the CCD chip of the camera, allowing for the fast acquisition of one background and nine atom images. Even though it is possible to derive the atom number from a single image, this method allows to make the best use of the available dynamic range of the camera and the noise can be reduced by combining these images.

6.2 State selective detection

Extending the detection to accommodate for more than one single output mode of an experiment will be crucial to fully exploit the benefits of an accurate atom counting detection. In order to simultaneously detect the number of atoms in more than one sub ensemble to challenges need to be tackled. Firstly, the ensembles need to be separated spatially, for example by employing the of Stern-Gerlach separation. Secondly, the ensembles need to be trapped individually. This can be achieved by alternating the d-MOT with a trapping potential that forces the sub ensembles apart. A blue light sheet for example can act as repulsive barrier in between the two clouds and has been used to demonstrate a limit of upt 500 atoms for single-atom resolution [44, 44, 209]. One main benefit of using blue detuned light is that it creates a repulsive potential. Compared to an attractive potential, created by red detuned light, the unwanted scattering events are suppressed by the fact that the atoms will avoid the regions of higher intensity. The Stark shift however will increase the energy of the ground state, necessitating alternating the repulsive potential and the d-MOTThis can be extended upon by replacing the light sheet by a tightly focused blue detuned beam steered by an acousto-optical deflector to paint arbitrary partitions into the d-MOT. An optical filter can be employed to protect the detection system from the unwanted wavelength, such that only a very minute change in background signal should be expected.

6.3 Atom number stabilization

In ultracold atom experiments, fluctuating starting conditions are a seemingly unavoidable result of the preparation procedure and will occur in virtually every experimental apparatus following the typical steps outlined in Section 4.1.

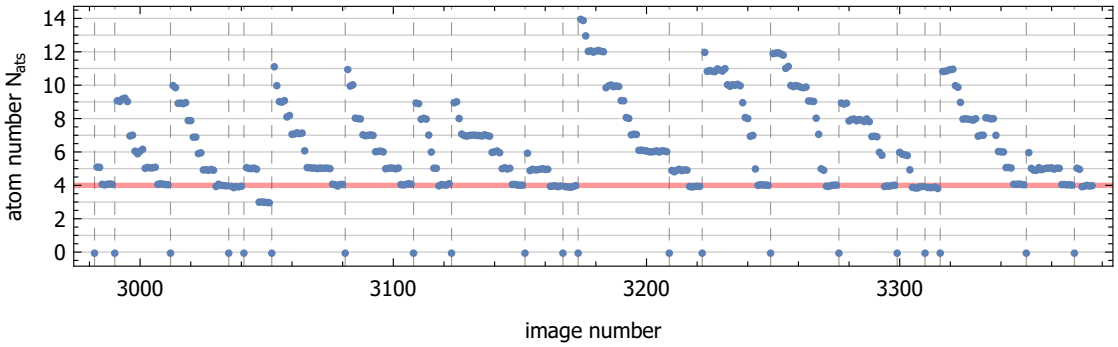

Figure 6.1: Preliminary data on atom number stabilization in the d-MOT. Time traces for experimental runs with an active atom number stabilization through loss induced by repump black outs of for a duration 3.5 ms. The red horizontal line marks the targeted atom number of $N_{ats} = 4$. The dashed vertical lines indicate the start of a new repetition of the experimental sequence. After the desired atom number was reached four additional images were taken in order to demonstrate the successfully reached atom number. In 74(3) % of all 319 repetitions the atom number was successfully controlled.

From the first step onwards, all events leading to an atom ending up within an ultracold atomic cloud are probabilistic by nature. The search for a deterministic way to prepare neutral atomic samples has lead to deterministic loading of a few Cs atoms from a magneto-optical trap into a dipole trap [211]. Single Cr atoms have been loaded into a magneto-optical trap using feedback from the fluorescence signal reaching an occupation probability as high as 98.7% [212, 213]. For much larger samples of 10^6 ^{87}Rb atoms, the number of particles in a magnetic traps was determined by a series of Farraday images [214]. There, feedback was employed by varying the number of successively applied radio-frequency pulses, spilling a controlled number of atoms from the trap.

After calibration, the accurate atom counting detection allows to accurately determine atom numbers on-the-fly. This live knowledge can be utilized in a real-time feedback loop to stabilize the atom number in the d-MOT, enabling the on-demand preparation of atom numbers. To this end, each atom image is evaluated directly after readout by the camera software. Comparing the detected number of counts to a prior set level of expected counts is used to stop a loss procedure during the holding within the experimental sequence[23]. Repeating these two steps eventually will lead to the desired number of atoms in the d-MOT. Due to the lack for designated TTL output ports on the camera computer itself, the trigger output of the camera is used to send a TTL signal to the FPGA

[23]The experimental sequence in this case is essentially the same as described in 5.1 except for the addition of a loss-mechanism during the holding time between images.

running experimental control sequence. Upon receiving the trigger signal, a predefined loss mechanism is stopped and four more images are acquired. In an initial attempt simply turning off any repump light for a duration of 3.5 ms during the holding time of the d-MOT was used to induce losses. Time traces for this are shown in Fig. 6.1. For 319 realizations in 74(3) % of the attempts the desired atom number of $N_{\mathrm{ats}} = 4$ was successfully attained. Not being able to change the strength of the induced loss makes it inevitable to design the loss process such, that the probability for an atom to get lost is low in order to avoid multiple losses in one step. Otherwise the last loss step just before reaching the desired atom number could likely fail, as the control will "overshoot" the target. Thus, to further pursuit the deterministic generation of atom numbers in the d-MOT a protocol will be needed to communicate the strength of the atom number deviation to the FPGA. Fully controlling the atom number cannot be achieved by only inducing losses to the atoms currently trapped. In order to also reach the desired atom number, when the initially loaded atom number is lower than the target could be achieved by selectively turning on the $2D^+$-MOT in order to send atoms into the science cell.

6.4 Moving towards a spinor BEC

The next steps in the construction of the apparatus will be to establish protocols for the optical molasses, optical pumping, generation of Bose-Einstein condensates and spin dynamics, while implementing remaining optics and hardware. Starting with the optical molasses, the needed optics are already in place as the i-MOT beams will be used, but careful compensation of the residual magnetic fields needs to be done. For the optical pumping, the light source is already set up and coils to generate a quantization axis are in place. A magnetic quadrupole trap should readily be realized, as the dedicated coil system is in place and connected. The dipole trap laser is put in place and the dipole trap optics are currently being implemented, including a combination of acousto-optical deflectors that will be used to steer them and generate time-averaged optical potentials.For spin-dynamics the corresponding microwave electronics need be set up.

6.5 A first experiment using accurate atom counting

Once a spin-dynamics protocol for the apparatus has been established the accurate atom counting detection can be used in conjunction with highly entangled states. In a first experiment the pair creation of the spin-dynamics process could be analyzed with single-atom precision. After a twin-Fock state of 1 to 100 atoms in the $|F = 1, m_F = \pm 1\rangle$ states has been created, the remaining atoms of the con-

densate in $|F = 1, m_F = 0\rangle$ could be pushed away by a resonant light pulse. The twin-Fock state could be released from the optical dipole trap and recaptured within the d-MOT. Upon counting the atoms only even numbers should occur, proving that the process naturally involves pairs of atoms.

Bibliography

[1] A. Einstein, B. Podolsky, and N. Rosen, *Can Quantum-Mechanical Description of Physical Reality Be Considered Complete?*, Physical Review, 47, 1935, DOI: 10.1103/PhysRev.47.777.

[2] E. Schrödinger and M. Born, *Discussion of Probability Relations between Separated Systems*, Mathematical Proceedings of the Cambridge Philosophical Society, 31, 1935, DOI: 10.1017/S0305004100013554.

[3] E. Schrödinger, *Die gegenwärtige Situation in der Quantenmechanik*, Die Naturwissenschaften, 23, 1935, DOI: 10.1007/BF01491891.

[4] E. Schrödinger and P. A. M. Dirac, *Probability Relations between Separated Systems*, Mathematical Proceedings of the Cambridge Philosophical Society, 32, 1936, DOI: 10.1017/S0305004100019137.

[5] W. H. Zurek, *Decoherence, Einselection, and the Quantum Origins of the Classical*, Reviews of Modern Physics, 75, 2003, DOI: 10.1103/RevModPhys.75.715.

[6] S. Gerlich, S. Eibenberger, M. Tomandl, S. Nimmrichter, K. Hornberger, P. J. Fagan, J. Tüxen, M. Mayor, and M. Arndt, *Quantum Interference of Large Organic Molecules*, Nature Communications, 2, 2011, DOI: 10.1038/ncomms1263.

[7] A. Bassi, K. Lochan, S. Satin, T. P. Singh, and H. Ulbricht, *Models of Wave-Function Collapse, Underlying Theories, and Experimental Tests*, Reviews of Modern Physics, 85, 2013, DOI: 10.1103/RevModPhys.85.471.

[8] X.-L. Wang, L.-K. Chen, W. Li, H.-L. Huang, C. Liu, C. Chen, Y.-H. Luo, Z.-E. Su, D. Wu, Z.-D. Li, H. Lu, Y. Hu, X. Jiang, C.-Z. Peng, L. Li, N.-L. Liu, Y.-A. Chen, C.-Y. Lu, and J.-W. Pan, *Experimental Ten-Photon Entanglement*, Physical Review Letters, 117, 2016, DOI: 10.1103/PhysRevLett.117.210502.

[9] N. Friis, G. Vitagliano, M. Malik, and M. Huber, *Entanglement Certification from Theory to Experiment*, Nature Reviews Physics, 2018, DOI: 10.1038/s42254-018-0003-5.

[10] X.-Y. Luo, Y.-Q. Zou, L.-N. Wu, Q. Liu, M.-F. Han, M. K. Tey, and L. You, *Deterministic Entanglement Generation from Driving through Quantum Phase Transitions*, Science, 355, 2017, DOI: 10.1126/science.aag1106.

[11] R. Blatt and C. F. Roos, *Quantum Simulations with Trapped Ions*, Nature Physics, 8, 2012, DOI: 10.1038/nphys2252.

[12] N. Gisin, G. Ribordy, W. Tittel, and H. Zbinden, *Quantum Cryptography*, Reviews of Modern Physics, 74, 2002, DOI: 10.1103/RevModPhys.74.145.

[13] M. A. Nielsen and I. L. Chuang, *Quantum Computation and Quantum Information*. Cambridge University Press, Cambridge ; New York, 10th anniversary ed edition, 2010.

[14] N. Gisin and R. Thew, *Quantum Communication*, Nature Photonics, 1, 2007, DOI: 10.1038/nphoton.2007.22.

[15] B. J. Bloom, T. L. Nicholson, J. R. Williams, S. L. Campbell, M. Bishof, X. Zhang, W. Zhang, S. L. Bromley, and J. Ye, *An Optical Lattice Clock with Accuracy and Stability at the 10-18 Level*, Nature, 506, 2014, DOI: 10.1038/nature12941.

[16] O. Hosten, N. J. Engelsen, R. Krishnakumar, and M. A. Kasevich, *Measurement Noise 100 Times Lower than the Quantum-Projection Limit Using Entangled Atoms*, Nature, 529, 2016, DOI: 10.1038/nature16176.

[17] M. Kasevich and S. Chu, *Measurement of the Gravitational Acceleration of an Atom with a Light-Pulse Atom Interferometer*, Applied Physics B Photophysics and Laser Chemistry, 54, 1992, DOI: 10.1007/BF00325375.

[18] Z.-K. Hu, B.-L. Sun, X.-C. Duan, M.-K. Zhou, L.-L. Chen, S. Zhan, Q.-Z. Zhang, and J. Luo, *Demonstration of an Ultrahigh-Sensitivity Atom-Interferometry Absolute Gravimeter*, Physical Review A, 88, 2013, DOI: 10.1103/PhysRevA.88.043610.

[19] G. W. Biedermann, X. Wu, L. Deslauriers, S. Roy, C. Mahadeswaraswamy, and M. A. Kasevich, *Testing Gravity with Cold-Atom Interferometers*, Physical Review A, 91, 2015, DOI: 10.1103/PhysRevA.91.033629.

[20] A. Gauguet, B. Canuel, T. Lévèque, W. Chaibi, and A. Landragin, *Characterization and Limits of a Cold-Atom Sagnac Interferometer*, Physical Review A, 80, 2009, DOI: 10.1103/PhysRevA.80.063604.

[21] G. Tackmann, P. Berg, C. Schubert, S. Abend, M. Gilowski, W. Ertmer, and E. M. Rasel, *Self-Alignment of a Compact Large-Area Atomic Sagnac Interferometer*, New Journal of Physics, 14, 2012, DOI: 10.1088/1367-2630/14/1/015002.

[22] T. L. Gustavson, P. Bouyer, and M. A. Kasevich, *Precision Rotation Measurements with an Atom Interferometer Gyroscope*, Physical Review Letters, 78, 1997, DOI: 10.1103/PhysRevLett.78.2046.

[23] J. K. Stockton, K. Takase, and M. A. Kasevich, *Absolute Geodetic Rotation Measurement Using Atom Interferometry*, Physical Review Letters, 107, 2011, DOI: 10.1103/PhysRevLett.107.133001.

[24] I. Dutta, D. Savoie, B. Fang, B. Venon, C. L. Garrido Alzar, R. Geiger, and A. Landragin, *Continuous Cold-Atom Inertial Sensor with 1 Nrad / Sec Rotation Stability*, Physical Review Letters, 116, 2016, DOI: 10.1103/PhysRevLett.116.183003.

[25] I. K. Kominis, T. W. Kornack, J. C. Allred, and M. V. Romalis, *A Subfemtotesla Multichannel Atomic Magnetometer*, Nature, 422, 2003, DOI: 10.1038/nature01484.

[26] P. Böhi, M. F. Riedel, T. W. Hänsch, and P. Treutlein, *Imaging of Microwave Fields Using Ultracold Atoms*, Appl. Phys. Lett., 97, 2010, DOI: http://dx.doi.org/10.1063/1.3470591.

[27] S. Dimopoulos, P. W. Graham, J. M. Hogan, and M. A. Kasevich, *Testing General Relativity with Atom Interferometry*, Physical Review Letters, 98, 2007, DOI: 10.1103/PhysRevLett.98.111102.

[28] L. Pezzè, A. Smerzi, M. K. Oberthaler, R. Schmied, and P. Treutlein, *Quantum Metrology with Nonclassical States of Atomic Ensembles*, Reviews of Modern Physics, 90, 2018, DOI: 10.1103/RevModPhys.90.035005.

[29] J. G. Bohnet, B. C. Sawyer, J. W. Britton, M. L. Wall, A. M. Rey, M. Foss-Feig, and J. J. Bollinger, *Quantum Spin Dynamics and Entanglement Generation with Hundreds of Trapped Ions*, Science, 352, 2016, DOI: 10.1126/science.aad9958.

[30] J. Estève, C. Gross, A. Weller, S. Giovanazzi, and M. K. Oberthaler, *Squeezing and Entanglement in a Bose–Einstein Condensate*, Nature, 455, 2008, DOI: 10.1038/nature07332.

[31] J. Appel, P. J. Windpassinger, D. Oblak, U. B. Hoff, N. Kj\a ergaard, and E. S. Polzik, *Mesoscopic Atomic Entanglement for Precision Measurements beyond the Standard Quantum Limit*, Proceedings of the National Academy of Sciences, 106, 2009.

[32] C. Gross, T. Zibold, E. Nicklas, J. Estève, and M. K. Oberthaler, *Nonlinear Atom Interferometer Surpasses Classical Precision Limit*, Nature, 464, 2010, DOI: 10.1038/nature08919.

[33] M. F. Riedel, P. Böhi, Y. Li, T. W. Hänsch, A. Sinatra, and P. Treutlein, *Atom-Chip-Based Generation of Entanglement for Quantum Metrology*, Nature, 464, 2010, DOI: 10.1038/nature08988.

[34] B. Lücke, J. Peise, G. Vitagliano, J. Arlt, L. Santos, G. Tóth, and C. Klempt, *Detecting Multiparticle Entanglement of Dicke States*, Physical review letters, 112, 2014.

[35] J. Peise, I. Kruse, K. Lange, B. Lücke, L. Pezzè, J. Arlt, W. Ertmer, K. Hammerer, L. Santos, A. Smerzi, and C. Klempt, *Satisfying the Einstein–Podolsky–Rosen Criterion with Massive Particles*, Nature Communications, 6, 2015, DOI: 10.1038/ncomms9984.

[36] B. Lücke, M. Scherer, J. Kruse, L. Pezzè, F. Deuretzbacher, P. Hyllus, O. Topic, J. Peise, W. Ertmer, J. Arlt, L. Santos, A. Smerzi, and C. Klempt, *Twin Matter Waves for Interferometry Beyond the Classical Limit*, Science, 334, 2011, DOI: 10.1126/science.1208798.

[37] W. Muessel, H. Strobel, M. Joos, E. Nicklas, I. Stroescu, J. Tomkovič, D. B. Hume, and M. K. Oberthaler, *Optimized Absorption Imaging of Mesoscopic Atomic Clouds*, Applied Physics B, 113, 2013, DOI: 10.1007/s00340-013-5553-8.

[38] Z. Hu and H. J. Kimble, *Observation of a Single Atom in a Magneto-Optical Trap*, Optics Letters, 19, 1994, DOI: 10.1364/OL.19.001888.

[39] D. Haubrich, H. Schadwinkel, F. Strauch, B. Ueberholz, R. Wynands, and D. Meschede, *Observation of Individual Neutral Atoms in Magnetic and Magneto-Optical Traps*, Europhysics Letters (EPL), 34, 1996, DOI: 10.1209/epl/i1996-00512-5.

[40] F. Ruschewitz, D. Bettermann, J. L. Peng, and W. Ertmer, *Statistical Investigations on Single Trapped Neutral Atoms*, Europhysics Letters (EPL), 34, 1996, DOI: 10.1209/epl/i1996-00510-7.

[41] P. A. Willems, R. A. Boyd, J. L. Bliss, and K. G. Libbrecht, *Stability of Magneto-Optical Traps with Large Field Gradients: Limits on the Tight Confinement of Single Atoms*, Physical Review Letters, 78, 1997, DOI: 10.1103/PhysRevLett.78.1660.

[42] W. Alt, D. Schrader, S. Kuhr, M. Müller, V. Gomer, and D. Meschede, *Single Atoms in a Standing-Wave Dipole Trap*, Physical Review A, 67, 2003, DOI: 10.1103/PhysRevA.67.033403.

[43] D. Hume, I. Stroescu, M. Joos, W. Muessel, H. Strobel, and M. Oberthaler, *Accurate Atom Counting in Mesoscopic Ensembles*, Physical Review Letters, 111, 2013, DOI: 10.1103/PhysRevLett.111.253001.

[44] I. Stroescu, D. B. Hume, and M. K. Oberthaler, *Double-Well Atom Trap for Fluorescence Detection at the Heisenberg Limit*, Physical Review A, 91, 2015, DOI: 10.1103/PhysRevA.91.013412.

[45] R. A. Campos, C. C. Gerry, and A. Benmoussa, *Optical Interferometry at the Heisenberg Limit with Twin Fock States and Parity Measurements*, Physical Review A, 68, 2003, DOI: 10.1103/PhysRevA.68.023810.

[46] B. Lücke, *Multi-Particle Entanglement in a Spinor Bose-Einstein Condensate for Quantum-Enhanced Interferometry*, PhD thesis, Leibniz Universität Hannover, Hannover, 2014.

[47] C. A. Sackett, D. Kielpinski, B. E. King, C. Langer, V. Meyer, C. J. Myatt, M. Rowe, Q. A. Turchette, W. M. Itano, D. J. Wineland, and C. Monroe, *Experimental Entanglement of Four Particles*, Nature, 404, 2000, DOI: 10.1038/35005011.

[48] V. Meyer, M. A. Rowe, D. Kielpinski, C. A. Sackett, W. M. Itano, C. Monroe, and D. J. Wineland, *Experimental Demonstration of Entanglement-Enhanced Rotation Angle Estimation Using Trapped Ions*, Physical Review Letters, 86, 2001, DOI: 10.1103/PhysRevLett.86.5870.

[49] D. Leibfried, B. DeMarco, V. Meyer, D. Lucas, M. Barrett, J. Britton, W. M. Itano, B. Jelenković, C. Langer, T. Rosenband, and D. J. Wineland, *Experimental Demonstration of a Robust, High-Fidelity Geometric Two Ion-Qubit Phase Gate*, Nature, 422, 2003, DOI: 10.1038/nature01492.

[50] D. Leibfried, M. Barrett, T. Schaetz, J. Britton, J. Chiaverini, W. M. Itano, J. D. Jost, C. Langer, and D. J. Wineland, *Toward Heisenberg-Limited Spectroscopy with Multiparticle Entangled States*, Science, 304, 2004, DOI: 10.1126/science.1097576.

[51] D. Leibfried, E. Knill, S. Seidelin, J. Britton, R. B. Blakestad, J. Chiaverini, D. B. Hume, W. M. Itano, J. D. Jost, C. Langer, R. Ozeri, R. Reichle, and D. J. Wineland, *Creation of a Six-Atom 'Schrödinger Cat' State*, Nature, 438, 2005, DOI: 10.1038/nature04251.

[52] T. Monz, P. Schindler, J. T. Barreiro, M. Chwalla, D. Nigg, W. A. Coish, M. Harlander, W. Hänsel, M. Hennrich, and R. Blatt, *14-Qubit Entanglement: Creation and Coherence*, Physical Review Letters, 106, 2011, DOI: 10.1103/PhysRevLett.106.130506.

[53] C. D. Hamley, C. S. Gerving, T. M. Hoang, E. M. Bookjans, and M. S. Chapman, *Spin-Nematic Squeezed Vacuum in a Quantum Gas*, Nature Physics, 8, 2012, DOI: 10.1038/nphys2245.

[54] T. Berrada, S. van Frank, R. Bücker, T. Schumm, J.-F. Schaff, and J. Schmiedmayer, *Integrated Mach–Zehnder Interferometer for Bose–Einstein Condensates*, Nature Communications, 4, 2013, DOI: 10.1038/ncomms3077.

[55] C. F. Ockeloen, R. Schmied, M. F. Riedel, and P. Treutlein, *Quantum Metrology with a Scanning Probe Atom Interferometer*, Physical Review Letters, 111, 2013, DOI: 10.1103/PhysRevLett.111.143001.

[56] W. Muessel, H. Strobel, D. Linnemann, D. B. Hume, and M. K. Oberthaler, *Scalable Spin Squeezing for Quantum-Enhanced Magnetometry with Bose-Einstein Condensates*, Physical Review Letters, 113, 2014, DOI: 10.1103/PhysRevLett.113.103004.

[57] H. Strobel, W. Muessel, D. Linnemann, T. Zibold, D. B. Hume, L. Pezzè, A. Smerzi, and M. K. Oberthaler, *Fisher Information and Entanglement of Non-Gaussian Spin States*, Science, 345, 2014, DOI: 10.1126/science.1250147.

[58] W. Muessel, H. Strobel, D. Linnemann, T. Zibold, B. Juliá-Díaz, and M. K. Oberthaler, *Twist-and-Turn Spin Squeezing in Bose-Einstein Condensates*, Physical Review A, 92, 2015, DOI: 10.1103/PhysRevA.92.023603.

[59] I. Kruse, K. Lange, J. Peise, B. Lücke, L. Pezzè, J. Arlt, W. Ertmer, C. Lisdat, L. Santos, A. Smerzi, and C. Klempt, *Improvement of an Atomic Clock Using Squeezed Vacuum*, Physical Review Letters, 117, 2016, DOI: 10.1103/PhysRevLett.117.143004.

[60] Y.-Q. Zou, L.-N. Wu, Q. Liu, X.-Y. Luo, S.-F. Guo, J.-H. Cao, M. K. Tey, and L. You, *Beating the Classical Precision Limit with Spin-1 Dicke States of More than 10,000 Atoms*, Proceedings of the National Academy of Sciences, 115, 2018, DOI: 10.1073/pnas.1715105115.

[61] I. D. Leroux, M. H. Schleier-Smith, and V. Vuletić, *Implementation of Cavity Squeezing of a Collective Atomic Spin*, Physical Review Letters, 104, 2010, DOI: 10.1103/PhysRevLett.104.073602.

[62] I. D. Leroux, M. H. Schleier-Smith, and V. Vuletić, *Orientation-Dependent Entanglement Lifetime in a Squeezed Atomic Clock*, Physical Review Letters, 104, 2010, DOI: 10.1103/PhysRevLett.104.250801.

[63] A. Louchet-Chauvet, J. Appel, J. J. Renema, D. Oblak, N. Kjaergaard, and E. S. Polzik, *Entanglement-Assisted Atomic Clock beyond the Projection Noise Limit*, New Journal of Physics, 12, 2010, DOI: 10.1088/1367-2630/12/6/065032.

[64] M. H. Schleier-Smith, I. D. Leroux, and V. Vuletić, *States of an Ensemble of Two-Level Atoms with Reduced Quantum Uncertainty*, Physical Review Letters, 104, 2010, DOI: 10.1103/PhysRevLett.104.073604.

[65] Z. Chen, J. G. Bohnet, S. R. Sankar, J. Dai, and J. K. Thompson, *Conditional Spin Squeezing of a Large Ensemble via the Vacuum Rabi Splitting*, Physical Review Letters, 106, 2011, DOI: 10.1103/PhysRevLett.106.133601.

[66] R. J. Sewell, M. Koschorreck, M. Napolitano, B. Dubost, N. Behbood, and M. W. Mitchell, *Magnetic Sensitivity Beyond the Projection Noise Limit by Spin Squeezing*, Physical Review Letters, 109, 2012, DOI: 10.1103/PhysRevLett.109.253605.

[67] J. G. Bohnet, K. C. Cox, M. A. Norcia, J. M. Weiner, Z. Chen, and J. K. Thompson, *Reduced Spin Measurement Back-Action for a Phase Sensitivity Ten Times beyond the Standard Quantum Limit*, Nature Photonics, 8, 2014, DOI: 10.1038/nphoton.2014.151.

[68] R. J. Sewell, M. Napolitano, N. Behbood, G. Colangelo, F. Martin Ciurana, and M. W. Mitchell, *Ultrasensitive Atomic Spin Measurements with a Nonlinear Interferometer*, Physical Review X, 4, 2014, DOI: 10.1103/PhysRevX.4.021045.

[69] G. Barontini, L. Hohmann, F. Haas, J. Estève, and J. Reichel, *Deterministic Generation of Multiparticle Entanglement by Quantum Zeno Dynamics*, Science, 349, 2015, DOI: 10.1126/science.aaa0754.

[70] K. C. Cox, G. P. Greve, J. M. Weiner, and J. K. Thompson, *Deterministic Squeezed States with Collective Measurements and Feedback*, Physical Review Letters, 116, 2016, DOI: 10.1103/PhysRevLett.116.093602.

[71] W. Wasilewski, K. Jensen, H. Krauter, J. J. Renema, M. V. Balabas, and E. S. Polzik, *Quantum Noise Limited and Entanglement-Assisted Magnetometry*, Physical Review Letters, 104, 2010, DOI: 10.1103/PhysRevLett.104.133601.

[72] G. Rosi, F. Sorrentino, L. Cacciapuoti, M. Prevedelli, and G. M. Tino, *Precision Measurement of the Newtonian Gravitational Constant Using Cold Atoms*, Nature, 510, 2014, DOI: 10.1038/nature13433.

[73] L. Zehnder, *Ein Neuer Interferenzrefraktor*, Zeitschrift für Instrumentenkunde, 11, 1891.

[74] L. Mach, *Über Einen Interferenzrefraktor*, Zeitschrift für Instrumentenkunde, 12, 1892.

[75] C. M. Caves, *Quantum-Mechanical Noise in an Interferometer*, Physical Review D, 23, 1981, DOI: 10.1103/PhysRevD.23.1693.

[76] Z. Y. Ou, *Fundamental Quantum Limit in Precision Phase Measurement*, Physical Review A, 55, 1997, DOI: 10.1103/PhysRevA.55.2598.

[77] V. Giovannetti, S. Lloyd, and L. Maccone, *Quantum Metrology*, Physical Review Letters, 96, 2006, DOI: 10.1103/PhysRevLett.96.010401.

[78] C. C. Gerry and P. Knight, *Introductory Quantum Optics*. Cambridge University Press, Cambridge, UK ; New York, 2005.

[79] R. A. Fisher, *On the Mathematical Foundations of Theoretical Statistics*, Philosophical Transactions of the Royal Society A: Mathematical, Physical and Engineering Sciences, 222, 1922, DOI: 10.1098/rsta.1922.0009.

[80] R. A. Fisher, Theory of statistical estimation, In *Mathematical Proceedings of the Cambridge Philosophical Society*, volume 22, pages 700–725. Cambridge Univ Press, 1925.

[81] H. Cramér, *Mathematical Methods of Statistics*. Princeton University Press, Princeton, 1946, OCLC: 767556225.

[82] R. C. Rao, *Information and the Accuracy Attainable in the Estimation of Statistical Parameters*, Bull. Calcutta Math. Soc., 37, 1945.

[83] S. L. Braunstein and C. M. Caves, *Statistical Distance and the Geometry of Quantum States*, Physical Review Letters, 72, 1994, DOI: 10.1103/PhysRevLett.72.3439.

[84] L. Pezzè and A. Smerzi, *Entanglement, Nonlinear Dynamics, and the Heisenberg Limit*, Physical Review Letters, 102, 2009, DOI: 10.1103/PhysRevLett.102.100401.

[85] W. Pauli, *Zur Quantenmechanik des magnetischen Elektrons*, Zeitschrift für Physik, 43, 1927, DOI: 10.1007/BF01397326.

[86] B. Yurke, S. L. McCall, and J. R. Klauder, *SU(2) and SU(1,1) Interferometers*, Physical Review A, 33, 1986, DOI: 10.1103/PhysRevA.33.4033.

[87] M. J. Holland and K. Burnett, *Interferometric Detection of Optical Phase Shifts at the Heisenberg Limit*, Physical review letters, 71, 1993.

[88] T. Kim, O. Pfister, M. J. Holland, J. Noh, and J. L. Hall, *Influence of Decorrelation on Heisenberg-Limited Interferometry with Quantum Correlated Photons*, Physical Review A, 57, 1998, DOI: 10.1103/PhysRevA.57.4004.

[89] Z. Y. Ou, J.-K. Rhee, and L. J. Wang, *Observation of Four-Photon Interference with a Beam Splitter by Pulsed Parametric Down-Conversion*, Physical Review Letters, 83, 1999, DOI: 10.1103/PhysRevLett.83.959.

[90] T. Nagata, R. Okamoto, J. L. O'Brien, K. Sasaki, and S. Takeuchi, *Beating the Standard Quantum Limit with Four-Entangled Photons*, Science, 316, 2007, DOI: 10.1126/science.1138007.

[91] C. C. Gerry, R. A. Campos, and A. Benmoussa, *Comment on "Interferometric Detection of Optical Phase Shifts at the Heisenberg Limit"*, Physical Review Letters, 92, 2004, DOI: 10.1103/PhysRevLett.92.209301.

[92] P. M. Anisimov, G. M. Raterman, A. Chiruvelli, W. N. Plick, S. D. Huver, H. Lee, and J. P. Dowling, *Quantum Metrology with Two-Mode Squeezed Vacuum: Parity Detection Beats the Heisenberg Limit*, Physical Review Letters, 104, 2010, DOI: 10.1103/PhysRevLett.104.103602.

[93] C. K. Hong, Z. Y. Ou, and L. Mandel, *Measurement of Subpicosecond Time Intervals between Two Photons by Interference*, Physical Review Letters, 59, 1987, DOI: 10.1103/PhysRevLett.59.2044.

[94] R. Krischek, C. Schwemmer, W. Wieczorek, H. Weinfurter, P. Hyllus, L. Pezzè, and A. Smerzi, *Useful Multiparticle Entanglement and Sub-Shot-Noise Sensitivity in Experimental Phase Estimation*, Physical Review Letters, 107, 2011, DOI: 10.1103/PhysRevLett.107.080504.

[95] L. Pezzè and A. Smerzi, *Phase Sensitivity of a Mach-Zehnder Interferometer*, Physical Review A, 73, 2006, DOI: 10.1103/PhysRevA.73.011801.

[96] A. I. Lvovsky and M. G. Raymer, *Continuous-Variable Optical Quantum-State Tomography*, Reviews of Modern Physics, 81, 2009, DOI: 10.1103/RevModPhys.81.299.

[97] A. I. Lvovsky, H. Hansen, T. Aichele, O. Benson, J. Mlynek, and S. Schiller, *Quantum State Reconstruction of the Single-Photon Fock State*, Physical Review Letters, 87, 2001, DOI: 10.1103/PhysRevLett.87.050402.

[98] A. Zavatta, S. Viciani, and M. Bellini, *Tomographic Reconstruction of the Single-Photon Fock State by High-Frequency Homodyne Detection*, Physical Review A, 70, 2004, DOI: 10.1103/PhysRevA.70.053821.

[99] A. Ourjoumtsev, R. Tualle-Brouri, and P. Grangier, *Quantum Homodyne Tomography of a Two-Photon Fock State*, Physical Review Letters, 96, 2006, DOI: 10.1103/PhysRevLett.96.213601.

[100] M. Cooper, L. J. Wright, C. Söller, and B. J. Smith, *Experimental Generation of Multi-Photon Fock States*, Optics express, 21, 2013.

[101] A. Zavatta, *Quantum-to-Classical Transition with Single-Photon-Added Coherent States of Light*, Science, 306, 2004, DOI: 10.1126/science.1103190.

[102] A. Zavatta, S. Viciani, and M. Bellini, *Single-Photon Excitation of a Coherent State: Catching the Elementary Step of Stimulated Light Emission*, Physical Review A, 72, 2005, DOI: 10.1103/PhysRevA.72.023820.

[103] R. Kumar, E. Barrios, C. Kupchak, and A. I. Lvovsky, *Experimental Characterization of Bosonic Creation and Annihilation Operators*, Physical Review Letters, 110, 2013, DOI: 10.1103/PhysRevLett.110.130403.

[104] D. T. Smithey, M. Beck, M. G. Raymer, and A. Faridani, *Measurement of the Wigner Distribution and the Density Matrix of a Light Mode Using Optical Homodyne Tomography: Application to Squeezed States and the Vacuum*, Physical Review Letters, 70, 1993, DOI: 10.1103/PhysRevLett.70.1244.

[105] D. C. Burnham and D. L. Weinberg, *Observation of Simultaneity in Parametric Production of Optical Photon Pairs*, Physical Review Letters, 25, 1970, DOI: 10.1103/PhysRevLett.25.84.

[106] P. J. Mosley, J. S. Lundeen, B. J. Smith, P. Wasylczyk, A. B. U'Ren, C. Silberhorn, and I. A. Walmsley, *Heralded Generation of Ultrafast Single Photons in Pure Quantum States*, Physical Review Letters, 100, 2008, DOI: 10.1103/PhysRevLett.100.133601.

[107] C. Gross, H. Strobel, E. Nicklas, T. Zibold, N. Bar-Gill, G. Kurizki, and M. K. Oberthaler, *Atomic Homodyne Detection of Continuous-Variable Entangled Twin-Atom States*, Nature, 480, 2011, DOI: 10.1038/nature10654.

[108] J. Peise, B. Lücke, L. Pezzè, F. Deuretzbacher, W. Ertmer, J. Arlt, A. Smerzi, L. Santos, and C. Klempt, *Interaction-Free Measurements by Quantum Zeno Stabilization of Ultracold Atoms*, Nature Communications, 6, 2015, DOI: 10.1038/ncomms7811.

[109] D. M. Stamper-Kurn and M. Ueda, *Spinor Bose Gases: Symmetries, Magnetism, and Quantum Dynamics*, Reviews of Modern Physics, 85, 2013, DOI: 10.1103/RevModPhys.85.1191.

[110] E. Wigner, *On the Quantum Correction For Thermodynamic Equilibrium*, Physical Review, 40, 1932, DOI: 10.1103/PhysRev.40.749.

[111] U. Leonhardt, P. Knight, and A. Miller, *Measuring the Quantum State of Light*, Cambridge Studies in Modern Optics. Cambridge University Press, 1997.

[112] K. Vogel and H. Risken, *Determination of Quasiprobability Distributions in Terms of Probability Distributions for the Rotated Quadrature Phase*, Physical Review A, 40, 1989, DOI: 10.1103/PhysRevA.40.2847.

[113] D.-G. Welsch, W. Vogel, and T. Opatrný, II Homodyne Detection and Quantum-State Reconstruction, In *Progress in Optics*, volume 39, pages 63–211. Elsevier, 1999, DOI: 10.1016/S0079-6638(08)70389-5.

[114] D.-G. Welsch, W. Vogel, and T. Opatrnỳ, *Homodyne Detection and Quantum State Reconstruction*, arXiv:0907.1353 [quant-ph], 2009.

[115] G. M. D'Ariano, C. Macchiavello, and M. G. A. Paris, *Detection of the Density Matrix through Optical Homodyne Tomography without Filtered Back Projection*, Physical Review A, 50, 1994, DOI: 10.1103/PhysRevA.50.4298.

[116] G. M. D'Ariano, U. Leonhardt, and H. Paul, *Homodyne Detection of the Density Matrix of the Radiation Field*, Physical Review A, 52, 1995, DOI: 10.1103/PhysRevA.52.R1801.

[117] A. Wünsche, *Radon Transform and Pattern Functions in Quantum Tomography*, Journal of Modern Optics, 44, 1997, DOI: 10.1080/09500349708231885.

[118] T. Richter, *Realistic Pattern Functions for Optical Homodyne Tomography and Determination of Specific Expectation Values*, Physical Review A, 61, 2000, DOI: 10.1103/PhysRevA.61.063819.

[119] Z. Hradil, *Quantum-State Estimation*, Physical Review A, 55, 1997, DOI: 10.1103/PhysRevA.55.R1561.

[120] K. Banaszek, *Maximum-Likelihood Estimation of Photon-Number Distribution from Homodyne Statistics*, Physical Review A, 57, 1998, DOI: 10.1103/PhysRevA.57.5013.

[121] A. I. Lvovsky, *Iterative Maximum-Likelihood Reconstruction in Quantum Homodyne Tomography*, Journal of Optics B: Quantum and Semiclassical Optics, 6, 2004, DOI: 10.1088/1464-4266/6/6/014.

[122] T. Aichele, A. Lvovsky, and S. Schiller, *Optical Mode Characterization of Single Photons Prepared by Means of Conditional Measurements on a Biphoton State*, The European Physical Journal D - Atomic, Molecular and Optical Physics, 18, 2002, DOI: 10.1140/epjd/e20020028.

[123] C. S. Wu and I. Shaknov, *The Angular Correlation of Scattered Annihilation Radiation*, Physical Review, 77, 1950, DOI: 10.1103/PhysRev.77.136.

[124] W. Heisenberg, *Über den anschaulichen Inhalt der quantentheoretischen Kinematik und Mechanik*, Zeitschrift für Physik, 43, 1927, DOI: 10.1007/BF01397280.

[125] J. S. Bell, *On the Einstein Podolsky Rosen Paradox*, Physics, 1, 1964.

[126] D. Bohm and Y. Aharonov, *Discussion of Experimental Proof for the Paradox of Einstein, Rosen, and Podolsky*, Physical Review, 108, 1957, DOI: 10.1103/PhysRev.108.1070.

[127] J. F. Clauser, M. A. Horne, A. Shimony, and R. A. Holt, *Proposed Experiment to Test Local Hidden-Variable Theories*, Physical Review Letters, 23, 1969, DOI: 10.1103/PhysRevLett.23.880.

[128] S. J. Freedman and J. F. Clauser, *Experimental Test of Local Hidden-Variable Theories*, Physical Review Letters, 28, 1972, DOI: 10.1103/PhysRevLett.28.938.

[129] A. Aspect, P. Grangier, and G. Roger, *Experimental Tests of Realistic Local Theories via Bell's Theorem*, Physical Review Letters, 47, 1981, DOI: 10.1103/PhysRevLett.47.460.

[130] A. Aspect, P. Grangier, and G. Roger, *Experimental Realization of Einstein-Podolsky-Rosen-Bohm* Gedankenexperiment *: A New Violation of Bell's Inequalities*, Physical Review Letters, 49, 1982, DOI: 10.1103/PhysRevLett.49.91.

[131] A. Aspect, *Bell's Inequality Test: More Ideal than Ever*, Nature, 398, 1999, DOI: 10.1038/18296.

[132] E. S. Fry and R. C. Thompson, *Experimental Test of Local Hidden-Variable Theories*, Physical Review Letters, 37, 1976, DOI: 10.1103/PhysRevLett.37.465.

[133] E. S. Fry, *Bell Inequalities and Two Experimental Tests with Mercury*, Quantum and Semiclassical Optics: Journal of the European Optical Society Part B, 7, 1995, DOI: 10.1088/1355-5111/7/3/005.

[134] A. Aspect, J. Dalibard, and G. Roger, *Experimental Test of Bell's Inequalities Using Time-Varying Analyzers*, Physical Review Letters, 49, 1982, DOI: 10.1103/PhysRevLett.49.1804.

[135] M. A. Rowe, D. Kielpinski, V. Meyer, C. A. Sackett, W. M. Itano, C. Monroe, and D. J. Wineland, *Experimental Violation of a Bell's Inequality with Efficient Detection*, Nature, 409, 2001, DOI: 10.1038/35057215.

[136] D. N. Matsukevich, P. Maunz, D. L. Moehring, S. Olmschenk, and C. Monroe, *Bell Inequality Violation with Two Remote Atomic Qubits*, Physical Review Letters, 100, 2008, DOI: 10.1103/PhysRevLett.100.150404.

[137] J. Hofmann, M. Krug, N. Ortegel, L. Gerard, M. Weber, W. Rosenfeld, and H. Weinfurter, *Heralded Entanglement Between Widely Separated Atoms*, Science, 337, 2012, DOI: 10.1126/science.1221856.

[138] N. Brunner, D. Cavalcanti, S. Pironio, V. Scarani, and S. Wehner, *Bell Nonlocality*, Reviews of Modern Physics, 86, 2014, DOI: 10.1103/RevModPhys.86.419.

[139] B. Hensen, H. Bernien, A. E. Dréau, A. Reiserer, N. Kalb, M. S. Blok, J. Ruitenberg, R. F. L. Vermeulen, R. N. Schouten, C. Abellán, W. Amaya, V. Pruneri, M. W. Mitchell, M. Markham, D. J. Twitchen, D. Elkouss, S. Wehner, T. H. Taminiau, and R. Hanson, *Loophole-Free Bell Inequality Violation Using Electron Spins Separated by 1.3 Kilometres*, Nature, 526, 2015, DOI: 10.1038/nature15759.

[140] M. Giustina, M. A. M. Versteegh, S. Wengerowsky, J. Handsteiner, A. Hochrainer, K. Phelan, F. Steinlechner, J. Kofler, J.-A. Larsson, C. Abellán, W. Amaya, V. Pruneri, M. W. Mitchell, J. Beyer, T. Gerrits, A. E. Lita, L. K. Shalm, S. W. Nam, T. Scheidl, R. Ursin, B. Wittmann, and A. Zeilinger, *Significant-Loophole-Free Test of Bell's Theorem with Entangled Photons*, Physical Review Letters, 115, 2015, DOI: 10.1103/PhysRevLett.115.250401.

[141] L. K. Shalm, E. Meyer-Scott, B. G. Christensen, P. Bierhorst, M. A. Wayne, M. J. Stevens, T. Gerrits, S. Glancy, D. R. Hamel, M. S. Allman, K. J. Coakley, S. D. Dyer, C. Hodge, A. E. Lita, V. B. Verma, C. Lambrocco, E. Tortorici, A. L. Migdall, Y. Zhang, D. R. Kumor, W. H. Farr, F. Marsili, M. D. Shaw, J. A. Stern, C. Abellán, W. Amaya, V. Pruneri, T. Jennewein, M. W. Mitchell, P. G. Kwiat, J. C. Bienfang, R. P. Mirin, E. Knill, and S. W. Nam, *Strong Loophole-Free Test of Local Realism*, Physical Review Letters, 115, 2015, DOI: 10.1103/PhysRevLett.115.250402.

[142] A. Aspect, *Closing the Door on Einstein and Bohr's Quantum Debate*, Physics, 8, 2015, DOI: 10.1103/Physics.8.123.

[143] W. Rosenfeld, D. Burchardt, R. Garthoff, K. Redeker, N. Ortegel, M. Rau, and H. Weinfurter, *Event-Ready Bell Test Using Entangled Atoms Simultaneously Closing Detection and Locality Loopholes*, Physical Review Letters, 119, 2017, DOI: 10.1103/PhysRevLett.119.010402.

[144] The BIG Bell Test Collaboration, *Challenging Local Realism with Human Choices*, Nature, 557, 2018, DOI: 10.1038/s41586-018-0085-3.

[145] B. P. Lanyon, M. Zwerger, P. Jurcevic, C. Hempel, W. Dür, H. J. Briegel, R. Blatt, and C. F. Roos, *Experimental Violation of Multipartite Bell Inequalities with Trapped Ions*, Physical Review Letters, 112, 2014, DOI: 10.1103/PhysRevLett.112.100403.

[146] R. McConnell, H. Zhang, J. Hu, S. Ćuk, and V. Vuletić, *Entanglement with Negative Wigner Function of Almost 3,000 Atoms Heralded by One Photon*, Nature, 519, 2015, DOI: 10.1038/nature14293.

[147] W. H. Furry, *Note on the Quantum-Mechanical Theory of Measurement*, Physical Review, 49, 1936, DOI: 10.1103/PhysRev.49.393.

[148] M. D. Reid and D. F. Walls, *Violations of Classical Inequalities in Quantum Optics*, Physical Review A, 34, 1986, DOI: 10.1103/PhysRevA.34.1260.

[149] N. Killoran, M. Cramer, and M. B. Plenio, *Extracting Entanglement from Identical Particles*, Physical Review Letters, 112, 2014, DOI: 10.1103/PhysRevLett.112.150501.

[150] J. Tura, R. Augusiak, A. B. Sainz, T. Vertesi, M. Lewenstein, and A. Acin, *Detecting Nonlocality in Many-Body Quantum States*, Science, 344, 2014, DOI: 10.1126/science.1247715.

[151] J. Tura, R. Augusiak, A. Sainz, B. Lücke, C. Klempt, M. Lewenstein, and A. Acín, *Nonlocality in Many-Body Quantum Systems Detected with Two-Body Correlators*, Annals of Physics, 362, 2015, DOI: 10.1016/j.aop.2015.07.021.

[152] R. Schmied, J.-D. Bancal, B. Allard, M. Fadel, V. Scarani, P. Treutlein, and N. Sangouard, *Bell Correlations in a Bose-Einstein Condensate*, Science, 352, 2016, DOI: 10.1126/science.aad8665.

[153] N. J. Engelsen, R. Krishnakumar, O. Hosten, and M. A. Kasevich, *Bell Correlations in Spin-Squeezed States of 500 000 Atoms*, Physical Review Letters, 118, 2017, DOI: 10.1103/PhysRevLett.118.140401.

[154] I. Marinković, A. Wallucks, R. Riedinger, S. Hong, M. Aspelmeyer, and S. Gröblacher, *Optomechanical Bell Test*, Physical Review Letters, 121, 2018, DOI: 10.1103/PhysRevLett.121.220404.

[155] K. Lange, J. Peise, B. Lücke, I. Kruse, G. Vitagliano, I. Apellaniz, M. Kleinmann, G. Tóth, and C. Klempt, *Entanglement between Two Spatially Separated Atomic Modes*, Science, 360, 2018, DOI: 10.1126/science.aao2035.

[156] M. Fadel, T. Zibold, B. Décamps, and P. Treutlein, *Spatial Entanglement Patterns and Einstein-Podolsky-Rosen Steering in Bose-Einstein Condensates*, Science, 360, 2018, DOI: 10.1126/science.aao1850.

[157] P. Kunkel, M. Prüfer, H. Strobel, D. Linnemann, A. Frölian, T. Gasenzer, M. Gärttner, and M. K. Oberthaler, *Spatially Distributed Multipartite Entanglement Enables EPR Steering of Atomic Clouds*, Science, 360, 2018, DOI: 10.1126/science.aao2254.

[158] K. Lange, J. Peise, B. Lücke, T. Gruber, A. Sala, A. Polls, W. Ertmer, B. Juliá-Díaz, L. Santos, and C. Klempt, *Creation of Entangled Atomic States by an Analogue of the Dynamical Casimir Effect*, arXiv:1805.02560 [cond-mat, physics:quant-ph], 2018.

[159] K. Lange, *Two-Mode Entanglement in Spin and Spatial Degrees of Freedom*, PhD thesis, Leibniz Universität Hannover, Hannover, 2018.

[160] H. M. Wiseman, S. J. Jones, and A. C. Doherty, *Steering, Entanglement, Nonlocality, and the Einstein-Podolsky-Rosen Paradox*, Physical Review Letters, 98, 2007, DOI: 10.1103/PhysRevLett.98.140402.

[161] B. Yurke and D. Stoler, *Bell's-Inequality Experiments Using Independent-Particle Sources*, Physical Review A, 46, 1992, DOI: 10.1103/PhysRevA.46.2229.

[162] F. Laloë and W. J. Mullin, *Interferometry with Independent Bose-Einstein Condensates: Parity as an EPR/Bell Quantum Variable*, The European Physical Journal B, 70, 2009, DOI: 10.1140/epjb/e2009-00248-6.

[163] W. J. Mullin and F. Laloë, *Interferometer Tests for Quantum Non-Locality Using Bose-Einstein Condensates*, Journal of Physics: Conference Series, 150, 2009, DOI: 10.1088/1742-6596/150/3/032068.

[164] H. Ott, *Single Atom Detection in Ultracold Quantum Gases: A Review of Current Progress*, Reports on Progress in Physics, 79, 2016, DOI: 10.1088/0034-4885/79/5/054401.

[165] W. S. Bakr, J. I. Gillen, A. Peng, S. Fölling, and M. Greiner, *A Quantum Gas Microscope for Detecting Single Atoms in a Hubbard-Regime Optical Lattice*, Nature, 462, 2009, DOI: 10.1038/nature08482.

[166] A. Robert, O. Sirjean, A. Browaeys, J. Poupard, S. Nowak, D. Boiron, C. I. Westbrook, and A. Aspect, *A Bose-Einstein Condensate of Metastable Atoms*, Science, 292, 2001, DOI: 10.1126/science.1060622.

[167] A. S. Tychkov, T. Jeltes, J. M. McNamara, P. J. J. Tol, N. Herschbach, W. Hogervorst, and W. Vassen, *Metastable Helium Bose-Einstein Condensate with a Large Number of Atoms*, Physical Review A, 73, 2006, DOI: 10.1103/PhysRevA.73.031603.

[168] W. Vassen, C. Cohen-Tannoudji, M. Leduc, D. Boiron, C. I. Westbrook, A. Truscott, K. Baldwin, G. Birkl, P. Cancio, and M. Trippenbach, *Cold and Trapped Metastable Noble Gases*, Reviews of Modern Physics, 84, 2012, DOI: 10.1103/RevModPhys.84.175.

[169] J.-C. Jaskula, M. Bonneau, G. B. Partridge, V. Krachmalnicoff, P. Deuar, K. V. Kheruntsyan, A. Aspect, D. Boiron, and C. I. Westbrook, *Sub-Poissonian Number Differences in Four-Wave Mixing of Matter Waves*, Physical Review Letters, 105, 2010, DOI: 10.1103/PhysRevLett.105.190402.

[170] T. Gericke, C. Utfeld, N. Hommerstad, and H. Ott, *A Scanning Electron Microscope for Ultracold Atoms*, Laser Physics Letters, 3, 2006, DOI: 10.1002/lapl.200610028.

[171] T. Gericke, P. Würtz, D. Reitz, C. Utfeld, and H. Ott, *All-Optical Formation of a Bose–Einstein Condensate for Applications in Scanning Electron Microscopy*, Applied Physics B, 89, 2007, DOI: 10.1007/s00340-007-2862-9.

[172] T. Gericke, P. Würtz, D. Reitz, T. Langen, and H. Ott, *High-Resolution Scanning Electron Microscopy of an Ultracold Quantum Gas*, Nature Physics, 4, 2008, DOI: 10.1038/nphys1102.

[173] P. Würtz, T. Langen, T. Gericke, A. Koglbauer, and H. Ott, *Experimental Demonstration of Single-Site Addressability in a Two-Dimensional Optical Lattice*, Physical Review Letters, 103, 2009, DOI: 10.1103/PhysRevLett.103.080404.

[174] S. Kraft, A. Günther, J. Fortágh, and C. Zimmermann, *Spatially Resolved Photoionization of Ultracold Atoms on an Atom Chip*, Physical Review A, 75, 2007, DOI: 10.1103/PhysRevA.75.063605.

[175] A. Stibor, S. Kraft, T. Campey, D. Komma, A. Günther, J. Fortágh, C. Vale, H. Rubinsztein-Dunlop, and C. Zimmermann, *Calibration of a Single-Atom Detector for Atomic Microchips*, Physical Review A, 76, 2007, DOI: 10.1103/PhysRevA.76.033614.

[176] A. Stibor, H. Bender, S. Kühnhold, J. Fortágh, C. Zimmermann, and A. Günther, *Single-Atom Detection on a Chip: From Realization to Application*, New Journal of Physics, 12, 2010, DOI: 10.1088/1367-2630/12/6/065034.

[177] A. Günther, H. Bender, A. Stibor, J. Fortágh, and C. Zimmermann, *Observing Quantum Gases in Real Time: Single-Atom Detection on a Chip*, Physical Review A, 80, 2009, DOI: 10.1103/PhysRevA.80.011604.

[178] T. Campey, C. J. Vale, M. J. Davis, N. R. Heckenberg, H. Rubinsztein-Dunlop, S. Kraft, C. Zimmermann, and J. Fortágh, *Atom Counting in Ultracold Gases Using Photoionization and Ion Detection*, Physical Review A, 74, 2006, DOI: 10.1103/PhysRevA.74.043612.

[179] F. Henkel, M. Krug, J. Hofmann, W. Rosenfeld, M. Weber, and H. Weinfurter, *Highly Efficient State-Selective Submicrosecond Photoionization Detection of Single Atoms*, Physical Review Letters, 105, 2010, DOI: 10.1103/PhysRevLett.105.253001.

[180] M. Viteau, J. Radogostowicz, A. Chotia, M. G. Bason, N. Malossi, F. Fuso, D. Ciampini, O. Morsch, I. I. Ryabtsev, and E. Arimondo, *Ion Detection in the Photoionization of a Rb Bose–Einstein Condensate*, Journal of Physics B: Atomic, Molecular and Optical Physics, 44, 2011, DOI: 10.1088/0953-4075/44/7/079802.

[181] M. K. Tey, Z. Chen, S. A. Aljunid, B. Chng, F. Huber, G. Maslennikov, and C. Kurtsiefer, *Strong Interaction between Light and a Single Trapped Atom without the Need for a Cavity*, Nature Physics, 4, 2008, DOI: 10.1038/nphys1096.

[182] R. Bücker, A. Perrin, S. Manz, T. Betz, C. Koller, T. Plisson, J. Rottmann, T. Schumm, and J. Schmiedmayer, *Single-Particle-Sensitive Imaging of Freely Propagating Ultracold Atoms*, New Journal of Physics, 11, 2009, DOI: 10.1088/1367-2630/11/10/103039.

[183] R. Bücker, J. Grond, S. Manz, T. Berrada, T. Betz, C. Koller, U. Hohenester, T. Schumm, A. Perrin, and J. Schmiedmayer, *Twin-Atom Beams*, Nature Physics, 7, 2011, DOI: 10.1038/nphys1992.

[184] R. Bücker, U. Hohenester, T. Berrada, S. van Frank, A. Perrin, S. Manz, T. Betz, J. Grond, T. Schumm, and J. Schmiedmayer, *Dynamics of Parametric Matter-Wave Amplification*, Physical Review A, 86, 2012, DOI: 10.1103/PhysRevA.86.013638.

[185] A. Perrin, R. Bücker, S. Manz, T. Betz, C. Koller, T. Plisson, T. Schumm, and J. Schmiedmayer, *Hanbury Brown and Twiss Correlations across the Bose–Einstein Condensation Threshold*, Nature Physics, 8, 2012, DOI: 10.1038/nphys2212.

[186] N. Schlosser, G. Reymond, I. Protsenko, and P. Grangier, *Sub-Poissonian Loading of Single Atoms in a Microscopic Dipole Trap*, Nature, 411, 2001.

[187] T. Grünzweig, A. Hilliard, M. McGovern, and M. F. Andersen, *Near-Deterministic Preparation of a Single Atom in an Optical Microtrap*, Nature Physics, 6, 2010, DOI: 10.1038/nphys1778.

[188] M. McGovern, A. J. Hilliard, T. Grünzweig, and M. F. Andersen, *Counting Atoms in a Deep Optical Microtrap*, Optics letters, 36, 2011.

[189] A. Fuhrmanek, R. Bourgain, Y. R. P. Sortais, and A. Browaeys, *Light-Assisted Collisions between a Few Cold Atoms in a Microscopic Dipole Trap*, Physical Review A, 85, 2012, DOI: 10.1103/PhysRevA.85.062708.

[190] P. Sompet, A. V. Carpentier, Y. H. Fung, M. McGovern, and M. F. Andersen, *Dynamics of Two Atoms Undergoing Light-Assisted Collisions in an Optical Microtrap*, Physical Review A, 88, 2013, DOI: 10.1103/PhysRevA.88.051401.

[191] N. Schlosser, G. Reymond, and P. Grangier, *Collisional Blockade in Microscopic Optical Dipole Traps*, Physical Review Letters, 89, 2002, DOI: 10.1103/PhysRevLett.89.023005.

[192] A. J. Hilliard, Y. H. Fung, P. Sompet, A. V. Carpentier, and M. F. Andersen, *In-Trap Fluorescence Detection of Atoms in a Microscopic Dipole Trap*, Physical Review A, 91, 2015, DOI: 10.1103/PhysRevA.91.053414.

[193] E. L. Raab, M. Prentiss, A. Cable, S. Chu, and D. E. Pritchard, *Trapping of Neutral Sodium Atoms with Radiation Pressure*, Physical Review Letters, 59, 1987, DOI: 10.1103/PhysRevLett.59.2631.

[194] W. D. Phillips, *Nobel Lecture: Laser Cooling and Trapping of Neutral Atoms*, Reviews of Modern Physics, 70, 1998, DOI: 10.1103/RevModPhys.70.721.

[195] H. J. Metcalf, *Laser Cooling and Trapping*, Graduate Texts in Contemporary Physics. Springer, New York, 1999.

[196] S. Jöllenbeck, J. Mahnke, R. Randoll, W. Ertmer, J. Arlt, and C. Klempt, *Hexapole-Compensated Magneto-Optical Trap on a Mesoscopic Atom Chip*, Physical Review A, 83, 2011, DOI: 10.1103/PhysRevA.83.043406.

[197] P. D. Lett, R. N. Watts, C. I. Westbrook, W. D. Phillips, P. L. Gould, and H. J. Metcalf, *Observation of Atoms Laser Cooled below the Doppler Limit*, Physical Review Letters, 61, 1988, DOI: 10.1103/PhysRevLett.61.169.

[198] W. Ketterle and N. van Druten, Evaporative cooling of trapped atoms, In *Advances In Atomic, Molecular, and Optical Physics*, volume 37, pages 181–236. Elsevier, 1996, DOI: 10.1016/S1049-250X(08)60101-9.

[199] R. Grimm, M. Weidemüller, and Y. B. Ovchinnikov, Optical Dipole Traps for Neutral Atoms, In *Advances In Atomic, Molecular, and Optical Physics*, volume 42, pages 95–170. Elsevier, 2000, DOI: 10.1016/S1049-250X(08)60186-X.

[200] C. S. Adams, H. J. Lee, N. Davidson, M. Kasevich, and S. Chu, *Evaporative Cooling in a Crossed Dipole Trap*, Physical Review Letters, 74, 1995, DOI: 10.1103/PhysRevLett.74.3577.

[201] L. Schaefer, *Painted optical potentials for Ultra-Cold Atoms*, Master's thesis, Leibniz Universität Hannover, 2017.

[202] M. Hetzel, *Dynamical two-dimensional potentials for ultracold atoms*, Master's thesis, Leibniz Universität Hannover, 2018.

[203] F. Gerbier, A. Widera, S. Fölling, O. Mandel, and I. Bloch, *Resonant Control of Spin Dynamics in Ultracold Quantum Gases by Microwave Dressing*, Physical Review A, 73, 2006, DOI: 10.1103/PhysRevA.73.041602.

[204] S. R. Leslie, J. Guzman, M. Vengalattore, J. D. Sau, M. L. Cohen, and D. M. Stamper-Kurn, *Amplification of Fluctuations in a Spinor Bose-Einstein Condensate*, Physical Review A, 79, 2009, DOI: 10.1103/PhysRevA.79.043631.

[205] E. M. Bookjans, C. D. Hamley, and M. S. Chapman, *Strong Quantum Spin Correlations Observed in Atomic Spin Mixing*, Physical Review Letters, 107, 2011, DOI: 10.1103/PhysRevLett.107.210406.

[206] S. Chaudhuri, S. Roy, and C. S. Unnikrishnan, *Realization of an Intense Cold Rb Atomic Beam Based on a Two-Dimensional Magneto-Optical Trap: Experiments and Comparison with Simulations*, Physical Review A, 74, 2006, DOI: 10.1103/PhysRevA.74.023406.

[207] D. A. Steck, *Rubidium 87 D Line Data, Available Online at http://steck.us/alkalidata (Revision 2.1.4)*. 2010.

[208] J. C. Simpson, J. E. Lane, C. D. Immer, and R. C. Youngquist, *Simple Analytic Expressions for the Magnetic Field of a Circular Current Loop*, available online at https://ntrs.nasa.gov/search.jsp?R=20010038494, Document ID: 20010038494, Contract/Grant: NAS10-98001, Financial Sponsor: NASA Kennedy Space Center; Cocoa Beach, FL United States, Organization: DYNACS Engineering Co., Inc.; Cocoa Beach, FL United States, 2001.

[209] I. Stroescu, *Dissipative Double-Well Potential: Mesoscopic Atom Number Detection and Cold Atom Dynamics*, PhD thesis, Ruperto-Carola Universität Heidelberg, 2014.

[210] J. Mahnke, *A Continuously Pumped Reservoir of Ultracold Atoms*, PhD thesis, Leibniz Universität Hannover, Hannover, 2015.

[211] D. Frese, B. Ueberholz, S. Kuhr, W. Alt, D. Schrader, V. Gomer, and D. Meschede, *Single Atoms in an Optical Dipole Trap: Towards a Deterministic Source of Cold Atoms*, Physical Review Letters, 85, 2000, DOI: 10.1103/PhysRevLett.85.3777.

[212] S. B. Hill and J. J. McClelland, *Atoms on Demand: Fast, Deterministic Production of Single Cr Atoms*, Applied Physics Letters, 82, 2003, DOI: 10.1063/1.1572539.

[213] S. B. Hill and J. J. McClelland, *Performance of a Feedback-Controlled, Deterministic Source of Single Chromium Atoms*, Journal of the Optical Society of America B, 21, 2004, DOI: 10.1364/JOSAB.21.000473.

[214] M. Gajdacz, A. J. Hilliard, M. A. Kristensen, P. L. Pedersen, C. Klempt, J. J. Arlt, and J. F. Sherson, *Preparation of Ultracold Atom Clouds at the Shot Noise Level*, Physical Review Letters, 117, 2016, DOI: 10.1103/PhysRevLett.117.073604.

Danksagung

Ich möchte mich bei allen bedanken, die mich während meiner Doktorandenzeit unterstützt haben.
Ich bedanke mich bei Herrn apl. Prof. Dr. Carsten Klempt für die Übernahme des Referats, sowie die Möglichkeit in seiner Gruppe meine Doktorarbeit anfertigen zu können. Die stets freundliche und lockere Atmosphäre, sowie die stetige Ansprechbarkeit haben die Arbeit am Experiment sehr erleichtert. Ich danke auch Frau Prof. Dr. Silke Ospelkaus und Herrn Prof. Dr. Jan Arlt für die Übernahme der Koreferate. Herrn Prof. Dr. Luis Santos danke ich für die Übernahme des Prüfungsvorsitzes.

Ein besonderer Dank geht an Jiao Geng, Cebrail Pür, Mareike Hetzel, Luise Schaefer und Ilka Kruse, für den freundschaftlichen Umgang, die gemeinsame Arbeit im Aufbau und am Experiment. Insbesondere möchte ich mich bei Jan Peise bedanken, für die stetige Ansprechbarkeit, sowie unzählige technische und fachliche Ratschläge. Fabian Anders danke ich für die freundlische Bereitstellung seines Quellcodes zur Simulation von Interferometersequenzen. Auch bei Karsten Lange und Jan Mahnke möchte ich mich für den netten und hilfsbereiten Umgang während unserer gemeinsamen Zeit am Institut bedanken.

Ein aufrichtiger Dank richtet sich an die Sekretärinnen, besonders an Frau Ohlendorf, die meinen Promotionsablauf organisiert und unterstützt hat. Mein dank gilt natürlich auch dem Rest des Teams, Frau Faber, Frau Hünitzsch und Frau Pfennig die immer für Fragen und Probleme ansprechbar waren. Eine unersetzbare Hilfe war auch das Werkstatt-Team um Alexander Vocino, das die anspruchsvolle Fertigung der Spulenhalter und sonstiger Spezialanfertigungen die im Labor benötigt werden mit Tatkraft und Geduld gemeistert hat. Darüber hinaus möchte ich mich auch bei Kai-Martin Knaak bedanken, der bei jeglichen Fragen zu elektronischen Themen immer ein offenes Ohr hat.

Vielen Dank!

List of publications

- J. Mahnke, I. Kruse, A. Hüper, S. Jöllenbeck, W. Ertmer, J. Arlt, C. Klempt,
  A continuously pumped reservoir of ultracold atoms
  J. Phys. B: At. Mol. Opt. Phys. **48**, 165301 (2015),
  DOI: 10.1088/0953-4075/48/16/165301

Curriculum vitae

Personal Details

Name	Andreas Hüper
Date of birth	July 15, 1987
Place of birth	Hannover, Germany

Education

11/2013 - 06/2019	Doctoral studies at Institut für Quantenoptik , Leibniz Universität Hannover
10/2010 - 10/2013	Master's studies at Georg-August-Universität Göttingen and the Max-Planck-Institute für biophysikalische Chemie
08/2010 - 09/2010	Internship at Max-Planck-Institute für Dynamik und Selbstorganisation, Göttingen
10/2007 - 07/2010	Bachelor's studies at Georg-August-Universität Göttingen
07/2006	Abitur at Gymnasium St. Ursula-Schule, Hannover

Erklärung der Selbstständigkeit

Hiermit versichere ich, die vorliegende Arbeit selbstständig verfasst und keine anderen als die angegebenen Quellen und Hilfsmittel benutzt, sowie alle Stellen der Arbeit, die wörtlich oder sinngemäß aus anderen Quellen übernommen wurden, als solche kenntlich gemacht zu haben. Die Arbeit hat in gleicher oder ähnlicher Form noch keiner Prüfungsbehörde vorgelgen.

Hannover, den 30.04.2019 Andreas Hüper